

Research on Engineering Structures & Materials

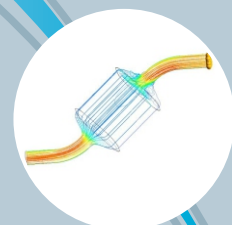
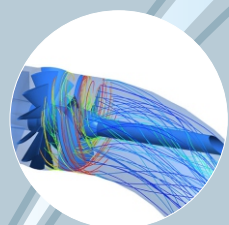
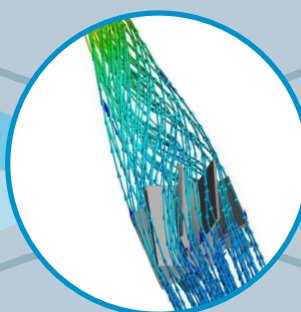
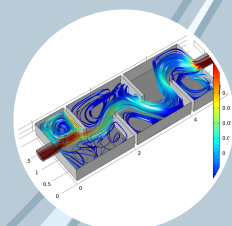
Volume :4

Issue: 3

p-ISSN: 2148-9807

e-ISSN: 2149-4088

Special Focus on:
Optimal Fluid Systems
&
Machinery



Edited by
Andreas Öchsner
Luiz A. O. Rocha
Antonio F. Miguel

www.jresm.org



MIM RESEARCH GROUP

The International Journal of **Research on Engineering Structures and Materials (RESM)** is a peer-reviewed open access journal (p-ISSN: 2148-9807; o-ISSN: 2149-4088) published by MIM Research Group. It is published in February, June and September.

The main objective of RESM is to provide an International academic platform for researchers to share scientific results related to all aspects of mechanical, civil and material engineering areas.

RESM aims the publication of original research articles, reviews, short communications technical reports, and letters to the editor on the latest developments in the related fields.

All expenditures for the publication of the manuscripts are most kindly reimbursed by *MIM Research Group*. Thus, authors do not need to pay for publishing their studies in the journal.

The scope of the journal covers (but not limited to) behavior of structures, machines and mechanical systems, vibration, impact loadings and structural dynamics, mechanics of materials (elasticity, plasticity, fracture mechanics), material science (structure and properties of concrete, metals, ceramics, composites, plastics, wood, etc.,), nano-materials performances of new and existing buildings and other structural systems, design of buildings and other structural systems, seismic behavior of buildings and other structural systems, repair and strengthening of structural systems, case studies and failure of structural systems, safety and reliability in structural and material engineering, use of new and innovative materials and techniques in energy systems and mechanical aspects of biological systems (biomechanics and biomimetics).

The topics covered in RESM include:

- Structural Engineering
- Mechanical Engineering
- Material Engineering
- Earthquake Engineering
- Nano-technology
- Energy Systems
- Biomimetics, Biomechanics

Abstracting and Indexing

Please visit <http://www.jresm.org> for more information.

Graphics and Design

Dr. H Ersen Balcioglu

ersen.balcioglu@usak.edu.tr



**RESEARCH on
ENGINEERING STRUCTURES &
MATERIALS**



Published by MIM Research Group

RESEARCH on ENGINEERING STRUCTURES & MATERIALS

Editor in Chief

Hayri Baytan Özmen Usak University Turkey

Editor

Antonio F. Miguel	University of Evora	Portugal
Andreas Öchsner	Esslingen University of Applied Sciences	Germany
Luiz A. O. Rocha	Universidade do Vale do Rio dos Sinos.	Brazil

Editorial Board Members

Farid Abed-Meraiam	Arts et Métiers ParisTech	France
P. Anbazhagan	Indian Institute of Science	India
Raffaele Barretta	University of Naples Federico II	Italy
R.S. Beniwal	Council of Scientific and Industrial Research	India
Antonio Caggiano	University of Buenos Aires	Argentina
Noël Challamel	University of South Brittany	France
Abdulkadir Çevik	Gaziantep University	Turkey
J. Paulo Davim	University of Aveiro	Portugal
Hom Nath Dhakal	University of Portsmouth	UK
S. Amir M. Ghannadpour	Shahid Beheshti University	Iran
David Hui	University of New Orleans	USA
Jian Jiang	National Institute of Standards and Technology	USA
Ramazan Karakuzu	Dokuz Eylül University	Turkey
Arkadiusz Kwiecien	Cracow University of Technology	Poland

Stefano Lenci	Università Politecnica delle Marche	Italy
Yuan Meini	North University of China	China
Mohammad Mehdi Rashidi	University of Tongji	China
Pier Paolo Rossi	University of Catania	Italy
Neritan Shkodrani	Polythecnic University of Tirana	Albania
Faris Tarlochan	Qatar University	Qatar
Y.B. Yang	National Taiwan University	Taiwan

Advisory Board Members

Erdogan Gök	Loughborough University	England
Khashayar Hosseinzadeh	Babol Noshirvani University	Iran
Mohsen Sheikholesmani	Babol Noshirvani University	Iran
Gökhan Gece	Ankara University	Turkey
Felipe Bertelli	Universidade Estadual de Campinas	Brazil
V. Mohanavel	St. Peter's University	India
Gül Tosun	Fırat University	Turkey
George Oguntala	University of Bradford	UK
Sobhan Mosayebidorcheh	Babol Noshirvani University	Iran
Hayri Baytan Özén	Usak University	Turkey
Philip Oladijo	Botswana International University	Botswana
Hakan Sarıkaya	Usak University	Turkey
Hamid Khan	National University of Computer and Emerging Sciences	Pakistan
Habibe Demir	İskenderun Teknik University	Turkey
M. W. Moura	Universidade Federal do Rio Grande	Brazil
Liércio André Isoldi	Universidade Federal do Rio Grande	Brazil
Flavia Zinani	Universidade do Vale do Rio dos Sinos	Brazil
Luiz Rocha	Universidade do Vale do Rio dos Sinos	Brazil
Elizaldo Domingues dos Santos	Universidade Federal do Rio Grande	Brazil
Tunde Bello-Ochende	Duke University	UK
Gözde Sarı	Celal Bayar University	Turkey

In This Issue

Editorial Note

- 137 **Andreas Öchsner, Luiz A. O. Rocha, Antonio F. Miguel**
Preface

Research Article

- 139 **Marcelo Langhinrichs Cunha, Grégori da Silva Troina, Elizaldo Domingues dos Santos, Luiz Alberto Oliveira Rocha, Liércio André Isoldi**

Computational modeling and Constructal Design method applied to the geometric optimization of stiffened steel plates subjected to uniform transverse load

Research Article

- 151 **Liang Ji, Xinzhi Liu, Houlei Zhang**
Properties of furfural residue and its drying characteristics in single-shaft paddle heat exchangers

Research Article

- 161 **Onur Yenigün, Turgay Coşkun, Erdal Çetkin**
The effect of time delay of fluid flow in a vascularized plate

Research Article

- 169 **Daniel Helbig, Marcelo Langhinrichs Cunha, Caio Cesar Cardoso da Silva, Elizaldo Domingues dos Santos, Ignácio Iturrio, Mauro de Vasconcellos Real, Liércio André Isoldi, Luiz Alberto Oliveira Rocha**
Numerical study of the elasto-plastic buckling in perforated thin steel plates using the constructal design method

Research Article

- 189 **Nelson C. Batista, Rui Melicio, Victor M.F. Mendes**
Darrieus vertical axis wind turbines: methodology to study the self-start capabilities considering symmetric and asymmetric airfoils

Research Article

- 219 **Anunciação Jr.N. C, Anflor C.T.M, Goulart J.N.V**
Optimization applied to dynamic poroelasticity using boundary element method (BEM) and genetic algorithm (GA)

Free access to tables of content, abstracts and full text of papers for web visitors.

ABSTRACTING / INDEXING

The international journal of Research on Engineering Structures and Materials (RESM) is currently Absracted/Index by CrossRef, Google Scholar, Universal Impact Factor, Scientific Indexing Service, Research Bible, CiteFactor, Electronic Journal Library, Open Academic Journals Index, Global Impact Factor, Directory of Research Journals Indexing, Materials Science & Engineering Database (ProQuest) Engineering Journals (ProQuest), ULAKBİM TR Index (Tubitak) and under evaluation by many other respected indexes.





Editorial Note

Preface

Andreas Öchsner¹, Luiz A. O. Rocha², Antonio F. Miguel^{*3}

¹ Faculty Mechanical Engineering, Esslingen University of Applied Sciences, Germany

² Mechanical Engineering, Universidade do Vale do Rio dos Sinos, Brazil

³ Department of Physics, University of Evora, Portugal

The competitive cost of numerical simulations over laboratory studies, due to the continued advancements in computing performance, has made computational fluid dynamics an integral tool in the study of engineering problems. This topical special focus issue "Optimal Fluid Systems and Machinery" of the Journal of Research on Engineering Structures & Materials (RESM) covers a varied range of engineering systems. It contains papers selected on the basis of the results of regular peer review of the short manuscripts submitted for consideration by the participants of the Special Session "Fluid Flow, Energy Transfer and Design" at the 13th International Conference on Diffusion in Solids and Liquids (DSL2017) held in Vienna, Austria.

The rapid growth of wind power generation and the need for a smarter grid with decentralized energy generation motivated the study of Batiata et al. [1]. They studied the self-start ability of vertical axis wind turbines, and suggested a new methodology that offers a substantial time reduction in the first steps of new blade profiles development.

Plates used as structural elements in the construction of bridges, offshore structures, etc., are subjected to compression stresses. A geometric evaluation of stiffened plates subjected to a uniformly distributed transverse loading is presented by Cunha et al. [2]. Helbig et al. [3] studied the presence of perforations in plates that causes a redistribution of stresses, affecting both the resistance and buckling characteristics.

Since the introduction of the concept of microchannel heat sink during the 1980s, there has been a huge growth of compact heat exchangers. It is required compactness ally to high dissipation of heat fluxes. Yenigün et al. [4] studied optimal time delay of the fluid flow in parallel and tree-shaped vascular channel structures heated with random heat loads.

A knowledge of properties of soil and rocks is important to improve estimates of underground resources. To gain insight regarding the dynamic poroelasticity of a soil, a coupling of the both the Genetic Algorithm and the Boundary Element Method are used by Anunciação Jr. et al. [5].

Residues of furfural ($C_5H_4O_2$) production used in chemical and pharmaceutical engineering has a high moisture content which is harmful to environment. Ji et al. [6] evaluated the drying capacity of these residues, and made some brief suggestions about the design of a drying-combustion integration system for furfural residues.

*Corresponding author: afm@uevora.pt

DOI: <http://dx.doi.org/10.17515/jresm2018.44ds2203ed>

The editors would like to take this opportunity to thank all the authors and the reviewers for their time and great effort in the preparation of this topical special issue. Also acknowledged the support of Dr. Hayri Baytan Özmen, who is the Editor-in-Chief of RESM.

References

- [1] Batista NC, Melicio R, Mendes VMF. Darrieus vertical axis wind turbines: methodology to study the self-start capabilities considering symmetric and asymmetric airfoils. *Res. Eng. Struct. Mat.*, 2018; 4(3): 189-217. <http://dx.doi.org/10.17515/resm2017.39ds0108>
- [2] Cunha ML, Troina GS, Santos ED, Rocha LAO, Isoldi LA. Computational modeling and Constructal Design method applied to the geometric optimization of stiffened steel plates subjected to uniform transverse load *Res. Eng. Struct. Mat.*, 2018; 4(3): 139-149. <https://doi.org/10.17515/resm2017.18st1118>
- [3] Helbig O, Cunha ML, Silva CCC, Santos ED, Iturrio I, Real MV, Isoldi LA, Rocha LAO. Numerical study of the elasto-plastic buckling in perforated thin steel plates using the constructal design method. *Res. Eng. Struct. Mat.*, 2018; 4(3): 169-187. <https://doi.org/10.17515/resm2017.37ds1123>
- [4] Yenigun O, Coskun T, Cetkin E. The effect of time delay of fluid flow in a vascularized plate. *Res. Eng. Struct. Mat.*, 2018; 4(3): 161-167. <https://doi.org/10.17515/resm2017.33ds1025>
- [5] Anunciação JNC, Anflor CTM, Goulart JNV. Optimization applied to dynamic poroelasticity using boundary element method (BEM) and genetic algorithm (GA). *Res. Eng. Struct. Mat.*, 2018; 4(3): 219-230. <https://doi.org/10.17515/resm2017.34ds1108>
- [6] Ji L, Liu X, Zhang H. Properties of furfural residue and its drying characteristics in single-shaft paddle heat exchangers. *Res. Eng. Struct. Mat.*, 2018; 4(3): 151-160. <http://dx.doi.org/10.17515/resm2017.32ds1025>



Research Article

Computational modeling and Constructual Design method applied to the geometric optimization of stiffened steel plates subjected to uniform transverse load

Marcelo Langhinrichs Cunha¹, Grégori da Silva Troina¹, Elizaldo Domingues dos Santos¹, Luiz Alberto Oliveira Rocha², Liércio André Isoldi^{*1}

¹ Federal University of Rio Grande - FURG, Rio Grande, RS, Brazil.

²University of Vale do Rio dos Sinos - UNISINOS, São Leopoldo, RS, Brazil.

Article Info

Article history:

Received 18 Nov 2017

Revised 10 Jan 2018

Accepted 15 Jan 2018

Keywords:

Numerical simulation,

Stiffened plates,

Constructual design,

Finite element method

Abstract

The present paper shows a geometric evaluation of stiffened plates subjected to a uniformly distributed transverse loading. For that, it was proposed a set of different geometric configurations through the Constructual Design method, which were numerically simulated. Then, by means of the Exhaustive Search technique, a geometric optimization was performed aiming to minimize the central deflection of the plate. A non-stiffened plate measuring 2.00 m x 1.00 m x 0.02 m was used as reference, then a constant volume ratio ϕ , equals to 0.5, was taken from the reference plate and transformed into longitudinal and transverse stiffeners. The geometric parameters considered as degrees of freedom were: the number of longitudinal (N_{ls}) and transverse (N_{ts}) stiffeners and h_s/t_s , which is defined by the ratio between the stiffener's height and thickness. In order to elaborate the computational model, it is used ANSYS Mechanical APDL®, a software based on the Finite Element Method (FEM). From the results, it was possible to determine a power function for each combination of N_{ls} and N_{ts} that accurately described the relation between the central deflection and h_s/t_s . Furthermore, it was noticed a substantial influence of the geometric parameters under analyses regarding the studied structural element's mechanical behavior. Even though the volume was kept constant, the optimized geometry has shown a result 9110 % better compared to the one shown by the reference plate.

© 2018 MIM Research Group. All rights reserved.

1. Introduction

Thin plates are defined as being structural components where the transverse dimension, called thickness, is considerably smaller than the planar dimensions, called width and length [1]. Stiffeners are reinforcement beams attached to the plates longitudinally, transversally or both. The main advantage of incorporating stiffeners into plates is the reduction of the structure's displacements due to the increase of its moment of inertia, thus avoiding the need to use a thicker plate. Stiffened thin plates are widely used to resist distributed and/or concentrated transverse loads in many structural systems such as bridges, ship hulls, vehicles, oilrigs, buildings and aircraft, among others, mainly due to its great strength-weight ratio [2].

In the past years, many researches have been performed seeking to analyze the behavior of plates reinforced with stiffeners under transverse loading. Yousif *et al.* [3] presented the relation between the height of one lengthwise stiffener and the strength of a given set of

*Corresponding author: liercioisoldi@furg.br

DOI: <http://dx.doi.org/10.17515/jresm2017.18st1118>

plates clamped on its four edges subjected to a pressure load. Virág [4] by using strength calculation methods investigated the minimum cost geometry of various stiffened plates with different loads, types and even stiffener shapes. Tanaka and Bercin [5] used the Boundary Element Method (BEM) in order to analyze the effect of different cross-sections stiffeners in plates subjected to bending. Bedair [6] investigated the stiffener positioning influence on the stability of thin plate structures under bending and compression combined loads through the Sequential Quadratic Programming (SQP) method. Finally, Silva [7] made a numerical study about ribbed slabs, idealizing it as a plate-beam system and using ANSYS® software to model the slab (with SHELL63 element type) and the ribs (with BEAM44 element type).

Since there are no analytical solutions that effectively describe the stiffened plate's behavior when subjected to transverse loads, computational models are helpful and important tools in order to analyze these structural components. Therefore, the present study uses the software ANSYS Mechanical APDL®, based on the Finite Element Method (FEM), to build the computational model to numerically simulate the behavior of the different stiffened plates' geometries derived from the application of the Constructal Design method. Considering the Fig. 1 and starting from a non-stiffened reference plate, the set of geometric configurations of stiffened plates to be analyzed were obtained through a variation of the number of longitudinal stiffeners (N_{ls}), the number of transverse stiffeners (N_{ts}) and the ratio between the stiffeners' height and thickness (h_s/t_s), always keeping the total steel volume constant. In addition, for each stiffened plate configuration an equal longitudinal stiffener spacing (S_{ls}) and an equal transverse stiffener spacing (S_{ts}) were adopted. All results were compared through Exhaustive Search technique aiming to obtain the optimum geometry that minimizes the deflection at the center of the plate.

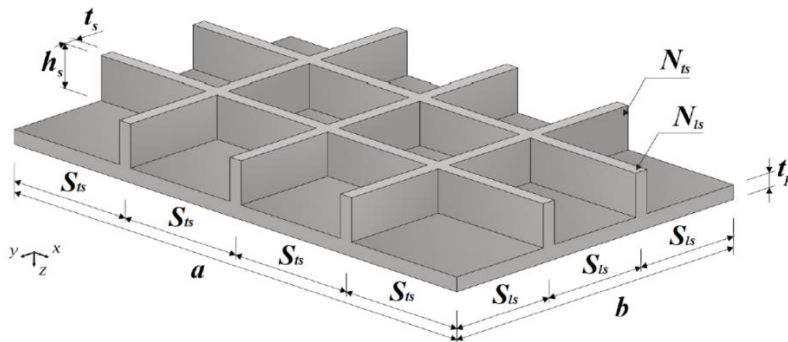


Fig. 1 Stiffened plate P(2,3)

2. Constructal Design Method

The Constructal Design method is based on the Constructal Law: "For a finite-size flow system to persist in time (to survive) its configuration must evolve in such a way that it provides an easier access to the currents that flow through it" [8]. This principle might be used for both predicting natural systems configurations such as river basins, animal design and earth climate; as well as yielding updated designs for engineering applications, for example in the areas of heat transfer, fluid mechanics and mechanic of materials [9].

According to Bejan [10], Constructal Design is a methodology that enables to determine a geometry that leads to the best performance of a system when subjected to a flow. For that, the flow should be malleable and the geometry is deduced from a principle of global performance maximization. Specifically in mechanic of materials problems, as explained in

Bejan and Lorente [11], this flow is related with the flow of stresses in the structure. Besides that, it should be imposed global restrictions to the geometry and vary the degrees of freedom.

The goal in the present work is to improve the mechanical behavior of stiffened plates regarding the deflection at its center by varying geometric parameters, yet without changing the plate total volume. In order to do so, it is used a non-stiffened plate as reference, then a fraction ϕ of volume is taken from this reference plate and transformed into stiffeners. The volume fraction ϕ is given by:

$$\phi = \frac{V_s}{V_r} = \frac{N_{ls}(ah_{st}s) + N_{ts}[(b - N_{ls}s)t_s]h_{st}s}{abt} \quad (1)$$

where, V_s is the reference plate's volume transformed into stiffeners, V_r is the reference non-stiffened plate's total volume, N_{ls} and N_{ts} are, respectively, the number of longitudinal and transverse stiffeners, h_s represents the height and t_s the thickness of the stiffeners. Lastly, a , b and t are, respectively, the length, width and thickness of the reference plate. Thus, all analyzed geometries have the same amount of material, enabling performing a comparative evaluation of their structural performance regarding the transversal deflections.

Seeking to determine the optimal geometry, it was investigated the influence of the degrees of freedom N_{ls} , N_{ts} and h_s/t_s . It were analyzed 36 combinations of longitudinal and transverse stiffeners equally spaced (see Fig. 1), with the following variation: $N_{ls} = 2, 3, 4, 5, 6$ and 7 and $N_{ts} = 2, 3, 4, 5, 6$ and 7. So, these plates were nominated accordingly with the notation $P(N_{ls}, N_{ts})$, such as the plate $P(2,3)$ presented in Fig. 1. In addition, it were used sizes of stiffeners' thickness ranging from 3.75 mm (1/8 in) to 76.2 mm (3 in), therefore the h_s/t_s ratio derives from these predefined t_s sizes. Moreover, the height h_s complies two geometric constraints: it should not be higher than 300 mm, in order to avoid a substantial disproportionality between the stiffener's height and the plate's dimensions; and the ratio h_s/t_s should be greater than 1 to avoid the thickness from being greater than the height.

3. Computational Modeling

The present work uses computational models based on the Finite Element Method (FEM) in order to numerically simulate the mechanical behavior of plates under a distributed transverse load. Basically, a finite element analysis consists of four steps: creation of the model geometry, mesh generation, application of the load and boundary conditions and the solution of the problem [12].

When analyzing the linear elastic behavior of mechanical structures through the FEM, it is used the virtual work principle in order to solve the problem. Concerning static analysis, the effects of damping and inertial forces are not taken into account when estimating the magnitude of displacements and internal forces at any part of the system, which are obtained through the algebraic equation [13]:

$$[K] \cdot \{U\} = \{F\} \quad (2)$$

where, $[K]$ is the stiffness matrix, $\{U\}$ is the unknown nodal displacement vector and $\{F\}$ is the external forces vector. The stiffness matrix $[K]$ is defined by the stress-strain and strain-deflection relations of the structure.

Nowadays, a wide variety of software adopt a FEM approach to analyze engineering problems, for instance the ANSYS Inc. software package, whose applications range from static structural to fluid dynamics problems. Since it is suitable for solving structural

problems, this work uses the SHELL281 finite element of the ANSYS Mechanical APDL® software for all studied cases.

The SHELL281 has six degrees of freedom (rotation and translation on x , y and z directions) for each of its eight nodes, being indicated for linear, large rotation and large strain nonlinear applications. It is also appropriate to analyze thin to moderately thick structural components. When using SHELL281, two relevant assumptions are made: the normal stress varies linearly through the thickness and the transverse shear strains are constant through the thickness [14].

3.1. Computational Model Verification

To verify the computational model it was simulated two simply supported plates with one longitudinal stiffener subjected to a 10 kN/m^2 uniform load, as shown in Fig. 2. The Poisson's ratio and Young's modulus are 0.154 and 30 GPa, respectively. It was analyzed two different stiffener's heights: $h_s = 1.25 \text{ m}$ and $h_s = 2.00 \text{ m}$, both cases were previously studied by Silva [7].

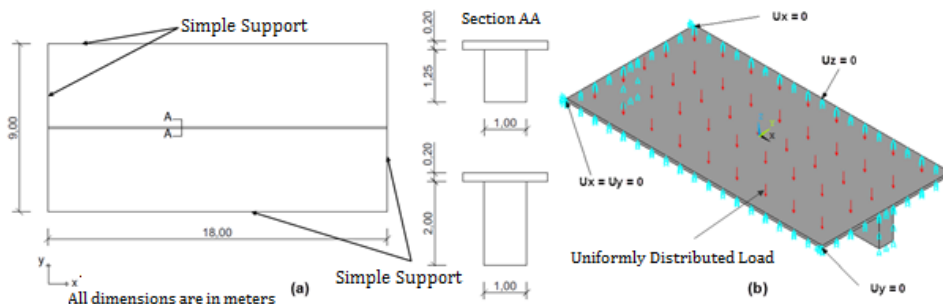


Fig. 2 Retangular plate with one longitudinal stiffener: (a) physical model (adapted from [7]) and (b) boundary and load conditions

A comparison between the obtained numerical results for the transverse displacements at the plate's center and the results presented by Silva [7], as well as a mesh convergence test for $h_s = 1.25 \text{ m}$ and $h_s = 2.00 \text{ m}$ is shown in Fig. 3. The structure was discretized by SHELL281 finite element with quadrilateral format, generating regular meshes.

It can be seen in Fig. 3 that the mesh convergence is reached in the second refinement in both cases. Moreover, there is a great approximation between the obtained numerical results and those presented by Silva [7]. Therefore, the computational model using the finite element SHELL281 was properly verified. Besides, from Fig. 3 one can note that the proposed model has a better agreement with Silva [7] for $h_s = 2.00 \text{ m}$. In other words, the decrease of h_s value promotes a slight difference between the numerical results of the present work and those obtained by Silva [7].

4. Results and Discussion

As earlier mentioned, a non-stiffened plate was adopted as reference. This steel plate has modulus of elasticity $E = 200 \text{ GPa}$, Poisson's ratio $\nu = 0.3$, length $a = 2.00 \text{ m}$, width $b = 1.00 \text{ m}$ and thickness $t = 0.02 \text{ m}$, being considered simply supported in its four edges. Using a converged mesh with 800 quadrilateral shaped SHELL281 elements and applying a transverse uniform load of 10 kPa , a central deflection of $U_{zr} = 0.698 \text{ mm}$ was numerically obtained for the reference plate.

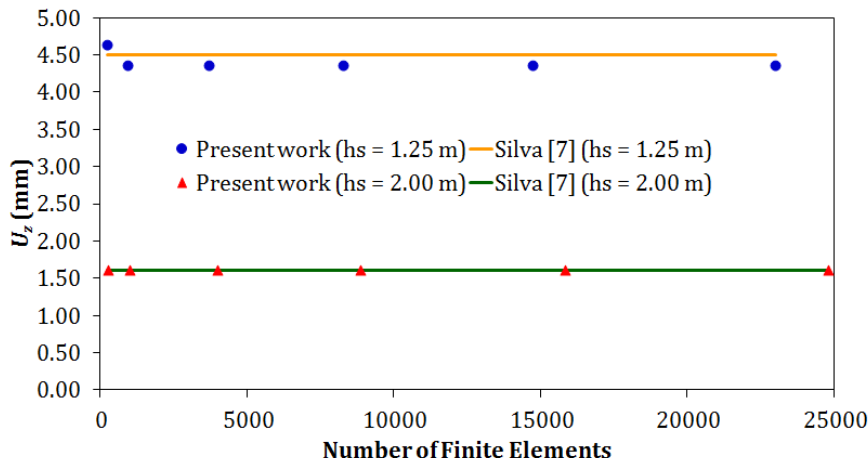


Fig. 3 Convergence mesh and computational model verification

Thereafter, the stiffened plates' configurations were defined by turning a material portion of the reference plate's thickness into stiffeners, which was the only imposed modification. In other words, a volume fraction of $\phi = 0.5$ from the reference plate was transformed into stiffeners, while all other parameters (E, ν, a, b , support conditions and loading) were kept the same as those of the reference plate.

So it was conducted a mesh convergence test seeking to determine the minimum number of finite elements to be used in stiffened plates simulations. For that test, it was used the most complex geometry studied in this work, which is the plate P(7,7) with $t_s = 4.75\text{ mm}$ and $h_s/t_s = 42.68$. It was performed five numerical simulations using different element sizes and mesh densities. Table 1 shows the results of these five simulated meshes, highlighting the convergence between the obtained results for the out-of-plane displacements at the center of the stiffened plate.

Table 1. Mesh independence test

Mesh	Element's size (m)	Nº of finite elements	Displacement U_z (mm)	Relative difference between meshes (%)
M1	0.2000	464	0.020114	0.124
M2	0.1000	1224	0.020139	0.055
M3	0.0500	3200	0.020150	0.020
M4	0.0375	5488	0.020154	0.009
M5	0.0250	9064	0.020156	-----

The mesh that leads to an independent result is the mesh M3 (see Table 1), whose relative difference with the following mesh is 0.02 %. Thus, all analyzed plates were modeled using the mesh M3, i.e., a regular mesh generated by quadrilateral SHELL281 elements with edge length of 0.05 m. Figure 4 shows the plate's discretization using the mesh M3, which is the independent mesh for the configuration P(7,7).

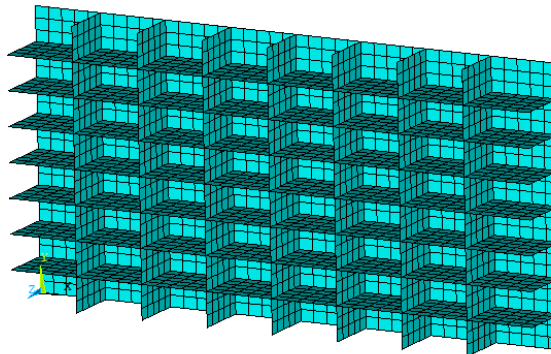


Fig. 4 Plate P(7,7) with $t_s = 4.75$ mm and $h_s/t_s = 42.68$ using the converged mesh M3

After that, all proposed stiffened plate configurations were numerically simulated. As expected, it was noted that the redistribution of the reference plate's material, by turning a portion of its thickness into stiffeners, improves the mechanical behavior regarding the deflection at the center since all analyzed configurations presented a lower deflection than the reference plate, where the worst analyzed geometry P(7,2) with $h_s/t_s = 1.27$ presented a displacement ($U_z = 0.448$ mm) 35.81% smaller than the reference plate ($U_{zr} = 0.698$ mm).

To exemplify how the variation of the h_s/t_s ratio influences in the central deflection of the stiffened plates, a scatter plot for the numerical results of the plates P(2,2) and P(2,7) is shown in Fig. 5. One can note that the h_s/t_s increase promotes a reduction in the central deflection value, being this a coherent behavior. It was also observed that it is possible to estimate a power function, which describes mathematically the relation between the variables under analysis with great accuracy. In addition to the scattered data for P(2,2) and P(2,7), in Fig. 5 it is presented a power trendline as well as the curve function and the coefficient of determination (R^2) for each plate.

It is important to mention that all analyzed geometric configurations presented the same pattern of deflection results observed in Fig. 5. Therefore, it is possible to determine for each one of the studied stiffened plates a curve fitting by a power function:

$$U_z = c_1 * (h_s/t_s)^{c_2} \quad (3)$$

where, the coefficients c_1 and c_2 depend on the number of longitudinal and transverse stiffeners. Table 2 shows the coefficients c_1 , c_2 , the coefficient of determination R^2 as well as the range of h_s/t_s that was numerically simulated in order to obtain the coefficients for each studied geometric configuration.

Through the results shown in Table 2, it is possible to observe that, since the coefficient c_2 is negative for all stiffened plates, an increment in the h_s/t_s ratio leads to a decrement in the displacement U_z , corroborating with the behavior already noted in Fig. 5. Moreover, when comparing the results as, for example, the plates P(6,3) with $h_s/t_s = 59.43$ and P(6,3) with $h_s/t_s = 1.37$ it is observed a difference of 94 % in the performance regarding the deflection at the plate's center. Remembering that the total steel volume is kept constant for all plates, this considerable performance's improvement occurred only due to the influence of the geometry in the structure's behavior.

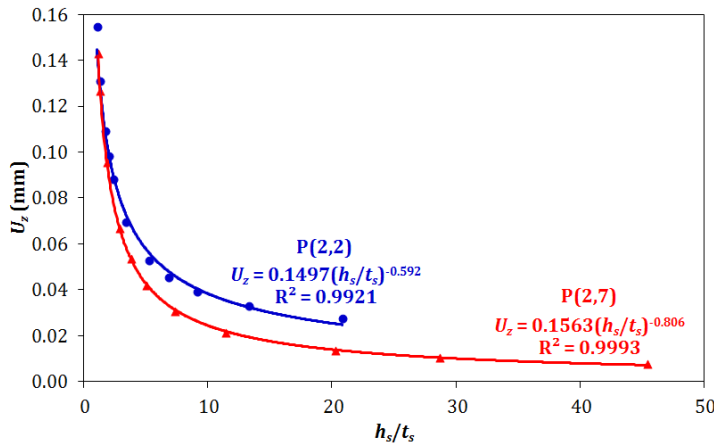


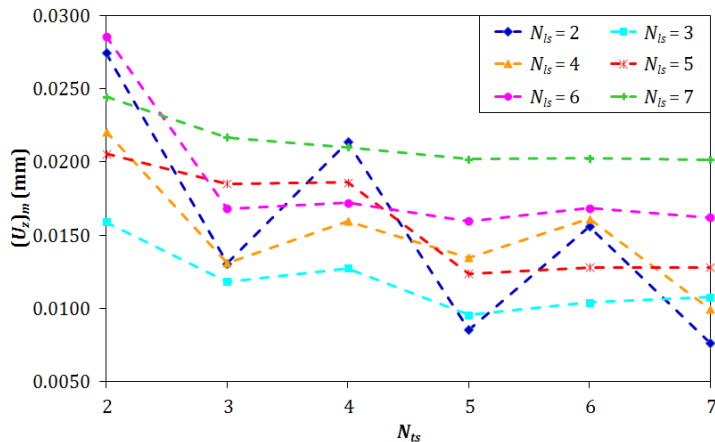
Fig. 5 Scatter plot of the relation between U_z and h_s/t_s of the plates P(2,2) and P(2,7) with their respective power trendlines

The Constructal Design method enables to perform an influence analysis of the degrees of freedom in the proposed stiffened plates' mechanical behavior. In this context, to obtain the global minimum deflection at the center among all analyzed configurations, it was evaluated the influence of N_{ls} , N_{ts} and h_s/t_s . Based on the Eq. (3) and the coefficients presented in Table 2, for each combination of longitudinal and transverse stiffeners, it was determined the optimal h_s/t_s called $(h_s/t_s)_o$, i.e., the h_s/t_s ratio that minimizes the plate's central displacement, called $(U_z)_m$. The graph in Fig. 6 shows the minimized displacement at the plates' center ($U_z)_m$ for each combination of the number of transverse stiffeners N_{ts} and the number of longitudinal stiffeners N_{ls} .

From Fig. 6, contrary to the common sense, it is not possible to affirm that an increase in the number of stiffeners always will generate an improvement in the plate stiffness. This is because the volume of material is constant, so an increase in the number of stiffeners entails a reduction in their height and hence the cross-sectional moment of inertia becomes smaller. Another important observation about Fig. 6 is that the results have an oscillating trend, which demonstrates that plates with an odd number of transverse stiffeners (N_{ts}) present better results when compared with those with an even number of transverse stiffeners. This can be explained by the fact that plates with an odd N_{ts} have a stiffener at its very center, reducing its central deflection.

Table 2 Geometric configuration's Coefficients

$P(N_{ls}, N_{ts})$	c_1	c_2	R^2	Range
P(2,2)	0.1497	-0.5917	0.9921	$1 \leq h_s/t_s \leq 20.84$
P(2,3)	0.1377	-0.8229	0.9999	$1 \leq h_s/t_s \leq 17.91$
P(2,4)	0.1397	-0.6074	0.9894	$1 \leq h_s/t_s \leq 27.79$
P(2,5)	0.1431	-0.8064	0.9996	$1 \leq h_s/t_s \leq 35.03$
P(2,6)	0.1474	-0.6820	0.9948	$1 \leq h_s/t_s \leq 31.55$
P(2,7)	0.1563	-0.8056	0.9993	$1 \leq h_s/t_s \leq 45.46$
P(3,2)	0.2177	-0.7996	0.9998	$1 \leq h_s/t_s \leq 27.72$
P(3,3)	0.1960	-0.8013	0.9998	$1 \leq h_s/t_s \leq 35.00$
P(3,4)	0.1921	-0.7958	0.9998	$1 \leq h_s/t_s \leq 31.55$
P(3,5)	0.1904	-0.7970	0.9998	$1 \leq h_s/t_s \leq 45.48$
P(3,6)	0.1932	-0.7946	0.9997	$1 \leq h_s/t_s \leq 41.73$
P(3,7)	0.1995	-0.8065	0.9994	$1 \leq h_s/t_s \leq 38.55$
P(4,2)	0.2927	-0.7632	0.9997	$1 \leq h_s/t_s \leq 31.45$
P(4,3)	0.2606	-0.7952	0.9997	$1 \leq h_s/t_s \leq 45.40$
P(4,4)	0.2442	-0.7503	0.9994	$1 \leq h_s/t_s \leq 41.69$
P(4,5)	0.2439	-0.7995	0.9992	$1 \leq h_s/t_s \leq 38.53$
P(4,6)	0.2392	-0.7650	0.9995	$1 \leq h_s/t_s \leq 35.82$
P(4,7)	0.2430	-0.7950	0.9996	$1 \leq h_s/t_s \leq 59.62$
P(5,2)	0.3780	-0.7882	0.9987	$1 \leq h_s/t_s \leq 41.55$
P(5,3)	0.3337	-0.7974	0.9985	$1 \leq h_s/t_s \leq 38.43$
P(5,4)	0.3118	-0.7920	0.9981	$1 \leq h_s/t_s \leq 35.75$
P(5,5)	0.2997	-0.7918	0.9994	$1 \leq h_s/t_s \leq 59.57$
P(5,6)	0.2937	-0.7898	0.9992	$1 \leq h_s/t_s \leq 55.90$
P(5,7)	0.2923	-0.7961	0.9985	$1 \leq h_s/t_s \leq 52.66$
P(6,2)	0.4679	-0.7838	0.9963	$1 \leq h_s/t_s \leq 35.62$
P(6,3)	0.4103	-0.7924	0.9989	$1 \leq h_s/t_s \leq 59.43$
P(6,4)	0.3765	-0.7789	0.9990	$1 \leq h_s/t_s \leq 55.80$
P(6,5)	0.3602	-0.7926	0.9980	$1 \leq h_s/t_s \leq 52.58$
P(6,6)	0.3463	-0.7812	0.9980	$1 \leq h_s/t_s \leq 49.72$
P(6,7)	0.3408	-0.7921	0.9966	$1 \leq h_s/t_s \leq 47.15$
P(7,2)	0.5684	-0.7887	0.9968	$1 \leq h_s/t_s \leq 55.63$
P(7,3)	0.4897	-0.7914	0.9966	$1 \leq h_s/t_s \leq 52.45$
P(7,4)	0.4479	-0.7872	0.9964	$1 \leq h_s/t_s \leq 49.61$
P(7,5)	0.4201	-0.7887	0.9956	$1 \leq h_s/t_s \leq 47.06$
P(7,6)	0.4019	-0.7855	0.9950	$1 \leq h_s/t_s \leq 44.77$
P(7,7)	0.3898	-0.7859	0.9939	$1 \leq h_s/t_s \leq 42.68$

Fig. 6 Effect of the N_{ts} variation over the $(U_z)_mm$ for $N_{ls} = 2$ to 7

Therefore, considering Fig. 6 and Table 2, for each N_{ls} it is possible to determine the optimal N_{ts} , called $(N_{ts})_o$, which represents the number of transverse stiffeners that twice minimizes the out-of-plane central displacement, called $(U_z)_{mm}$. Hence, the twice optimized ratio h_s/t_s , called $(h_s/t_s)_{oo}$, is also defined. These values are shown in Table 3.

Table 3 Values of $(N_{ts})_o$, $(h_s/t_s)_{oo}$ and $(U_z)_{mm}$ for each N_{ls} .

N_{ls}	$(N_{ts})_o$	t_s (mm)	h_s (mm)	$(h_s/t_s)_{oo}$	$(U_z)_{mm}$ (mm)
2	7	6.35	28.87	45.46	0.0077
3	5	6.35	28.89	45.48	0.0096
4	7	4.75	28.32	59.62	0.0099
5	5	4.75	28.29	59.57	0.0124
6	5	4.75	24.98	52.58	0.0160
7	7	4.75	20.27	42.68	0.0201

It can be noticed, through the data of Table 3, that the twice minimized displacement $(U_z)_{mm}$ tends to increase as the degree of freedom N_{ls} enhances. This is explained by the fact that the volume of material used in the construction of all geometric configurations is the same and, consequently, the stiffener's height decreases as well as the structure's moment of inertia.

Finally, among all analyzed cases, the configuration P(2,7) (see Table 3) defined by $(h_s/t_s)_{ooo} = 45.46$, $(N_{ts})_{oo} = 7$ and $(N_{ls})_o = 2$ has the better global performance, leading to a three times minimized displacement at its center of $(U_z)_{mmm} = 0.0077$ mm. The deformed configuration of stiffened plate P(2,7) is depicted in Fig. 7. Thus, even keeping the plate's volume constant, it was reached a mechanical behavior improvement regarding the central deflection of the plate of 9110 % when comparing the optimal geometry with the reference plate without stiffeners.

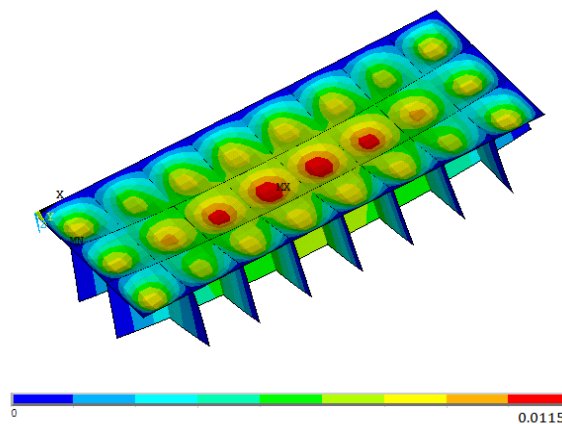


Fig. 7 Deformed configuration of the optimal global plate P(2,7), in mm

5. Conclusions

By using the software ANSYS® to analyze the computational models of the plates derived from the application of the Constructal Design method, it was possible to perform an evaluation about the influence of different geometric parameters on the mechanical behavior of stiffened plates, which are important components widely used in the structural engineering.

It was observed that a rearrangement of material, even without changing the total material's volume of the studied structural component, can entail an improvement in the structural stiffness. It was also shown that besides the number of transverse and longitudinal stiffeners, the ratio h_s/t_s has a significant influence in the plates' stiffness.

Moreover, for each combination of the degrees of freedom N_{ts} and N_{ls} , it was possible to define a regression equation, which describes the relation between the central displacement and the degree of freedom h_s/t_s with great accuracy, presenting a coefficient of determination R^2 greater than 99 %. Therefore, through these equations, it is possible to infer the displacements at the center of the plates for values of the ratio h_s/t_s within the simulated range and even to extrapolate these results, being this an unpublished scientific contribution of the present work.

Through the obtained results, it was observed that since all studied plates have the same volume, an increment in the number of stiffeners does not mean a reduction in the deflection at the plate's center, emphasizing the significance of performing studies regarding the geometric optimization of structural components. In addition, it was noticed that the geometry has a great influence in the structural behavior of the plates, where, for example, the plate P(6,3) with $h_s/t_s = 59.43$ presented a displacement 94 % smaller when compared with the plate P(6,3) with $h_s/t_s = 1.37$. The optimal geometry, among all analyzed configurations, was the plate P(2,7) with the degree of freedom $h_s/t_s = 45.46$, whose deflection at the center was 9110 % better than the plate without stiffeners used as reference.

Therefore, through the application of computational modeling along with Constructal Design it is possible to make recommendations about the suitable geometry to be used as well as to draw conclusions about the structural behavior of varied plates' geometries,

thereby enabling to optimize these structures regarding the minimization of the displacement at the center when subjected to uniform transverse loads.

6. Acknowledgements

The authors thank FAPERGS (Research Support Foundation of Rio Grande do Sul), CNPq (Brazilian National Council for Scientific and Technological Development) and CAPES (Brazilian Coordination for Improvement of Higher Education Personnel) for the financial support.

References

- [1] Timoshenko S, Woinowsky-Krieger S. Theory of Plates and Shells, McGraw-Hill, New York, NY, USA, 1976.
- [2] Shanmugan N E, Liew J Y R, Thevendran V. Thin-walled Structures – Research and Development, Elsevier, Singapore, 1998.
- [3] Yousif M Z, Naief N K M, Hamada Y M. Optimum height of plate stiffener under pressure effect. The 1st Regional Conference of Eng. Sci. NUCEJ Spatial ISSUE; 11(3): 459 – 468, 2008.
- [4] Virág Z. Optimum design of stiffened plates for different loads and shapes of ribs. Journal of Computational and Applied Mechanics, 2004; 5(1): 165-179.
- [5] Tanaka M, Bercin A N. Static bending analysis of stiffened plates using the boundary element method. Engineering Analysis with Boundary Elements, 1998; 21: 147 -154. [https://doi.org/10.1016/S0955-7997\(98\)00002-2](https://doi.org/10.1016/S0955-7997(98)00002-2)
- [6] Bedair O K. Influence of stiffener location on the stability of stiffened plates under compression and in-plane bending. Int. J. Mech. Sci, 1997; 39(1): 33 – 49. [https://doi.org/10.1016/0020-7403\(96\)00017-3](https://doi.org/10.1016/0020-7403(96)00017-3)
- [7] Silva H B S. Análise numérica da influência da excentricidade na ligação placa-viga em pavimentos usuais de edifícios. Master Thesis, Federal University of São Carlos, São Paulo, Brazil, 2010.
- [8] Bejan A. Advanced Engineering Thermodynamics 2nd Ed, Willey, New York, NY, USA, 1997.
- [9] Bejan A, Lorente S. Constructal theory of generation of configuration in nature and engineering. Journal of Applied Physics 100, 041301. <https://doi.org/10.1063/1.2221896>
- [10] Bejan A. Shape and Structure, from Engineering to Nature, Cambridge University Press, Cambridge, England.
- [11] Bejan A, Lorente S. Design with Constructal Theory, John Wiley Sons, Hoboken, NJ, USA, 2008. <https://doi.org/10.1002/9780470432709>
- [12] Zienkiewicz O C. Finite Element Method in Engineering Science 2nd Edition, McGraw-Hill, London, England, 1971.
- [13] Marinho I J P. Projeto ótimo de estruturas metálicas de arquibancadas reutilizáveis via ANSYS. Master Thesis, PUC-Rio, Rio de Janeiro, Brazil, 2002.
- [14] ANSYS Inc. ANSYS User's Manual: Analysis Systems, 2009.



Research Article

Properties of furfural residue and its drying characteristics in single-shaft paddle heat exchangers

Liang Ji, Xinzhi Liu, Houlei Zhang*

School of Energy and Power Engineering, Nanjing University of Science and Technology, Nanjing, China

Article Info

Article history:

Received 25 Oct 2017

Revised 11 Feb 2018

Accepted 20 Jun 2018

Keywords:

Furfural residue,
Property,
Drying, Single-shaft,
Paddle heat
exchanger

Abstract

Furfural residue is a detrimental waste generated in furfural production processes. Combustion is an efficient way to dispose furfural residue and drying is a necessary unit operation prior to combustion. In this paper, the properties of furfural residue, including particle size distribution, proximate analysis and pyrolysis process curves were presented. The flow and drying characteristics of furfural residue in a lab-scale single-shaft paddle heat exchanger were documented. The measurements show that the furfural residue contains high moisture (54.26%) and its as received basis lower heating value is 7301 kJ/kg. The high moisture content in furfural residue makes ignition and efficient combustion very difficult. It is feasible to use single-shaft paddle heat exchanger to dry furfural residue to moisture content of 15.94% which is advantageous for further combustion due to low moisture content. No agglutination and blockage were found. This preliminary experimental research provides reference for furfural residue drying unit design.

© 2018 MIM Research Group. All rights reserved

1. Introduction

Furfural ($C_5H_4O_2$) is a kind of organic compound which is used in many fields, such as chemical engineering, pharmaceutical engineering and so on [1]. It is commonly produced from agricultural and forestry byproducts, such as corn cob and sugar cane bagasse. At present, China is the largest producer of furfural [1]. In furfural production processes, furfural residue with high moisture content is generated which is detrimental to environment. Many methods have been proposed to dispose furfural residue [2-3]. Among them, high temperature combustion is an important treatment way which has relatively short workflow [4-6]. The combustion device design is closely relevant to furfural residue's properties, including physical features (e.g., agglutination degree, particle size) and proximate analysis results. Direct combustion of materials with high moisture content will cause difficulty in ignition, low combustion temperature, low combustion efficiency, large exhaust gas heat loss and large exhaust treatment cost [7], so removing moisture in materials (i.e., drying) prior to combustion is always necessary for furfural residue disposal system optimization.

Meng [8] discussed the application of spin flash drying technique in drying furfural residue in which hot air (200 °C) directly contacts the wet furfural residue and removes its moisture to obtain dry product with moisture content less than 6%. Gao et al. [9] did mechanism research of furfural residue drying process in which the effects of particle size,

*Corresponding author: houleizhang@aliyun.com

DOI: <http://dx.doi.org/10.17515/jresm2017.32ds1025>

drying temperature, heating rate and initial load were documented and a few drying models were evaluated. Paddle heat exchanger (or paddle dryer) is a kind of indirect heating equipment with high energy efficiency and low exhaust gas treatment cost that has been used in various sludge and fine-particle material drying processes [10-14]. Different from normal fluid-to-fluid heat exchangers with static heat transfer surfaces that cannot convey solid materials, paddle heat exchanger has rotating heat transfer surfaces. Hollow paddles welded on a hollow shaft have a designed inclined angle. Under operating conditions, when the shaft rotates, the material flows from the inlet end to the outlet end driven by the inclined paddles and at the same time it is heated by the hot shaft-paddle surfaces to reduce its moisture content. The success or not of using paddle heat exchangers strongly depends on the properties of materials to be dried. For instance, two-shaft paddle heat exchangers can dry agglutinating paste materials (e.g., sewage sludge) and non-agglutinating particle materials, but single-shaft paddle heat exchangers are mainly proper for the later. Meanwhile, when the particle size is larger than a critical value, the material flow may be blocked due to small gap between the rotating surfaces and the static surfaces of the shell of the equipment [13]. Up to know, although great progress has been made in modelling drying processes [15-16], it is difficult to quantitatively predict from theory whether a wet material can be successfully dried by paddle heat exchangers or not. Experiment is still the main way of validation.

In this paper we document the basic properties (especially those drying unit design related) of furfural residue and measure the drying characteristics in a lab-scale single-shaft paddle heat exchanger which is simpler than its two-shaft counterpart. The aim is to evaluate the drying feasibility and provide reference for conceptual design of application systems.

2. Experimental Methods

2.1. Property Test

The raw furfural residue sample is shown in Fig. 1 which was collected from a cane sugar plant (Changling Sugar, Guangxi, China) in which furfural was produced from sugar cane bagasse. From the appearance, furfural residue is a mixture of dark brown non-continuous wet particles. The particle size distribution was measured by a series of standard sieves (mesh number 10, 24, 30, 60, 100, 170, 200, 250). By measuring the mass in a specified particle size range, the corresponding mass fraction was obtained. The uncertainty of the corresponding mass weighing is 10 mg [17]. The obtained maximum absolute uncertainty of the mass fraction measurements is 0.00063%. Proximate analysis was performed according to Chinese National Standard GB/T 28731-2012 [17-20]. The uncertainty of the mass measurements in proximate analysis is 0.1 mg. The obtained maximum absolute uncertainty of the measurements of the moisture content (M_{ar}), ash content (A_{ar}), volatile matter content (V_{ar}) and fixed carbon content (FC_{ar}) is 0.06%. The uncertainty of the lower heating value (LHV) measurement is 50 J/g. In order to avoid local pyrolysis due to high temperature, the highest drying temperature should be constrained in design. Pyrolysis process was recorded by HCT-1 TG Analyzer (Beijing Hengjiu Co.). In the pyrolysis experiment, nitrogen with flow rate 50 mL/min was used to provide inert atmosphere. The sample mass was 5.12 mg and the temperature rising rate was set as 10 °C /min. For HCT-1 TG Analyzer, the uncertainties of temperature and mass measurements are 0.1 °C and 0.1 µg respectively [17].

2.2. Drying test

Fig. 2 shows the experimental setup. The specifications of the single-shaft paddle heat exchanger (i.e., dryer) are: heat transfer area 1 m², inclined angle of paddles 4 °, number of paddle pairs 14 and paddle pitch 70 mm. Heat transfer oil was heated in the boiler and

flowed through the hollow shaft and paddles. Furfural residue flowed on the outside of the shaft and paddles and meanwhile the moist content was reduced along the flow path. The oil flow rate was adjusted based on the data of a vortex flow meter (DN32, VF-LUGB24-652, Shanghai Weiliu Co.) and the oil temperatures at the inlet and outlet were measured by thermal resistors (Pt100). In real applications, saturated steam is commonly used as the working fluid. In the present experiment, we adjusted the oil flow rate to make its temperature change along the flow path as little as possible.



Fig. 1. Raw sugar cane bagasse furfural residue.

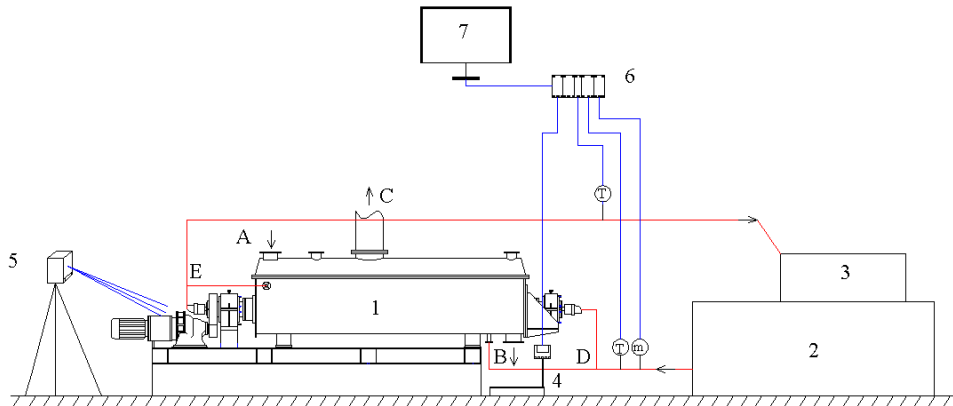


Fig. 2. Experimental setup [17].

1- paddle heat exchanger; 2- boiler; 3- oil tank; 4- electronic scale; 5- photo tachometer; 6- data acquisition unit; 7- computer; A- material inlet; B- material outlet; C- exhaust gas outlet; D- oil inlet; E- oil outlet; m- flow meter; T- temperature sensor

The flow rate of furfural residue at the outlet (m_o) was obtained via real-time continuous weighing with the sampling period of 1 s by an electronic balance (TCS-150) with 0.01 kg accuracy. A computer with data acquisition unit recorded the outlet furfural residue mass continuously and the outlet mass flow rate was then calculated based on the mass vs. time data. The inlet flow rate (m_i) was deduced according to dry matter mass conservation.

$$m_i = \frac{1-x_o}{1-x_i} m_o . \quad (1)$$

In Eq. (1), x_i and x_o are inlet and outlet moisture contents respectively and were tested based on Chinese National Standard GB/T 28731-2012 [18]. Besides, in experiments, the rotating speed of the shaft, which can be adjusted by motor inverter in the range 0~50 rpm, was acquisitioned by an infrared photo tachometer (XSM/C).

3. Results and Discussion

3.1. Properties

The particle size distribution of raw (wet) furfural residue with moisture content of 54.26% is shown in Fig. 3. The data in Fig. 3 are correlated as

$$y = 2.67909x^2 - 16.38295x + 30.03408 \quad (\text{dm} = 0-0.09 \text{ mm}) \quad (2a)$$

$$y = -0.35185x^5 + 9.66385x^4 - 105.86887x^3 + 578.81593x^2 - 1582.94284x + 1745.53418 \quad (\text{dm} = 0.09-1.7 \text{ mm}) \quad (2b)$$

where

$$x = \ln(1000\text{dm}) \quad (3a)$$

$$y = \ln(1000r/\Delta d) \quad (3b)$$

In Eqs. (2a), (2b) and (3a), dm is the average particle diameter in a specified range, e.g., $\text{dm} = 1.2 \text{ mm}$ in the range 0.7-1.7 mm. In Eq. (3b), r and Δd represent the mass fraction in a specified range and the range length respectively, e.g., $\Delta d = 1 \text{ mm}$ in the range 0.7-1.7 mm.

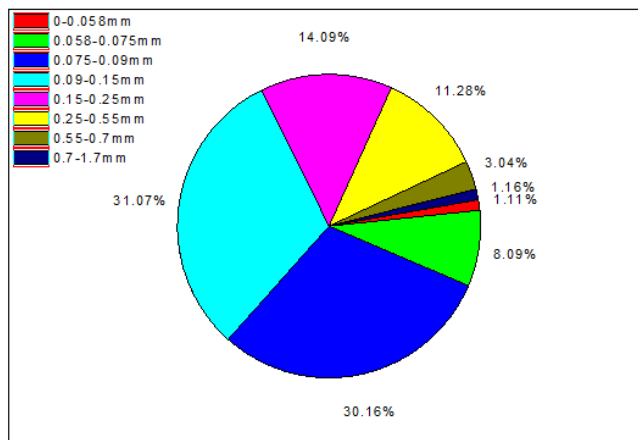


Fig. 3. Particle size distribution of raw furfural residue (moisture content: 54.26%)

According to Fig. 3, the size of most particles (95.8%) is less than 0.55 mm and the average size is 0.174 mm. Fine particles mean that blockage may not happen in single-shaft paddle

heat exchangers. This prediction was validated in flow and drying experiments. Besides, this measurement also provides evidence for selecting proper combustion mode. In the experiment performed by Gao et al. [9], the range of particle sizes is 0.5~10 mm which is very different from that of the sample in this paper although the two samples have similar moisture content. The corresponding bulk density of the present sample is 400 kg/m³ [17] with the uncertainty less than 1 kg/m³ which is also different from that in Ref. [9]. In fact, the present sample is cane sugar bagasse furfural residue but the sample in Ref. [9] is not. This comparison shows that the physical properties (like particle size and bulk density) significantly depend on how the furfural residues are produced. Agglutination is a critical physical problem in paddle heat exchanger applications. By direct observation, we noticed that the furfural residue particles are dispersed, meaning that agglutination may not matter. This was finally checked via drying experiment too.

Table 1 documents the proximate analysis results of raw (wet) furfural residue where M_{ar} is moisture content, A_{ar} is ash content, V_{ar} is volatile content, FC_{ar} is fixed carbon content and LHV is lower heating value. The moisture content (54.26% for the present sample) is the most important parameter for drying unit design. Note that in real applications, the moisture content of raw furfural residue may not be completely the same because of different furfural production processes, deposit, transportation and inevitable non-uniformity. Generally, the highest moisture content is about 60% [1-2]. We assumed the ambient temperature is 25 °C and the latent heat of water evaporation is 2257 kJ/kg at 0.1 MPa. We considered the sensible heat loss of liquid water heating and the latent heat loss of water evaporation in combustion process. From the LHV with moisture content of 54.26%, the LHV with moisture content of 60% can be estimated, which is about 6062 kJ/kg. This result tells that furfural residue with moisture content less than 60% can be used as fuel. A properly designed drying-combustion integration system can generate net heat to outside users.

Table 1. Proximate analysis (as received basis) of raw furfural residue.

M_{ar}	A_{ar}	V_{ar}	FC_{ar}	LHV
54.26%	1.73%	30.07%	13.94%	7301 kJ/kg

Fig. 4 presents the pyrolysis process curves (i.e., TG and DTG). In the range from initial temperature to about 100 °C, TG drops fast which is usually called drying stage. The following stage ranges from 100 °C to about 270 °C, at the end of which most moisture loses. When the temperature is higher than 270 °C, slight pyrolysis initiates. For materials with moisture, when the hot solid surface temperature approaches pyrolysis temperature, the material temperature is usually much lower than the solid surface temperature due to water evaporation cooling effect. Even though, due to non-uniformity of the material particle size distribution and flow distribution, it is possible to generate local high temperature for the material. So, based on this consideration, it is safe to use oil temperature no higher than 270 °C to make sure that no pyrolysis occurs for any particles in any location in a paddle heat exchanger.

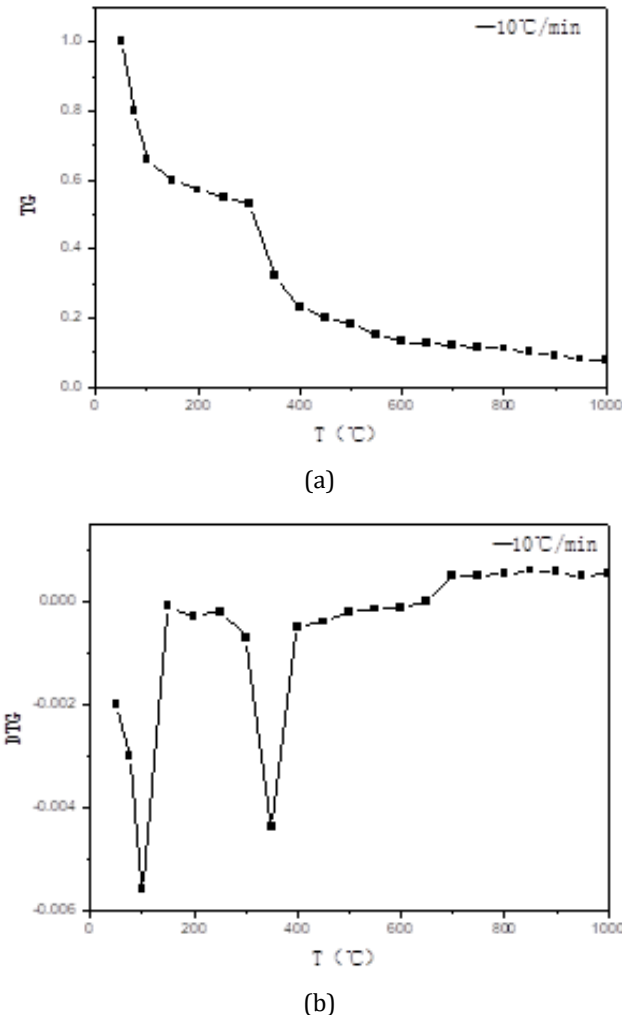


Fig. 4. Pyrolysis process curves of furfural residue (a) TG, (b) DTG

3.2. Drying characteristics

For specified furfural residue, its flow rate m_i at the inlet of the specified paddle heat exchanger in this paper depends on the rotating speed n , whose effect is given in Fig. 5. For the flow test without heating, the maximum relative uncertainty of m_i (or m_0) is less than 0.2% in the specified flow rate range. Approximately, the flow rate increases with the increasing of rotating speed linearly. How to choose n in design is a problem of trade-off. Higher rotating speed increases furfural residue disposal capacity but shortens the residence time which increases the outlet moisture content.

Table 2 documents two cases of drying experiments. In the drying test, the absolute uncertainties of the temperature and moisture content measurements are 0.1°C and 0.02% respectively. The obtained uncertainty of the inlet flow rate (m_i) based on Eq. (1) is about 0.1 kg/h for both cases. More details of the experiments can be found in Ref. [17]. Both cold-state and drying experimental results do not show furfural residue agglutination

on solid surfaces and flow blockage. For imitating saturated steam heating process, we adjusted the oil temperature difference between inlet and outlet to be very small (less than 3 °C). Case II uses higher average oil temperature (181.45 °C) than Case I (132.0 °C). Although the two cases have different inlet moisture contents, the furfural residue flow rates are the same. The outlet moisture content of Case I is close to the inlet moisture content of Case II. We can approximately seem the outlet of Case I as the inlet of Case II but with different oil temperature. Based on the data in Table 2, we can calculate the removed moisture Δm in each case.

$$\Delta m = \frac{x_i - x_o}{1 - x_o} m_i. \quad (4)$$

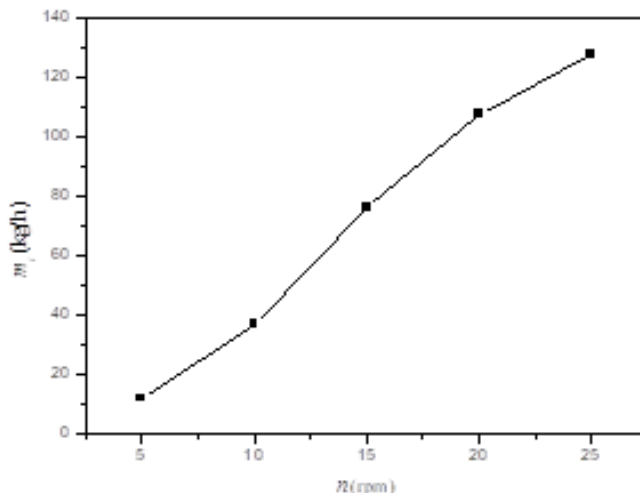


Fig. 5. Flow rate of raw furfural residue (moisture content: 54.26%)

Table 2. Results of drying experiments

Parameters	Case I	Case II
Rotating speed (rpm)	10	10
Inlet oil temperature (°C)	133.9	182.9
Outlet oil temperature (°C)	130.1	180.0
Inlet furfural residue temperature (°C)	22.0	22.0
Inlet mass flow rate of furfural residue (kg/h)	37.0	37.0
Inlet moisture content of furfural residue (%)	54.26	41.31
Outlet moisture content of furfural residue (%)	40.64	15.94

Based on Eq. (4), Δm is 8.49 kg/h for Case I and 11.17 kg/h for Case II. Case II with higher oil temperature removes more moisture than Case I. In the present analysis, assume that the temperature difference between oil and furfural residue (or the oil temperature itself) is more significant and the overall heat transfer coefficient does not change significantly with moisture content in the specified range. It is safe to use 181.45 °C (oil temperature of

Case II) to dry wet furfural residue (with flow rate 37.0 kg/h) from moisture content 54.26% to 15.94% with two 1 m² single paddle heat exchangers in series if we combine Case I and Case II together. The equivalent paddle heat exchanger area is 2 m². For combustion process, less than 20% moisture content is usually acceptable from the viewpoints of technology (i.e., ignition) and economy. Lower outlet moisture content means larger paddle heat exchanger area or more equipment investment. Under such condition, the exhaust gas of drying process will carry dust easily. Trade-off in design is necessary.

3.3. Further discussions

In engineering design, drying unit is suggested to be integrated into the drying-combustion integration system. Fig. 6 shows how the paddle heat exchanger is used in the system. Wet furfural residue is dried in the paddle heat exchanger using saturated steam generated by burning dry furfural residue in the boiler. More steam than needed by drying is output to outside users. Because of the indirect drying feature, most of the exhaust gas generated in the paddle heat exchanger is steam. It is possible to recover and reuse the heat stored in the exhaust gas through proper methods like condensing. If so, the energy efficiency of the drying-combustion integration system will be improved. In China, there are a lot of industrial steam boilers with steam pressure no higher than 1 MPa, including some installed in furfural production factories. The saturation temperature of steam at 1 MPa is about 180 °C which is very close to oil temperature used in Case II. So it is convenient and cheaper to use these boilers to burn dry furfural residue and provide saturated steam to dry wet furfural residue. Detailed analysis and optimization on drying-combustion integration system will be performed later.

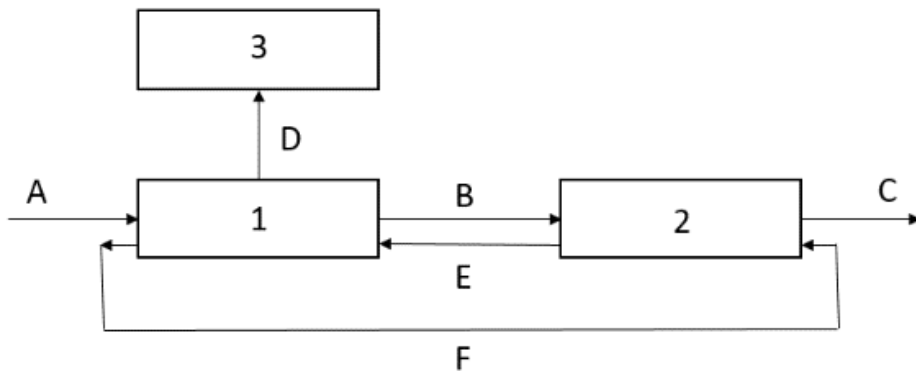


Fig. 6. Furfural residue drying-combustion integration system

1- paddle heat exchanger; 2- boiler; 3- exhaust gas disposal unit; A- wet furfural residue; B- dry furfural residue; C- ash; D- exhaust gas; E- steam; F- condensing water

4. Conclusions

The present work is a preliminary investigation that provides evidence for conceptual design of application systems. The aim is to check the feasibility of using single-shaft paddle heat exchanger to dry wet sugar cane bagasse furfural residue. Measurements of basic properties of furfural residue were performed. The average particle size is 0.174 mm, very different from that in literature. This shows that the particle size significantly depends on how furfural residue is generated. The lower heating value of furfural residue with

moisture content of 54.26% is positive which means that properly designed drying-combustion integration system does not consume net heat in furfural residue disposal processes. Pyrolysis curves were also documented for design need. Furfural residue flow rate and drying characteristics were tested in a lab-scale single-shaft paddle heat exchanger. No agglutination and flow blockage were found. The results confirm that it is feasible to dry wet furfural residue to moisture content of 15.94% with reasonable equipment design and working fluid parameters in the viewpoint of engineering applications. Compared with raw wet furfural residue, the product after drying can be burned more easily and efficiently. This conclusion provides basis for future design of drying-combustion integration system. More research will be performed in the future, e.g., in scale-up performance of furfural residue drying systems based on single-shaft paddle heat exchangers.

References

- [1] Rong, C. Studies on Preparation of Furfural and Comprehensive Utilization of Furfural Residue (in Chinese), Ph.D. Dissertation, Jilin University, Changchun, China, 2005.
- [2] Dai, L., Liu, B. Research progress on furfural residues recycling: a literature review, Proceedings of 2010 International Conference on Environmental Engineering and Applications, Singapore, September 10-12, 2010.
- [3] Yin, Y., Li, A., Mao, L. Progress in utilization of furfural residue utilization technology (in Chinese), Modern Chemical Industry, 2011; 31: 22-24 and 26.
- [4] Bie, R., Yang, L., Lu, H., Li, B., Bao, Y. Experimental study on furfural residue combustion in a fluidized bed (in Chinese), Acta Energiae Solaris Sinica, 2001;22: 291-295.
- [5] Yang, Z. Experimental Studies on Furfural Residue Combustion in Fluidized Bed (in Chinese), Master Thesis, Northeast Dianli University, Jinlin, China, 2012.
- [6] Li, H., Liu, J. Mechanism of bed material agglomeration during fluidized bed combustion of furfural residues, Journal of Xi'an Jiaotong University, 2015; 49: 145-150.
- [7] Che, D. Boilers-Design and Operation, Xi'an Jiaotong University Press, Xi'an, China, 2008.
- [8] Meng, X. Application of spin flash dryer in furfural residue drying (in Chinese), Chemical Equipment Technology, 1995; 16: 10-13.
- [9] Gao, N., Li, A., Mao,L., Yang, J. Drying characteristics of the furfural residues of biomass hydrolyzation, Journal of Biobased Materials and Bioenergy, 2012; 6: 661-668. <https://doi.org/10.1166/jbmb.2012.1294>
- [10] Arlabosse, P., Chavez, S., Lecomte, D. Method for thermal design of paddle dryers: application to municipal sewage sludge, Drying Technology, 2004; 22: 2375-2393. <https://doi.org/10.1081/DRT-200040041>
- [11] Deng, W., Yan, J., Li, X., Wang, F., Lu, S., Chi, Y., Cen, K. Measurement and simulation of the contact drying of sewage sludge in a Nara-type paddle dryer based on batch experiments, Chemical Engineering Science, 2009; 64: 5117-5124. <https://doi.org/10.1016/j.ces.2009.08.015>
- [12] Wang, W., Zhang, H., Liu, X. Research and application prospects of coal slime in paddle dryers (in Chinese), Industrial Boiler, 2015; 1: 34-36.
- [13] Zhang, S., Liu, X., Yang, G., Zhang, H. Drying characteristics of fine-particle lignite in paddle dryers, Defect and Diffusion Forum, 2016; 366: 192-198. <https://doi.org/10.4028/www.scientific.net/DDF.366.192>
- [14] Ding, J., Liu, X., Zhang, H. The calculation and analysis of heat transfer Characteristics of coal slime drying process in single-shaft paddle dryer (in Chinese), Energy Research and Utilization, 2016; (6): 29-32.
- [15] Tsotsas, E., Mujumdar, A. S. Modern Drying Technology - Volume 1: Computational Tools at Different Scales, WILEY-VCH Verlag GmbH & Co. KGaA, Weinheim, Germany, 2007.
- [16] Defraeye, T. Advanced computational modelling for drying processes – A review, Applied Energy, 2014; 131: 323-344. <https://doi.org/10.1016/j.apenergy.2014.06.027>

- [17] Ji, L. The Research on Energy Saving Technology for Thermal System of Sugarcane Factory (in Chinese), Master Thesis, Nanjing University of Science and Technology, Nanjing, China, 2017.
- [18] GB/T 28731-2012: Proximate Analysis of Solid Biomass Fuels (in Chinese), Standards Press of China, Beijing, China, 2012.
- [19] GB/T 212-2008: Proximate Analysis of Coal (in Chinese), Standards Press of China, Beijing, China, 2008.
- [20] Li, Y., Lin, W. Contrast test of proximate analysis of solid biomass fuel (in Chinese), Guangdong Chemical Industry, 2014; 41(16): 60-61.



Research Article

The effect of time delay of fluid flow in a vascularized plate

Onur Yenigün, Turgay Coşkun, Erdal Çetkin*

Department of Mechanical Engineering, Izmir Institute of Technology, Izmir, Turkey

Article Info

Article history:

Received 25 Oct 2017

Revised 25 Jan 2018

Accepted 26 Mar 2018

Keywords:

Furfural residue,
Self-cooling,
Vascular,
Time delay

Abstract

In this study, we show the effect of time delay of coolant fluid flow into a vascularized plate on the peak temperature. Coolant flows along vascular channels which were embedded in a rectangular plate. Two kinds of vascular channel designs were investigated experimentally: parallel and tree-shaped. In the study, the peak temperatures were monitored and the coolant was pumped when the peak temperature reaches to 50°C, 70°C and 90°C. The performance comparison of two distinct designs is based on two criteria: the time required for the steady state condition after the coolant is pumped and the peak temperature after the steady state condition is conformed. The results show that the time required to reach steady-state condition increases as the time delay increases. The parallel and tree-shaped designs show similar performance (time required to reach steady state) with slightly improved performance in the tree-shaped design as the preset temperature for time delay increases. For instance, 4% decrease in the time required to reach steady-state with the tree-shaped design relative to the parallel design was achieved when the preset temperature for time delay is 90°C.

© 2018 MIM Research Group. All rights reserved

1. Introduction

The trend of compact equipment with high processing capability increases the volumetric heat generation rate greatly in the last decade. Compact equipment design constraint limits the increase of heat transfer surface area. Therefore, the literature focus on the maximization of the overall heat transfer coefficient (i.e., minimization of the thermal resistances) such as using nanofluids and phase change materials in order to enhance heat transfer rate [1-4]. Furthermore, not always the rate of generated heat is known, i.e. such as the case of thermal runaway. Therefore, there is a need for uncovering the performance of cooling systems with random heat generation cases. For instance, Çetkin et al. [5] uncovered numerically how the temperature distribution is affected when there is a randomly moving source on a vascular plate. Self-cooling structures promises to provide proper cooling of a structure even under random heat generation cases [5-12].

Materials with the smart feature of self-healing (autonomic healing) was firstly suggested by White et. al. [13] in 2001. They mimicked the healing mechanism of animals, i.e., clot seals the wound. Unlike in the animals, the suggested mechanism in their publication was to embed spheres filled with healing agent. Therefore, this healing could be achieved once, i.e. not repetitive. Later, Hamilton et. al. [14] stated that embedded vascular channels into the structure would create a network similar to the circulatory system which would yield countless time of healing in theory. However, the healing agent during the release may also block the channels which reduces the performance of healing for multiple healing cases.

*Corresponding author: erdalcetkin@iyte.edu.tr

DOI: <http://dx.doi.org/10.17515/jresm2017.33ds1025>

Res. Eng. Struct. Mat. Vol. 4 Iss. 3 (2018) 161-167

Bejan et. al. [15] discussed that embedding vascular channels into a structure can also be used to cool it under an applied heat load. Wang et. al. [16] uncovered how the mechanical strength of a domain with a cavity shaped as the vascular channel network is affected for various vascular channel networks and volume fraction. Later, Cetkin et al. [10] uncovered how the mechanical strength and cooling performance are affected by the volume fraction and the shape of the embedded channel configurations simultaneously. In addition, Cetkin et. al. [5] showed that vascularization provides required cooling even when the cooling requirements are random [14]. Later, the publications uncovered the effect of thermal expansion on vascularized plates which are heated and under a mechanical load [17-18].

The current literature uncovers the cooling performance in steady-state condition. Therefore, fluid should be circulated in the vascular channels continuously. However, this would not be feasible due to the energy usage in random heating load cases. This paper discusses the effect of time delay of the fluid flow in order to uncover what should be the required time for delay when the equipment is heated with a random heat load. The parallel and tree-shaped vascular channel structures were investigated experimentally.

2. Model

The plates of size 170x170 mm with embedded vascularized cooling channels were heated with constant and uniform heating load of 150W from the surface boundary as shown in Fig. 1. The details on the length scales and geometry can be found in our previous publication [19], and the dimensions are also given in Table 1. The rest of the outer boundaries of the vascularized plate is adiabatic (i.e., $\partial T/\partial n=0$). Coolant flows along the embedded vasculature network with the same flow rate for all the designs (0.225 lt/min, $Re = 1198$). The pressure difference between the inlet and outlet boundaries of the cooling channels is the driving force for coolant to flow. The volume of the vascular channels and solid plate are fixed for all the designs. The channel surface area for the tree-shaped and parallel designs are 0.013m^2 and 0.014m^2 , respectively. In addition, the coolant is distilled water.

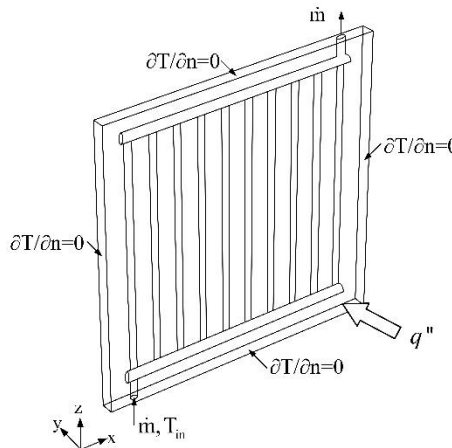


Fig. 1 Cooling plate with embedded circular cross-sectional channels in parallel design: boundary conditions with perspective of the geometry [19]

Two vasculature network is studied in the current paper: parallel design (Fig. 2a) and tree-shaped design (Fig. 2b). In the parallel design, the coolant channels of diameter d_1 are connected to one distributing and one collecting channels of diameter d_0 . In the tree-shaped design, four cooling channels of diameter d_1 is joined to eight channels of diameter d_2 and they are connected to sixteen daughter channels of diameter d_3 . All of the tree-

shaped channels are connected to one distributing and one collecting channels of diameter d_0 with the channels of diameter d_3 .

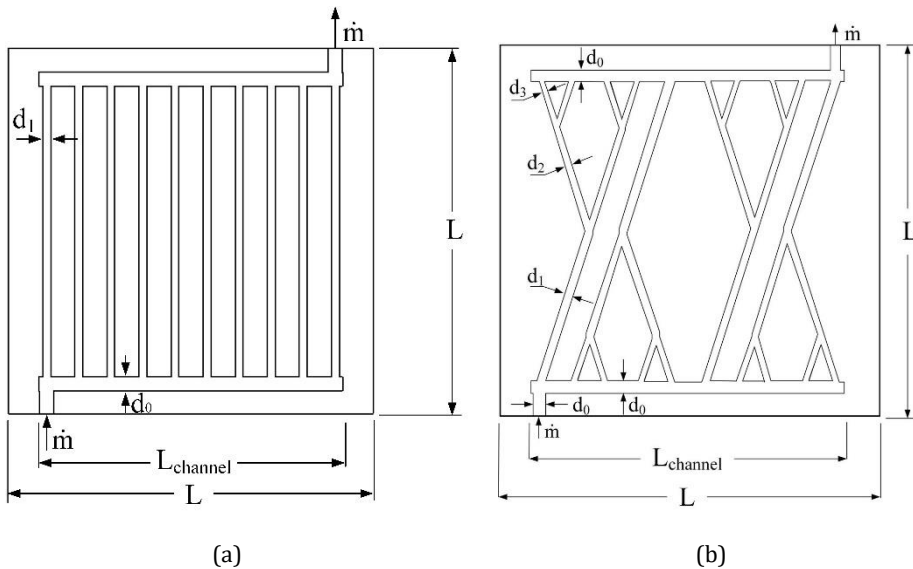


Fig. 2 Cooling plate with embedded circular cross-sectional channels: (a) parallel design and (b) tree-shaped design [19]

Table 1 Dimensions of the competitive designs

Designs	d_0 [m]	d_1 [m]	d_2 [m]	d_3 [m]	L [m]	L_{channel} [m]
Parallel	0.004	0.0025	-	-	0.17	0.15
Tree-shaped	0.004	0.003	0.0025	0.002	0.17	0.15

3. Experimental Method

Figure 3 shows the schematics of the experimental setup. The setup consists of cooled circulating bath, needle valve, turbine flow meter, thermocouples, vascularized plate, thermal camera, silicone flexible resistance and data logger. The circulating water bath regulates constant inlet temperature into the vasculature network. The temperature at the inlet of the vasculature network is also measured to check whether the temperature fluctuates. During the study we have monitored constant inlet temperature (i.e., the fluctuation in the temperature is in the order of the accuracy of the cooled circulating bath). Needle valve and flow meter are used to turn on/off the coolant flow and to measure volume flow rate of the coolant, respectively. Thermocouples were used to measure ambient temperature and coolant at the outlet of the vascular plate in addition to the inlet temperature of the coolant into the vasculature. The vascularized plates used in the experiments were manufactured from 5083 Aluminum. A silicone heater is used to supply constant heat flux to the bottom surface of the vascular plate. The overall heating rate of the silicone heater is 150W. Hioki data logger was used to record measurement data of the flow meter and thermocouples. The peak temperature on the surface was measured with thermal camera which was calibrated before the measurements. The accuracies of each measurement equipment with the error analysis study was given in our previous study of Ref [19] where the temperature distribution of the vascularized structure was documented

under steady state condition (i.e., constant flow rate of the coolant supplied into the vasculature structure in the Ref. [19]).

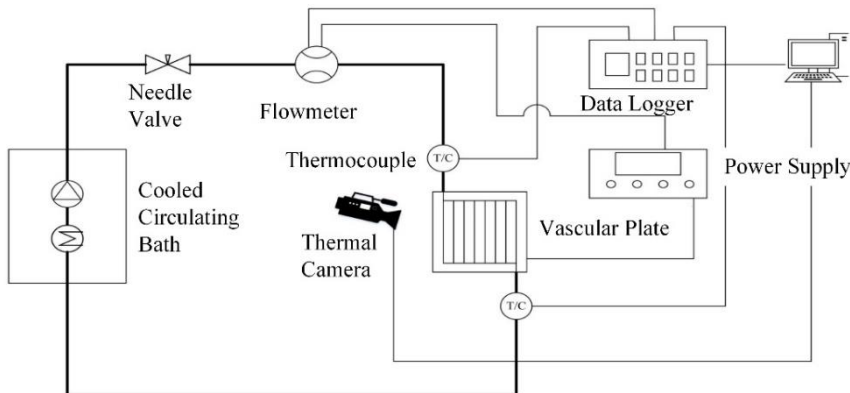


Fig. 3 The schematic of the experimental setup [19]

In the experiment, the coolant fluid in the water bath is cooled down to 20°C. Then, vascular plate was heated by using the silicone flexible resistance. First, there is no coolant flowing in the vasculature. Heating process is continued up to the pre-determined peak temperature value. Then, the needle valve was turned on to supply the coolant into the vasculature. The coolant flows through the needle valve, flow meter and vascular plate, respectively, and then it returns to the circulating bath. The volumetric flow rate of the coolant is 0.225 lt/min and the flow regime is laminar during the process (maximum value of the Reynolds number is 1198). The cooling power of the circulating bath (250W) is greater than the supplied heat from the silicone resistance (150W). Therefore, the inlet temperature of the coolant into the vascularized plate was kept constant. In addition, during the experiment, the maximum temperature on the surface of the plate is monitored via thermal camera. The temperature distribution on the thermal camera and measurements done from the thermocouples were monitored and stored. The experiment is repeated for various pre-determined peak temperatures such as 50°C, 70°C and 90°C. Finally, the required time to reach steady state condition is evaluated with respect to peak temperature values.

4. Results and Discussion

Here, the peak temperature history of the experimental results for two distinct vasculature structures (parallel and tree-shaped) are documented. In addition to the effect of design on cooling, the effect of the cooling time of the vascularized plates are investigated.

First, consider the parallel design of Fig. 2(a) with preset temperatures of 50°C, 70°C and 90°C in order to supply the coolant. The applied heating load increases the temperature of the solid domain in which coolant is trapped, i.e. no flow of coolant. Therefore, the temperature increases in an S-curve characteristic as expected, cf. Fig. 4.

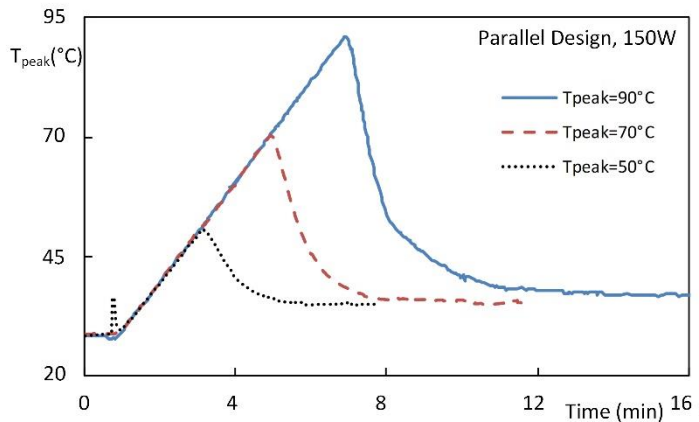


Fig. 4 Parallel design with preset temperature of 50°C, 70°C and 90°C

According to Figure 4, when the cooling fluid delayed, the time required to reach steady state condition increases due to the stored thermal energy in the vascularized plate. The plate reaches steady state condition in approximately 6min, 8min and 11min for the peak temperatures 50°C, 70°C and 90°C, respectively. Steady-state temperatures are approximately the same and measured as 35°C (there is a fluctuation in the order of 1°C due to the variation of the ambient temperature). This also indicates that the proper cooling at the circulating bath and the vasculature was achieved. Figure 4 also shows that the decrease in the peak temperature is steeper when the coolant is being sent to the vasculature. The temperature difference of the coolant flowing along the vasculature and the solid plate yield an exponential peak temperature difference history from the instance that the coolant is pumped to the steady-state condition temperature. Therefore, the peak temperature decreases in a steep fashion after the fluid is pumped until the peak temperature and steady state temperature difference is approximately 50°C.

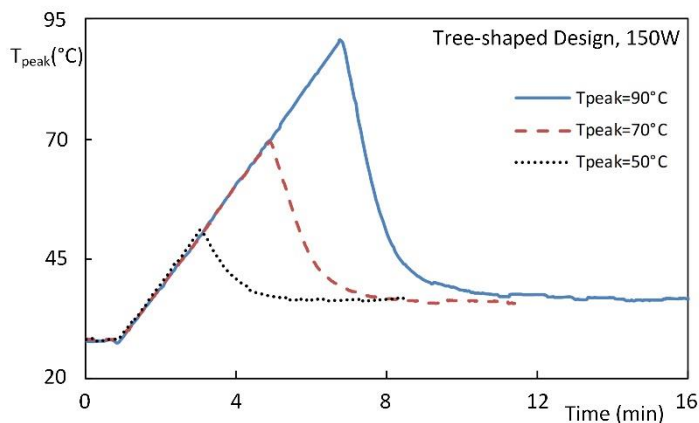


Fig. 5 Tree-shaped design with preset temperature of 50°C, 70°C and 90°C

Next, consider the tree-shaped design with three levels of embedded vascular cooling channels in Figure 2(b). Figure 5 shows that the temperature history from time 0 min to the preset temperature is almost the same with the temperature history of Fig. 4. Because the volume of the coolant and the solid material is fixed, this result is reasonable. They are

not exactly the same due to how non-flowing coolant distributed inside the vasculature and the surface area of the channels are different in Figs. 4 and 5.

Figure 5 shows that the vascularized plate reaches steady state condition approximately in 5min, 8min and 10min for the peak temperatures 50°C, 70°C and 90°C, respectively. Figures 4 and 5 shows that the time required to reach steady state is approximately the same for both parallel and tree-shaped designs. However, the results indicated that the steady-state temperature is being reached faster with the tree-shaped design. The reason of that trend is due to the decrease of the pressure drop in the tree-shaped design relative to the parallel design. Steady-state temperatures were recorded as approximately 36°C for the peak temperatures 50°C, 70°C and 90°C. In addition, the steady state peak temperature is 1°C greater in tree-shaped design relative to the parallel one. However, this difference stays in the calculated error for the experimental analysis.

5. Conclusions

In this study, we showed the effect of time delay on the cooling of a vascularized plate with two distinct channel networks: parallel and tree-shaped designs. The results show that varying the time delay affects the peak temperature, and that the time required to reach steady-state condition is increased by the rise in peak temperature. The temperature history first shows an S-curve characteristic (from time 0 to peak temperature) and then it shows an exponential characteristic (from the peak temperature to the steady-state temperature). Figures 4 and 5 uncover that the time required to reach steady-state condition increases approximately 1 min for every 10°C increment. However, it should be noted here the cooling power of the circulating bath is greater than the supplied heat load. Therefore, the supplied coolant satisfied the requirement of constant temperature at the inlet of the vascularized structure. Otherwise, the steady-state may not be reached. The results show that the parallel and tree-shaped designs yields almost the same steady state temperature (1°C difference exists which is less than the experimental error). However, the steady state temperature is reached faster with the tree-shaped design. For instance, it is 4% less than the parallel design when the preset temperature for time delay is 90°C.

Acknowledgment

The authors acknowledge the funding from the Scientific and Technological Research Council of Turkey.

References

- [1] Shafahi M, Bianco V, Vafai K, Manca O. Thermal performance of flat-shaped heat pipes using nanofluids. International Journal of Heat and Mass Transfer, 2010; 53: 1438-1445. <https://doi.org/10.1016/j.ijheatmasstransfer.2009.12.007>
- [2] Li Y, Xie HQ, Yu W, Li J. Liquid cooling of tractive lithium ion batteries pack with nanofluids coolant. Journal of Nanoscience and Nanotechnology, 2015; 15(4): 3206-3211. <https://doi.org/10.1166/jnn.2015.9672>
- [3] Alshaer WG, Nada SA, Rady MA, Del Barrio EP, Sommier A. Thermal management of electronic devices using carbon foam and PCM/nano-composite. International Journal of Thermal Sciences, 2015; 89: 79-86. <https://doi.org/10.1016/j.ijthermalsci.2014.10.012>
- [4] Ma T, Yang HX, Zhang YP, Lu L, Wang X. Using phase change materials in photovoltaic systems for thermal regulation and electrical efficiency improvement: A review and outlook. Renewable and Sustainable Energy Reviews, 2015; 43: 1273-1284. <https://doi.org/10.1016/j.rser.2014.12.003>
- [5] Cetkin E, Lorente S, Bejan A. Vascularization for cooling a plate heated by a randomly moving source. Journal of Applied Physics, 2012; 112(8): 084906, 2012.

- [6] Cetkin E, Lorente S, Bejan A. Vascularization for cooling and mechanical strength. International Journal of Heat and Mass Transfer, 2011; 54(13-14): 2774-2781. <https://doi.org/10.1016/j.ijheatmasstransfer.2011.02.061>
- [7] Wang KM, Lorente S, Bejan A. Vascular materials cooled with grids and radial channels. International Journal of Heat and Mass Transfer, 2009; 52(5-6): 1230-1239. <https://doi.org/10.1016/j.ijheatmasstransfer.2008.08.027>
- [8] Cho KH. Fluid flow and heat transfer in vascularized cooling plates. International Journal of Heat and Mass Transfer, 2010; 53(19-20): 3607-3614. <https://doi.org/10.1016/j.ijheatmasstransfer.2010.03.027>
- [9] Rocha LAO, Lorente S, Bejan A. Tree-shaped vascular wall designs for localized intense cooling. International Journal of Heat and Mass Transfer, 2009; 52(19-20): 4535-4544. <https://doi.org/10.1016/j.ijheatmasstransfer.2009.03.003>
- [10] Cetkin E, Lorente S, Bejan A. Hybrid grid and tree structures for cooling and mechanical Strength. Journal of Applied Physics, 2011; 110(6): 064910. <https://doi.org/10.1063/1.3626062>
- [11] Cho KH, Lee J, Ahn HS, Bejan A, Kim MH. Fluid flow and heat transfer in vascularized cooling plates. International Journal of Heat and Mass Transfer, 2010; 53: 3607-3614. <https://doi.org/10.1016/j.ijheatmasstransfer.2010.03.027>
- [12] Cho KH, Chang WP, Kim MH. A numerical and experimental study to evaluate performance of vascularized cooling plates. International Journal of Heat and Fluid Flow, 2011; 32: 1186-1198, 2011. <https://doi.org/10.1016/j.ijheatfluidflow.2011.09.006>
- [13] White SR, Sottos NR, Geubelle PH, Moore JS, Kessler MR, Sriram SR, Brown EN, Viswanathan S. Autonomic healing of polymer composites. Nature, 2001; 409: 794-797. <https://doi.org/10.1038/35057232>
- [14] Hamilton AR, Sottos NR, White SR. Self-healing of internal damage in synthetic vascular materials. Advanced Materials, 2010; 22(45): 5159-5163. <https://doi.org/10.1002/adma.201002561>
- [15] Bejan A, Lorente S, Wang KM. Networks of channels for self-healing composite materials. Journal of Applied Physics, 2006; 100(3): 033528. <https://doi.org/10.1063/1.2218768>
- [16] Wang KM, Lorente S, Bejan A. Vascular structures for volumetric cooling and mechanical Strength. Journal of Applied Physics, 2010; 107(4): 044901. <https://doi.org/10.1063/1.3294697>
- [17] Rocha LAO, Lorente S, Bejan A. Vascular design for reducing hot spots and stresses. Journal of Applied Physics, 2014; 115(17): 174904. <https://doi.org/10.1063/1.4874220>
- [18] Cetkin E, Lorente S, Bejan A. Vascularization for cooling and reduced thermal stresses. International Journal of Heat and Mass Transfer, 2015; 80: 858-864. <https://doi.org/10.1016/j.ijheatmasstransfer.2014.09.027>
- [19] Yenigün O, Cetkin E. Experimental and numerical investigation of constructal vascular channels for self-cooling: Parallel channels, tree-shaped and hybrid designs. International Journal of Heat and Mass Transfer, 2016; 103: 1155-1165. <https://doi.org/10.1016/j.ijheatmasstransfer.2016.08.074>
- [20] Bejan A, Lorente S. Design with Constructal Theory, John Wiley & Sons, 2008. <https://doi.org/10.1002/9780470432709>



Research Article

Numerical study of the elasto-plastic buckling in perforated thin steel plates using the constructal design method

Daniel Helbig¹, Marcelo Langhinrichs Cunha², Caio Cesar Cardoso da Silva², Elizaldo Domingues dos Santos², Ignácio Iturrioz¹, Mauro de Vasconcellos Real², Liércio André Isoldi^{*2}, Luiz Alberto Oliveira Rocha^{1,3}

¹ Graduate Program in Mechanical Engineering, Federal University of Rio Grande do Sul - UFRGS, Brazil

² Graduate Program in Ocean Engineering, Federal University of Rio Grande - FURG, Brazil

³ Graduate Program in Mechanical Engineering, University of Vale do Rio dos Sinos - UNISINOS, Brazil

Article Info

Article history:

Received 23 Nov 2017

Revised 09 Feb 2018

Accepted 20 Jun 2018

Keywords:

Post-buckling,

Perforated steel plate,

Computational modeling,

Constructal Design method

Abstract

There are several areas of engineering that use thin plates as structural elements, among them, we can highlight their application in the construction of offshore structures, bridges, ship hulls, and aircraft fuselage. In some design situations, the plates may be subjected to compression stresses and, consequently, they may be under the effect of elastic and/or elasto-plastic buckling. The analysis of the buckling phenomenon presents significant differences between one-dimensional elements, such as beams and columns, and two-dimensional elements, such as plates. The buckling phenomenon is directly related to dimensional, constructive and/or operational aspects. In this sense, the presence of perforations in plates causes a redistribution of their stresses, affecting not only their resistance but also their buckling characteristics. In order to solve the problem of elasto-plastic buckling in thin steel plates with perforations, we used computational models developed in Ansys^(R) software, which is based on the Finite Element Method (FEM). For the analysis, it was considered perforated plates with constant thickness h for the relationships $H/L = 1.0$ and $H/L = 0.5$, where H is the plate width and L is the plate length. For the volume fraction Φ , i.e., the ratio between the volume of the perforation and the volume of the plate, the following values were considered: 0.08; 0.10; 0.15; 0.20 and 0.25. In addition, the plates were considered to have centralized perforations with the following geometric forms: longitudinal oblong, transverse oblong, elliptic, rectangular, diamond, longitudinal hexagonal, and transverse hexagonal. The shape variation of each perforation type occurs through the ratio H_0/L_0 , being H_0 and L_0 the characteristics dimensions of perforation. The Constructal Design method was employed to define the range of possible geometries for the perforated plates, allowing an adequately comparison about the von Mises stress distribution among the studied cases. The results show that the geometric shape variation, for all analyzed perforation types, leads to an optimum geometry.

© 2018 MIM Research Group. All rights reserved

Introduction

The growing use of the steel plates in structures is directly related to the advantages that this element possesses when compared with other construction types. The high strength of the material to the several stress states, for instance, makes it possible to withstand great internal forces, in spite of having cross-sectional areas relatively small, what turns them lighter [1].

*Corresponding author: liercioisoldi@furg.br

DOI: <http://dx.doi.org/10.17515/resm2017.37ds1123>

Res. Eng. Struct. Mat. Vol. 4 Iss. 3 (2018) 169-187

As for the thin plates, these are structural elements very used in the naval, aerial, and automotive industries, as well as in the civil construction. It stands out for its use in the construction of shipyards cranes, petroleum platforms, floating docks, ship hulls, and in the fuselage of airplanes. According to [2], thin plates are widely used in structures because they have excellent performance at imposed stresses, with the reduced weight of their elements, and, if added chrome, nickel or zinc to plates, high corrosion resistance. When a flat plate is subjected to transverse or axial loads, it develops stresses due to axial force, shear, bending, and torsion [3]. For [4] some factors must be analyzed with extreme care in the design of naval and offshore structures. The idealization and the design of a structural element should satisfy specific requirements of resistance, rigidity, and stability. In its great majority, structures as the ship hulls are formed basically by the association of beams, columns and plates, which are usually submitted to compression loads. In this context, when a slender structural element is subjected to compressive strengths, an extremely important phenomenon called buckling may occur, that is, making the element susceptible to instability.

Moreover, the designers should observe carefully the presence of perforations in plates. These can be used with the objective of decrease the total weight of the structure or to make possible the people's access to certain sections or services, or still, as elements with an aesthetic purpose. However, the inclusion of perforations in the plates causes a redistribution of their stresses, and may even lead to modifications in their mechanical strength and in the buckling characteristics [5]. Other aspects related to perforations, such as the geometry, the dimension and the positioning of the perforation, influence directly in the performance of a plate submitted to uniaxial compression [6].

Several researchers have studied the mechanical behavior of thin steel plates subjected to compression, and among them can be cited: [7] determined the values of critical buckling loads in rectangular plates with centralized perforations and subjected to biaxial loading using FEM; [8] have developed, validated and summarized analytical expressions whose purpose is to estimate the influence of single or multiple perforations in determining the value of the critical buckling load of plates in bending or compression; [9] applied the Constructal Design method for the optimization of perforated thin steel plates submitted to the elastic buckling; [10] used the Constructal Design method to evaluate the influence of the type and the shape of centralized perforations in thin steel plates subjected to linear elastic and nonlinear elasto-plastic buckling; and [11] studied the mechanical behavior to nonlinear buckling of thin rectangular steel plates with rectangular perforations and rounded vertices subjected to uniform compression.

Although there exists a significant number of scientific works addressed to the study of the elastic buckling in plates, there is a reduced number of these referring to the elasto-plastic buckling. This paper proposes to analyze the mechanical behavior of perforated thin steel plates subjected to uniaxial compression, using the computational modeling allied to the Constructal Design method for the generation of limit curves for elasto-plastic buckling. In this context, the type, the shape and the size of the perforation are essential parameters to be analyzed.

In order to aid in understanding the next sections of this article, a list of abbreviations and a list of symbols are presented in the Appendix.

2. Buckling and Post-Buckling of Plates

As already mentioned, according to [4], the majority of the parts that integrate a naval structure are composed of plates, beams and columns, which are, in several situations, subjected to compressive loads. Structural components as plates, for instance, when submitted to compression or tension forces, possess differentiated behavior. Plates axially

tensioned develop shear stresses, on the other hand, when submitted to compressive strengths it can occur its transverse deflection, which is called buckling. Therefore, it is extremely important considering the buckling phenomenon in the procedures that involve the structural design of naval and offshore structures. Evidently, this procedure should be used for any structural component that is under the influence of the buckling phenomenon.

When a thin plate subjected to compression reaches its critical load value P_{cr} , the plate undergoes a sudden transverse deformation and may lose its ability to withstand loading, which would result in the collapse of the structure. The transverse deformation is curvilinear and graphically shows the buckling phenomenon. Moreover, according to [12], the application of a compression load, but less than the critical load value, does not cause the buckling phenomenon. In this case, a small perturbation (small lateral load or small initial curvature) causes a curvilinear deformation (lateral displacement) in the plate, but with the retreat of this, the plate returns to its initial configuration. However, for the least increase of the load beyond the critical value, a great transverse displacement occurs in the structure, that can cause the collapse of the plate.

According to [13], the analytical solution to the problem of elastic buckling in thin steel plates without perforation subjected to uniaxial compression is:

$$P_{cr} = k \frac{\pi^2 D}{H^2} \quad (1)$$

where, P_{cr} is the critical load per unit of length, π is a mathematical constant, D is the plate bending stiffness, and k is a function of the aspect ratio H/L . The plate bending stiffness and the buckling coefficient are defined, respectively, by:

$$D = \frac{Eh^3}{12(1-\nu^2)} \quad (2)$$

$$k = \left(m \frac{H}{L} + \frac{1}{m} \frac{L}{H} \right)^2 \quad (3)$$

being, E and ν , respectively, the modulus of elasticity and the Poisson's ratio of the plate's material, h the plate thickness, and m the number of half-waves of the deformation pattern in the x -axis direction.

A thin plate does not enter in collapse soon after the occurrence of the elastic buckling, but actually it can support loads significantly larger than the critical load without deforming excessively. The behavior of plates differs from that expected when considering the behavior of elastic bars submitted to compression that only withstands a slight increase in the load before excessive deformation of the bar occurs (see Fig. 1). The additional post-buckling resistance of thin plates is due to several factors however, the main one is that the deformed shape of the buckling plate cannot be developed from the pre-buckling configuration without a redistribution of the stresses in the mid-plane along the plate. This redistribution, which is ignored in the theory of small displacements of elastic buckling, usually favors the less rigid regions of the plate and causes an increase in plate efficiency. One of the most common causes of this redistribution is associated with the boundary conditions in the plane of the loaded edges of the plate [14].

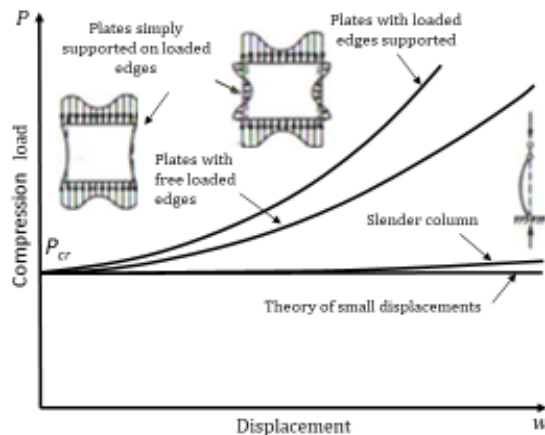


Fig. 1 Post-buckling behavior in slender plates, adapted of [15]

The load that defines the collapse of a plate, in its elasto-plastic behavior, is called post-critical or ultimate load, being represented by P_u . However, as already mentioned, the final load capacity of a plate is not restricted to the occurrence of elastic buckling, i.e., the plates resist load higher than the critical load, which allows an increase of load after the occurrence of elastic buckling [12]. Still in agreement with [12], the capacity of the plates support this load increment is associated with the formation of a membrane force that stabilizes the displacement through a transverse tension (see Fig. 2). When the external load is increased in order to cause the plate buckling, it occurs a non-uniform distribution of the stresses caused by the external load. This provides an increased resistance, which is due to the fact that the transverse fibers are tensioned after the buckling, tending to stabilize the longitudinal fibers.

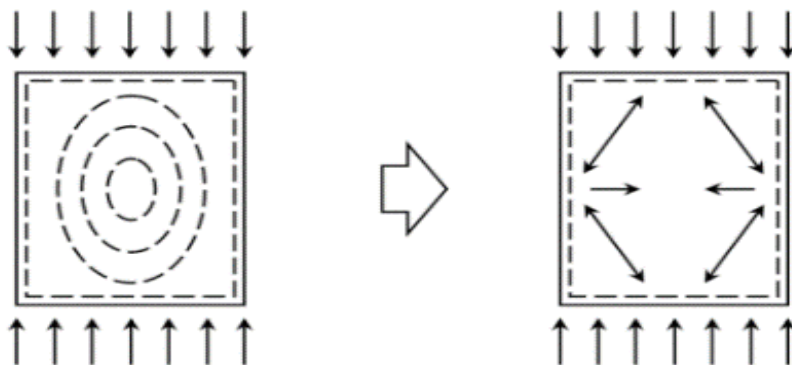


Fig. 2 Redistribution of stresses in the post-buckling critical state [12]

As described above, unlike the behavior of bars, plates exhibit significant resistance after the occurrence of buckling. In addition, if this post-critical resistance is fully utilized, a structural, efficient and economic design may be obtained [16]. According to [17] the post-critical loading reserve is not unlimited, and according to experimental results, the plate reaches the collapse when the maximum compressive stress at the edges not charged reach the elastic limit. Still according to [17], Bleich proposed in 1924 the Eq. 4 to calculate

buckling of plates in the elasto-plastic regime, where $\tau = E_t/E$, and E_t corresponds to the steel tangent modulus of elasticity.

$$\frac{\partial^4 w}{\partial x^4} + 2\sqrt{\tau} \frac{\partial^4 w}{\partial x^2 \partial y^2} + \frac{\partial^4 w}{\partial y^4} + \frac{\sigma_x h}{D} \frac{\partial^2 w}{\partial x^2} = 0 \quad (4)$$

In Eq. 4, the term $\sqrt{\tau}$ is the plastic reduction factor of a plate subjected to uniform compression stress in one direction, being this factor variable with the type of loading and with the boundary conditions of the plate. According to [17], the analysis of the differential equation proposed by von Karman, 1910, and after by Bleich, 1924, to elasto-plastic analysis is quite complex, being normally necessary resort to numerical and computational methods.

3. Constructal Design Method

The Constructal Theory stands out for present time context and for the perception of the design importance of natural structures. As a basic reference, it is based on the perception that the design of natural structures is directly related to the occurrence of a physical phenomenon, which occurs in small and large systems such as rivers, traffic in cities, vascularized living tissue, the dissemination of ideas, among others. Its guidelines and its major advances in science are directly related to the studies developed by its founder, Adrian Bejan, and researchers who use it in different areas of knowledge. The line of reasoning where forms from nature are accepted, observed, and copied are still present today. However, the Constructal Theory, according to [18], proposes the inversion of this thought, that is, initially invokes the Constructal law and with that, theoretically, the architecture of the form is deduced. Then, the theoretical configuration obtained in the deduction is compared with that of the natural phenomena, and the agreement between the geometries is what validates the Constructal Law.

According to [19], the Constructal Law for flow generation and configuration is defined as: "For a finite-size flow system to persist in time (to live), its configuration must evolve in such a way that provides greater and greater access to the currents that flow through it". This law corresponds to the basis of the Constructal Theory and represents a new extension of thermodynamics: the thermodynamics of systems out of balance and with constraints. Some confuse the Constructal Law with an assumed natural evolutionary trend with toward "more flow," which is not correct. The natural tendency is to evolve freely into flow configurations that offer greater access to what flows, not more flow [20]. According to [21], in summary, the evolution of systems is strictly connected with the possibility of their morphing configuration, permitting that the new configurations replace existing configurations, to perform better (Constructal Law). This self-standing law of design has both local and global significance. It shows a fascinating connection between the Nature as a whole and what this law holds in our world. The paths of all natural flow systems (i.e., animate and inanimate systems) are drawn together and can be described and understood under a unified view. The application of the Constructal Law according to [18] occurs through the Constructal Method, called Constructal Design, and serves to predict many phenomena in nature and designs in engineering. This method is used to obtain configurations that optimize the flow systems through the optimal distribution of imperfections.

3.1 Constructal Design Application

The application of the Constructal Design method allows an adequate evaluation of the influence of the geometric configuration on the mechanical performance of a physical system. Taking into account that all the geometries proposed by the Constructal Design

method are evaluated, it can be said that there is a geometric optimization procedure through an exhaustive search process. Thus, in order to apply the Constructal Design method, it is fundamental to define some parameters, such as objective functions, degrees of freedom and constraints. After the definition of these parameters, it is possible to generate infinite geometries, enabling the application the exhaustive search method. However, according to [22] and [23], if the degrees of freedom and/or parameters are many, another optimization method can be used.

Here, the objective function seeks to maximize the ultimate stresses by varying the degrees of freedom H/L and H_0/L_0 . The degrees of freedom relate, respectively, the width H to the length L of the plate and the width H_0 to the length L_0 of the perforation. For H/L , two possibilities were adopted: $H/L = 1.0$ and $H/L = 0.5$, while for H_0/L_0 several possible values were considered (being related to the perforation type and the problem constraints). The variables H , L , H_0 and L_0 as well as the perforation types used in this work are presented in Fig. 3. It is worth to mention that the plate without perforation, used to verify the computational model, is presented in Fig. 3a. Besides, values of $H = 1000.00$ mm and $L = 2000.00$ mm were considered for the plates with $H/L = 0.5$ and $H = L = 1414.21$ mm for the plates with $H/L = 1.0$.

It was adopted, with the purpose of adequately comparing the different types of perforation and as a restriction to the resolution of the buckling problem, a fraction (Φ) for the perforation volume. This volume fraction is a function of the characteristic dimensions of each perforation type, being defined, respectively, for longitudinal oblong, transverse oblong, elliptical, rectangular, diamond, longitudinal hexagonal and transverse hexagonal cut out, as:

$$\Phi = \frac{V_0}{V} = \frac{\left((L_0 - H_0)H_0 + \frac{\pi}{4}H_0^2\right)h}{HLh} = \frac{(L_0 - H_0)H_0 + \frac{\pi}{4}H_0^2}{HL} \quad (5)$$

$$\Phi = \frac{V_0}{V} = \frac{\left((H_0 - L_0)L_0 + \frac{\pi}{4}L_0^2\right)h}{HLh} = \frac{(H_0 - L_0)L_0 + \frac{\pi}{4}L_0^2}{HL} \quad (6)$$

$$\Phi = \frac{V_0}{V} = \frac{(\pi H_0 L_0 h)/4}{HLh} = \frac{\pi H_0 L_0}{4HL} \quad (7)$$

$$\Phi = \frac{V_0}{V} = \frac{H_0 L_0 h}{HLh} = \frac{H_0 L_0}{HL} \quad (8)$$

$$\Phi = \frac{V_0}{V} = \frac{(H_0 L_0 h)/2}{HLh} = \frac{H_0 L_0}{2HL} \quad (9)$$

$$\Phi = \frac{V_0}{V} = \frac{H_0(L_1 + L_2)h}{HLh} = \frac{H_0(L_1 + L_2)}{HL} \quad (10)$$

$$\Phi = \frac{V_0}{V} = \frac{L_0(H_1 + H_2)h}{HLh} = \frac{L_0(H_1 + H_2)}{HL} \quad (11)$$

where, V_0 represent the perforation volume, V the total volume of the plate without perforation and h the plate's thickness.

For all studied cases in this work, plates with the total area without perforation of 2.00 m^2 and thickness of 10.00 mm were considered. In addition, as a geometric constraint, the

minimal distance between de cut out edge and the plate edge is $H-H_0 = 200.00$ mm and $L-L_0 = 200.00$ mm, respectively, in transverse and longitudinal directions (see Figs. 3b to 3h).

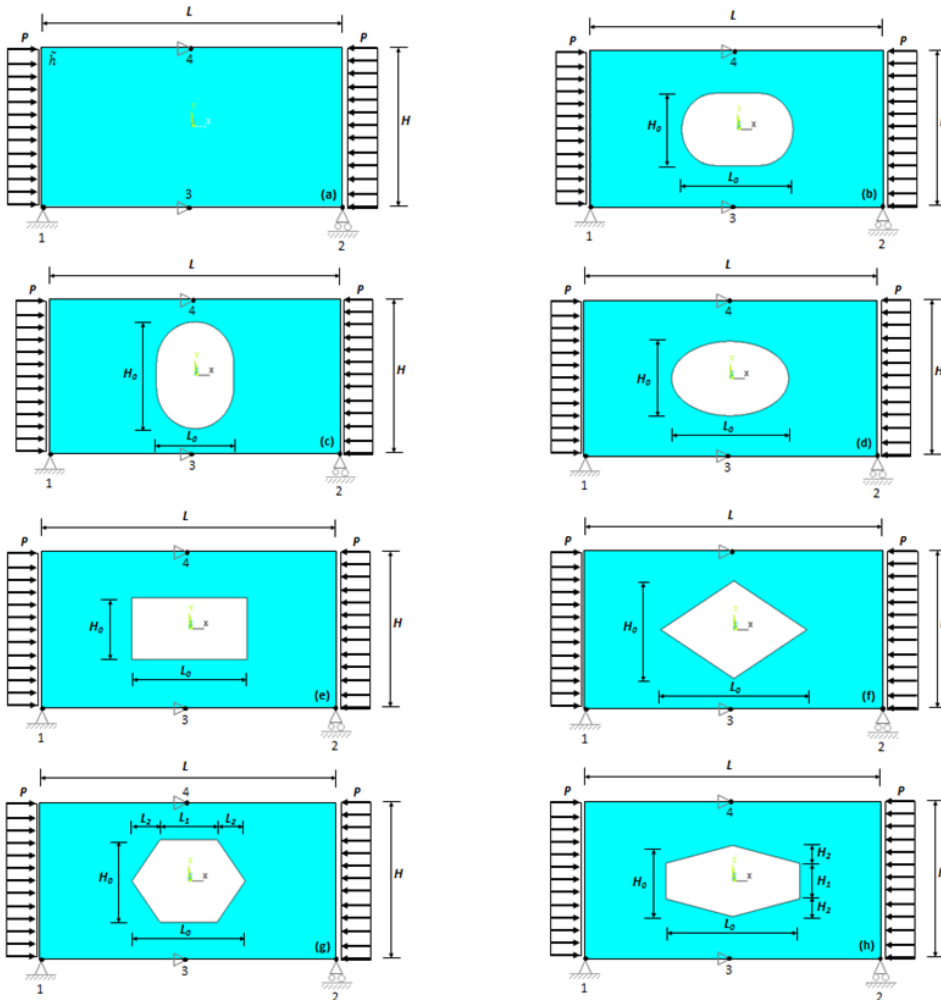


Fig. 3 Plate with: (a) no perforation, (b) longitudinal oblong perforation, (c) transverse oblong perforation, (d) elliptical perforation, (e) rectangular perforation, (f) diamond perforation, (g) longitudinal hexagonal perforation, and (h) transverse hexagonal perforation

5. Computational Models

The computational model used in this work to solve the problem of elasto-plastic buckling of thin steel perforated plates was developed in Ansys® software. For all numerical simulations, the SHELL93 finite element was adopted (see Fig. 4). This element, that can be used for the modeling of plates and shells, has eight nodes with six degrees of freedom in each node, being 3 translations and 3 rotations in the x , y , and z directions. The interpolating polynomials responsible for the deformation form are quadratic in both plane directions and the finite element in question can incorporate plasticity, hardening, and large deformations [24].

An example of discretization and mesh generation for the computational domain, using the SHELL93 finite element, is presented in Fig. 5. In this figure, the compression load P , the length L , the width H and the constraints are indicated. The plate has a constant thickness h of 10.00 mm. Concerning the boundary conditions, it was considered that the plates have all edges simply supported, i.e., all nodes along the four edges are restricted to deflection in z direction. Besides, the displacement in x direction is restricted at nodes 1, 3 and 4 as well as the displacement in y direction is restricted at nodes 1 and 2.

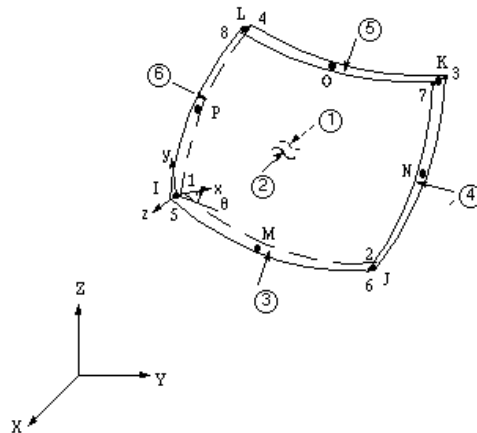


Fig. 4 SHELL93 element [24]

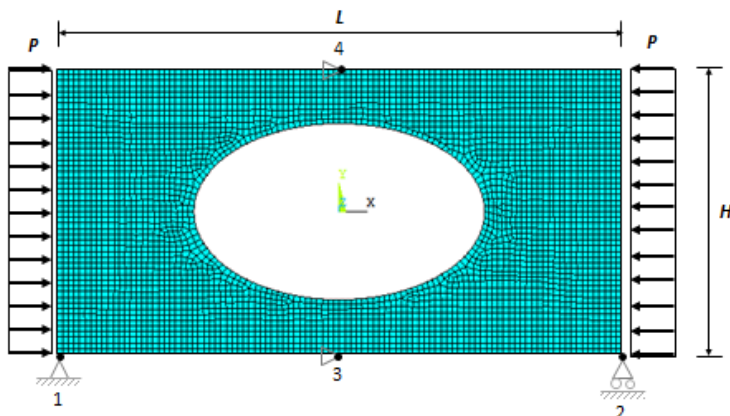


Fig. 5 Reference model generated in ANSYS®

5.1 Elastic and Elasto-plastic Plate Buckling

The numerical procedure used to calculate the load that causes elastic buckling is based on an analysis of eigenvalues and eigenvectors. Once assumed that the structure presents a linear elastic behavior, a structural instability is foreseen, being the focus of the study the verification of the load that provokes the elastic buckling of the plate. For this analysis type, that involves the equilibrium conditions of the finite element equations, it is necessary the solution of homogeneous algebraic equations, where the smallest eigenvalue and eigenvector correspond, respectively, to the critical buckling load and the elastic deformation mode of the structure [25].

This consideration is necessary because the exact post-buckling problem does not allow for a direct analysis due to problems of response discontinuities at the bifurcation point. Starting from the first elastic buckling mode configuration, [26] defines that the maximum value to be assumed for the initial imperfection should obey the relationship $H/2000$, where H represents the width of the plate. Then, the ultimate load on the plate can be found using as reference the load $P_y = \sigma_y t$, where σ_y represents the material yielding strength. This load should be applied in small loading increments on the plate in the direction parallel to the x -axis. As already adopted in [27], for each load increment the Newton-Raphson method is used to determine the displacements corresponding to the equilibrium configuration of the plate through the equations:

$$\{P\}_{i+1} = \{P\}_i + \{\Delta P\} \quad (12)$$

$$\{\psi\} = \{P\}_{i+1} - \{F_{NL}\} \quad (13)$$

$$[K_t]\{\Delta U\} = \{\psi\} \quad (14)$$

$$\{U\}_{i+1} = \{U\}_i + \{\Delta U\} \quad (15)$$

where $[K_t]$ is the updated tangent stiffness matrix, $\{\Delta U\}$ corresponds to the vector of incremental displacements required to achieve the equilibrium configuration, $\{F_{NL}\}$ represents the vector of internal nonlinear nodal forces and $\{\psi\}$ is the vector of unbalanced forces. The vectors $\{U\}_i$ and $\{U\}_{i+1}$ correspond to the displacements, while the vectors $\{P\}_i$ and $\{P\}_{i+1}$ correspond to the external loads applied, to two successive equilibrium configurations of the structure, respectively.

If at a certain load level the convergence can not be reached, or in other words, a finite displacement increment can not be defined so that the unbalanced forces vector $\{\psi\}$ is nullified, this means that the structure failure load has been achieved. This occurs because no matter as large as the displacements and strains can be, the stresses and internal forces can not enhance as it would be necessary to balance the external loads. Therefore, in this case, the maximum resistance capacity of the material was reached [27].

The external compression load on the plate, used in this work for the elasto-plastic buckling analysis, was divided into 100 load increments with a maximum of 200 iterations for each load increment.

6. Results and Discussion

Initially, the results will be presented for the verification of the computational model for the linear elastic buckling analysis and validation of the computational model for the nonlinear elasto-plastic buckling analysis. Then, the thin steel plates with $H/L = 1.0$ and $H/L = 0.5$, with various central perforation types (elliptical, rectangular, diamond, longitudinal hexagonal, transversal hexagonal, longitudinal oblong and transversal oblong), with different sizes ($\Phi = 0.08, 0.10, 0.15, 0.20$ and 0.25) and for different geometric forms (obtained by the H_0/L_0 variation) are subjected to elasto-plastic buckling.

6.1 Verification and Validation

The computational model verification for the analysis of elastic buckling was performed by comparing the result of the critical load of a thin plate of steel without perforation with the analytical solution given by Eq. 1. It was considered a simply supported plate in its four

edges, with the following mechanical and dimensional properties: $E = 210 \text{ GPa}$, $\nu = 0.30$, $\sigma_y = 250 \text{ MPa}$, $H = 1000.00 \text{ mm}$, $L = 2000.00 \text{ mm}$ and $h = 10.00 \text{ mm}$. It was used a structured and converged mesh, generated with the assistance of a finite square element of side 20.00 mm, obtaining a critical stress of $\sigma_{cr} = 75.37 \text{ MPa}$. This value, when compared to the analytical result ($\sigma_{cr} = 75.92 \text{ MPa}$), represents a difference of -0.72%, verifying the developed computational model.

After that, the computational model validation for the analysis of elasto-plastic buckling was performed considering the value of the ultimate load experimentally obtained in [26] for the comparison. For this purpose, a thin steel plate was used, simply supported in the four borders, with the dimensions $H = L = 1000.00 \text{ mm}$ and $h = 20.00 \text{ mm}$, and with the mechanical properties: $E = 210 \text{ GPa}$, $\nu = 0.30$, $\sigma_y = 350 \text{ MPa}$, with centralized circular perforation with diameter of 300.00 mm. The computational domain was discretized using a finite element with the maximum size of 20.00 mm. The ultimate stress determined experimentally in [26] was of $\sigma_u = 213.50 \text{ MPa}$, and the result obtained by numerical simulation in this work was of $\sigma_u = 217.00 \text{ MPa}$, which represents a difference of 1.64%, validating the proposed computational model.

6.2 Normalization of the Limit Stress

Here the objective is to define the limit curve that prevents the occurrence of elasto-plastic buckling. To do so, it is necessary to normalize the ultimate stresses, by means the equation:

$$NLS_{EP} = \frac{\sigma_u}{\sigma_y} \quad (16)$$

where NLS represents the normalized limit stress and the subscript EP refers to elasto-plastic buckling. For all studied cases, the following properties of the material were considered: $E = 210 \text{ GPa}$, $\nu = 0.30$, $\sigma_y = 250 \text{ MPa}$ and $h = 10.00 \text{ mm}$, respectively, for modulus of elasticity, Poisson's ratio, material yielding strength and thickness of the plate.

The H_0/L_0 variation, i.e. the perforation shape variation, allows the generation of an elasto-plastic buckling limit curve for each perforation size and for each perforation type. To exemplify, the plates with $H/L = 1.0$ and $H/L = 0.5$, for $\Phi = 0.20$, having an elliptical perforation were considered, being its limit curves showed in Figs. 6a and 6b, respectively. The NLS_{Max} and NLS_{Min} factors are indicated in Fig. 6, corresponding to maximum and minimum normalized limit stresses and identify, respectively, the optimal geometry and the worst geometry. Regarding the normalized stresses, it was found that, in several situations and for several values of H_0/L_0 , the stresses acting on the plates exceeded the limit to elastic buckling.

So to take into account all studied perforation types the following nomenclature was employed: elliptic (E), rectangular (R), diamond (D), longitudinal hexagonal (LH), transverse hexagonal (TH), longitudinal oblong (LO), and transverse oblong (TO). Therefore, Figs. 7 to 11 show the elasto-plastic buckling limit curve for the plates with $H/L = 1.0$ and $H/L = 0.5$, for all volume fractions Φ and all type of perforations.

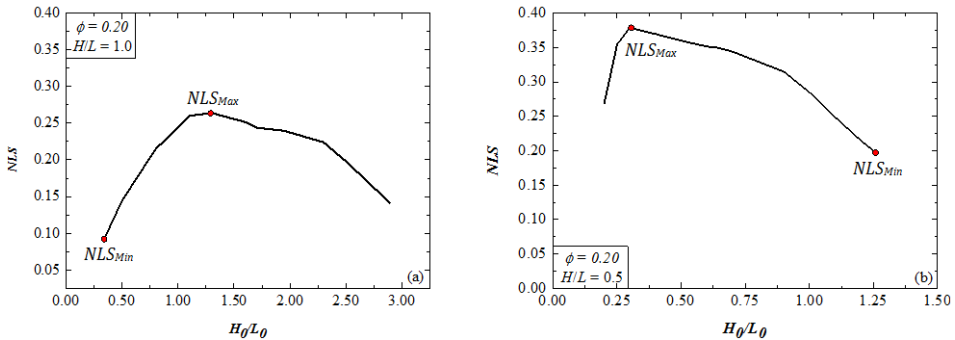


Fig. 6 Limit curve for the occurrence of elasto-plastic buckling in plates with elliptical perforation, for $\Phi = 0.20$: (a) $H/L = 1.0$ e (b) $H/L = 0.5$

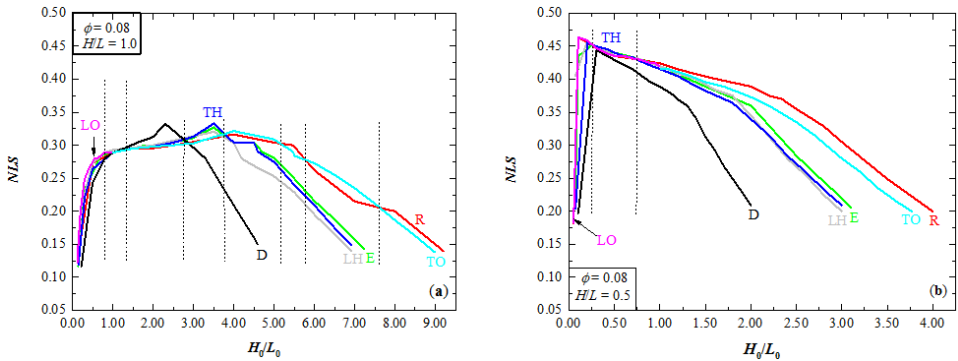


Fig. 7 Limit curves for the occurrence of the elasto-plastic buckling for all types of perforation, and for $\Phi = 0.08$: (a) $H/L = 1.0$ e (b) $H/L = 0.5$

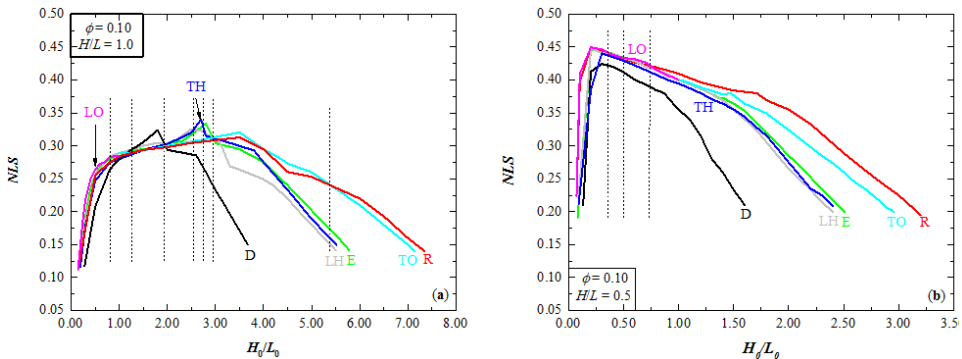


Fig. 8 Limit curves for the occurrence of the elasto-plastic buckling for all types of perforation, and for $\Phi = 0.10$: (a) $H/L = 1.0$ e (b) $H/L = 0.5$

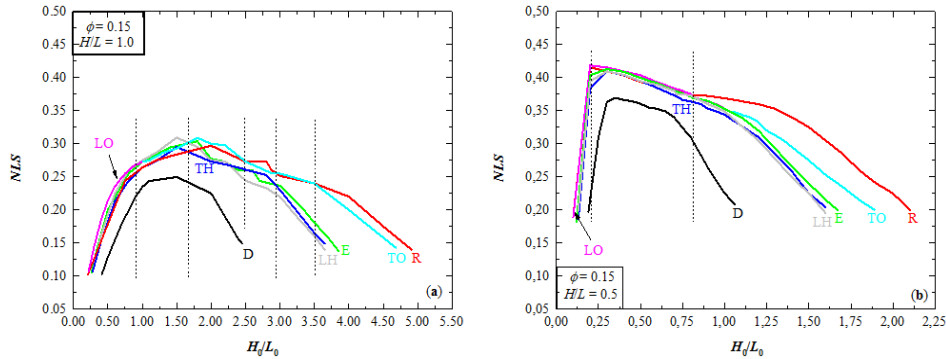


Fig. 9 Limit curves for the occurrence of the buckling for all types of perforation, and for $\Phi = 0.15$: (a) $H/L = 1.0$ e (b) $H/L = 0.5$

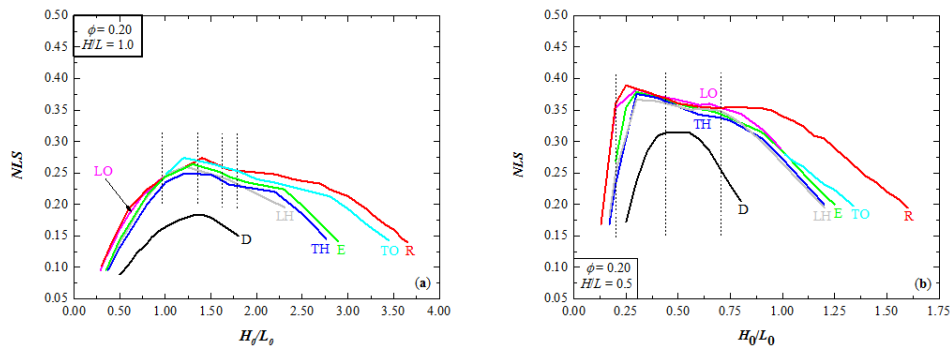


Fig. 10 Limit curves for the occurrence of the elasto-plastic buckling for all types of perforation, and for $\Phi = 0.20$: (a) $H/L = 1.0$ e (b) $H/L = 0.5$

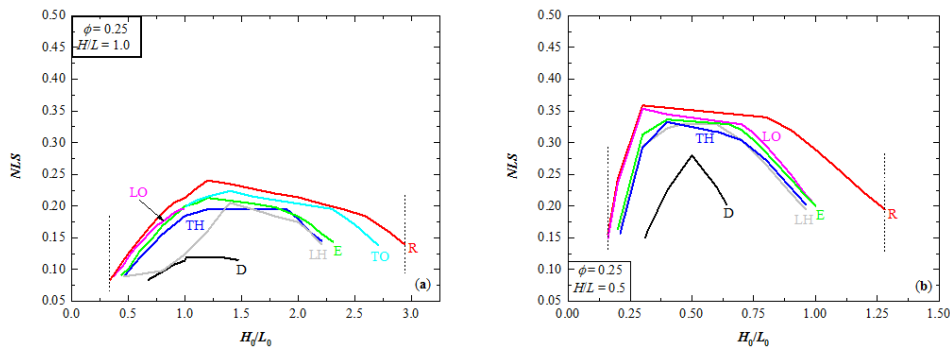


Fig. 11 Limit curves for the occurrence of the elasto-plastic for all types of perforation, and for $\Phi = 0.25$: (a) $H/L = 1.0$ e (b) $H/L = 0.5$

The Figs. 7-11 show some recurrent aspects for the mechanical behavior of the limit curves considering the elasto-plastic buckling. Among them, in a general way, it is possible to highlight that: first, the plates with rectangular perforation present the greatest range for the variation of H_0/L_0 , and those with diamond perforation, the least range; second, there is a graphical similarity in the representation of the limit curves for $\Phi = 0.08$ and 0.10

and for $\Phi = 0.15, 0.20 and 0.25 ; third, the plates with transverse hexagonal, longitudinal hexagonal and elliptical perforation type, present values very close to H_0/L_0 ; fourth, the values of maximum stresses to the plates with $H/L = 1.0$, defined from the NLS_{EP} , are found for higher values of degree of freedom H_0/L_0 when compared to the plates $H/L = 0.5$; fifth, the plates with $H/L = 0.5$ show higher loading capacity compared to the plates with $H/L = 1.0$; sixth, there is no universal perforation type that conducts to the best mechanical performance regarding the degree of freedom H_0/L_0 , instead there are intervals in which one perforation type has better results than the other types, e.g. in plates with $H/L = 0.5$ and for $\Phi = 0.20$, in the interval $0.44 < H_0/L_0 \leq 0.70$, the best perforation type is the rectangular, and; finally, the geometric shape of the perforation, i.e., the variation of its geometric configuration on the x and y -axes, is important for the development of the elasto-plastic buckling limit curves, causing an increase or decrease in the mechanical performance of the plates.$

In order to quantify the improvement in the mechanical behavior of the plates, Table 1 shows the results obtained comparing the best and the worst geometries for each specific type of perforation and for each value of Φ .

According to Table 1, the best mechanical performance for the plates with $H/L = 1.0$ corresponds to an increase of 191.85% for the plates with $\Phi = 0.10$ and transverse hexagonal perforation, while for the plates with $H/L = 0.5$ an improvement of 154.03% was achieved for the longitudinal oblong perforation type and $\Phi = 0.08$. In turn, the worst mechanical performance, of 42.82%, refers to the plates with $H/L = 1.0$, was obtained with $\Phi = 0.25$ and diamond perforation, as well as, of 36.54% for plates with $H/L = 0.5$, reached with $\Phi = 0.20$ and longitudinal oblong perforation.

Considering the mechanical performance for each studied perforation volume fraction Φ , it was observed:

Plates with $\Phi = 0.08$ for $H/L = 1.0$ and for $H/L = 0.5$ reached improvements of 185.41% for diamond perforation and 155.71% for rectangular perforation, respectively; while the worst obtained results were 132.97% and 107.50%, respectively, both for transversal oblong perforation.

Plates with $\Phi = 0.08$ for $H/L = 1.0$ and for $H/L = 0.5$ achieved improvements of 191.85% for transversal hexagonal perforation and 134.26% for elliptical perforation, respectively; while the worst results correspond, respectively, to 132.14% and 100.00% for plates with transversal oblong perforation.

Plates with $\Phi = 0.15$ for $H/L = 1.0$ and $H/L = 0.5$ presented improvements of 189.85% for rectangular perforation and 126.30% for elliptical perforation, respectively; and the worst results were 116.08% and 74.50%, respectively, for plates with transversal oblong perforation.

Plates with $\Phi = 0.20$ for $H/L = 1.0$ and $H/L = 0.5$ showed improvements of 176.44% for elliptical perforation and 130.88% for rectangular perforation, respectively; whereas the worst behaviors were 92.28% for transversal oblong perforation and 36.56% for rectangular perforation, respectively.

Plates with $\Phi = 0.20$ for $H/L = 1.0$ and $H/L = 0.5$ achieved improvements of 176.44% for elliptical perforation and of 130.88% for rectangular perforation, respectively; being the worst results of 92.28% for transversal oblong perforation and of 36.56% for longitudinal oblong perforation, respectively.

Plates with $\Phi = 0.25$ for $H/L = 1.0$ and $H/L = 0.5$ reached improvements of 186.31% for rectangular perforation and 137.25% for longitudinal oblong perforation, respectively;

whilst the worst results were of 42.86% and 86.67%, respectively, both for diamond perforation.

The application of the Constructal Design method allows an adequate comparison about the von Mises stress distribution among the studied plates. Thus, to illustrate how the principle of optimal distribution of imperfections actually leads to superior performances, the Figs. 12 and 13 show the distribution of von Mises stresses for the best and worst geometries, according to the data exposed in the Table 1, for $H/L = 1.0$ with $\Phi = 0.10$ and for $H/L = 0.5$ with $\Phi = 0.20$, respectively.

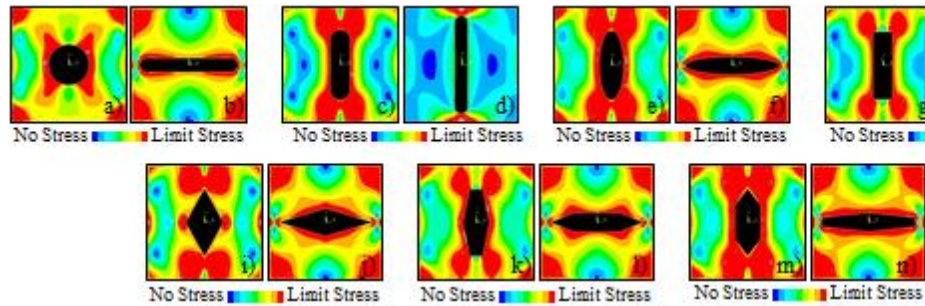


Fig. 12 Distribution of the von Mises stress in plates with $H/L = 1.0$, for all perforation types, and $\Phi = 0.10$, being: (a, c, e, g, i, m), the best; and (b, d, f, h, j, l, n), the worst configurations

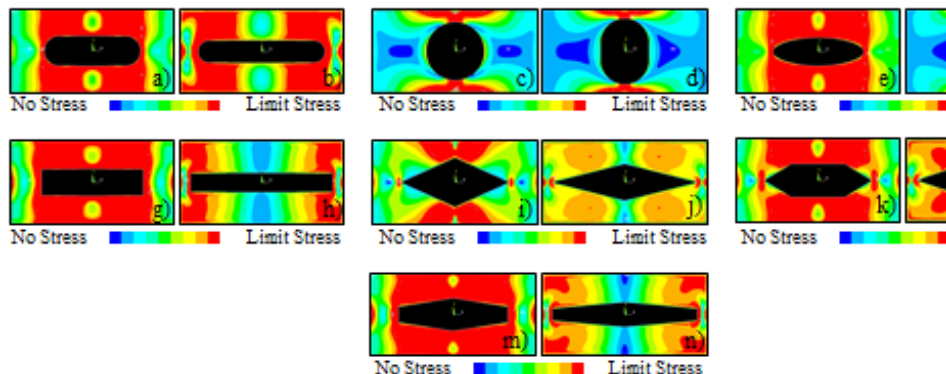


Fig. 13 Distribution of the von Mises stress in plates with $H/L = 0.5$, for all perforation types, and $\Phi = 0.20$, being: (a, c, e, g, i, k, m), the best; and (b, d, f, h, j, l, n), the worst configurations

The Figs. 12 and 13 show that the plates with the optimized geometries have the best distribution of the material yielding stress at failure when compared with the plates with the worst geometries. Visually, this means that the optimal geometries have a larger region subjected to the limit stress (which is represented by the red color). In this context, the improvement in mechanical performance obtained in the optimized geometries is in accordance with the principles defined by the Constructal Theory, that is, this geometry promotes the better distribution of the imperfections [18].

Table 1: Best and worst geometries for all cases studied

Hole type	H/L = 1.0					H/L = 0.5					
	$\left(\frac{H_0}{L_0}\right)_o$	NLS _{Max}	$\frac{H_0}{L_0}$	NLS _{Min}	Diff. %	$\left(\frac{H_0}{L_0}\right)_o$	NLS _{Max}	$\frac{H_0}{L_0}$	NLS _{Min}	Diff. %	
$\phi = 0.08$	LO	0.99	0.2890	0.12	0.1227	135.53	0.10	0.4636	0.05	0.1825	154.03
	TO	4.00	0.3215	8.99	0.1380	132.97	1.01	0.4150	3.77	0.2000	107.50
	E	3.50	0.3271	0.14	0.1165	180.77	0.25	0.4515	3.10	0.2050	120.24
	R	4.00	0.3165	0.12	0.1253	152.59	0.10	0.4636	0.05	0.1813	155.71
	D	2.30	0.3325	0.22	0.1165	185.41	0.30	0.4440	0.10	0.1972	125.15
	LH	3.50	0.3205	0.15	0.1227	161.21	0.20	0.4581	3.00	0.2000	129.05
	TH	3.50	0.3330	0.15	0.1190	179.83	0.20	0.4555	0.07	0.2036	123.72
$\phi = 0.10$	LO	0.99	0.2840	0.14	0.1115	154.71	0.20	0.4496	0.07	0.2236	101.07
	TO	3.50	0.3250	7.15	0.1400	132.14	1.01	0.4000	2.96	0.2000	100.00
	E	2.80	0.3340	0.18	0.1178	183.53	0.20	0.4465	0.08	0.1906	134.26
	R	3.50	0.3130	0.14	0.1115	180.72	0.20	0.4495	3.20	0.1950	130.51
	D	1.80	0.3240	0.28	0.1177	175.28	0.30	0.4245	1.60	0.2096	102.53
	LH	2.50	0.3255	0.19	0.1203	170.57	0.20	0.4476	2.40	0.2000	123.80
	TH	2.70	0.3400	0.19	0.1165	191.85	0.30	0.4405	2.40	0.2090	110.77
$\phi = 0.15$	LO	0.99	0.2730	0.22	0.1075	153.95	0.20	0.4186	0.10	0.1889	121.60
	TO	1.80	0.3090	4.68	0.1430	116.08	1.05	0.3490	1.89	0.2000	74.50
	E	1.80	0.3040	0.26	0.1050	189.52	0.30	0.4130	0.12	0.1825	126.30
	R	2.00	0.2971	0.21	0.1025	189.85	0.20	0.4155	0.10	0.1906	118.00
	D	1.50	0.2500	0.41	0.1025	143.90	0.35	0.3695	0.19	0.1972	87.37
	LH	1.50	0.3095	0.28	0.1075	187.91	0.20	0.4096	1.60	0.1986	106.24
	TH	1.50	0.2950	0.28	0.1075	174.42	0.30	0.4096	0.13	0.1863	119.86
$\phi = 0.20$	LO	0.99	0.2440	0.29	0.0950	156.84	0.30	0.3830	0.17	0.2805	36.54
	TO	1.60	0.2740	3.45	0.1425	92.28	1.01	0.2800	1.34	0.1980	41.41
	E	1.30	0.2640	0.35	0.0955	176.44	0.30	0.3786	1.25	0.2000	89.30
	R	1.40	0.2740	0.30	0.1025	167.32	0.25	0.3895	0.13	0.1687	130.88
	D	1.30	0.1840	0.55	0.0890	106.74	0.45	0.3150	0.25	0.1725	82.61
	LH	1.20	0.2600	0.37	0.1000	160.00	0.30	0.3665	0.17	0.1813	102.15
	TH	1.50	0.2490	0.37	0.0955	160.73	0.30	0.3756	0.17	0.1687	122.64
$\phi = 0.25$	LO	0.99	0.1955	0.37	0.0890	119.66	0.30	0.3535	0.16	0.1490	137.25
	TO	1.20	0.2240	2.71	0.1380	62.32	-	-	-	-	-
	E	1.20	0.2130	0.44	0.0915	132.79	0.40	0.3365	0.20	0.1640	105.18
	R	1.20	0.2405	0.34	0.0840	186.31	0.30	0.3586	0.16	0.1555	130.61
	D	1.01	0.1200	0.68	0.0840	42.86	0.50	0.2800	0.31	0.1500	86.67
	LH	1.40	0.2050	0.46	0.0890	130.34	0.47	0.3300	0.21	0.1650	100.00
	TH	1.40	0.1950	0.46	0.0890	119.10	0.40	0.3326	0.21	0.1573	111.44

7. Conclusions

Computational models associated to the Constructal Design were used to analyze the influence of the geometric configuration of perforations on thin steel plates subjected to elasto-plastic buckling. It was possible, through these analyses, to obtain the values of the ultimate stresses in the elasto-plastic buckling. To do so, the type (longitudinal oblong, transverse oblong, elliptic, rectangular, diamond, longitudinal hexagonal, and transverse hexagonal), shape (by means the variation of H_0/L_0 ratio) and size (through of volume fraction Φ variation) of perforations were evaluated.

The H_0/L_0 variation allows the definition of elasto-plastic buckling limit curve for all studied type and size of perforations. These curves represent the collapse of the plates by yielding of the material and indicate the effect of shape perforation in each case, being this a scientific contribution of the present work.

The obtained results show a variation in the mechanical performance improvement from 42.86% to 191.85% for the plates with $H/L = 1.0$, and from 36.54% to 155.71% for the plates with $H/L = 0.5$.

According to the type of perforation, the best mechanical performances obtained for the plates with $H/L = 1.0$ were: 156.8% for longitudinal oblong perforation plates and $\Phi = 0.20$; 132.9% for the plates with transversal oblong perforation and $\Phi = 0.08$; 189.5% for plates with elliptical perforation and $\Phi = 0.15$; 189.8% for plates with rectangular perforation and $\Phi = 0.15$; 185.4% for plates with diamond perforation and $\Phi = 0.08$; 187.9% for the plates with longitudinal hexagonal perforation and $\Phi = 0.15$; 191.8% for the plates with transverse hexagonal perforation and $\Phi = 0.10$. For the plates with $H/L = 0.5$, there were: 154.0% for the plates with longitudinal oblong perforation and $\Phi = 0.08$; 107.5% for plates with transverse oblong perforation and $\Phi = 0.08$; 134.2% for plates with elliptical perforation and $\Phi = 0.10$; 155.7% for plates with rectangular perforation and $\Phi = 0.08$; 125.1% for plates with diamond perforation and $\Phi = 0.08$; 129.0% for the plates with longitudinal hexagonal perforation and $\Phi = 0.08$; 123.7% for the plates with transverse hexagonal perforation and $\Phi = 0.08$. Hence, the plates with $H/L = 1.0$ presented a higher mechanical performance than the plates with $H/L = 0.5$, considering all types of perforation, for $\Phi = 0.10$, $\Phi = 0.15$, and $\Phi = 0.20$. The exceptions refer to plates with oblong longitudinal and rectangular perforations, for $\Phi = 0.08$; and with oblong longitudinal and diamond perforation for $\Phi = 0.25$.

Lastly, the use of the Constructal Design method associated with computational modeling allowed to show the importance that the geometric evaluation has for the definition of the mechanical behavior of the plates in elasto-plastic buckling. Its application made it possible to compare adequately the results obtained for all types and geometric forms of the proposed perforations. It was possible to evaluate the influence of the type, shape, and size of the perforation on the mechanical behavior of the plates as a function of H/L and H_0/L_0 . In this sense, the Constructal Design method was used to define, through the analysis of the imperfection distribution, the optimal geometry for each H/L ratio, for each volume fraction (Φ) of the perforation, and for each type of perforation. It was verified that the optimal geometry, i.e., the geometry that promotes the maximization of the ultimate buckling stress, is in agreement with the statement: "The structures that present the best mechanical performance also present the best distribution of their imperfections, which is in accordance with the principles defined in the Constructal theory [18, 28].

8. Acknowledgments

The authors thank FAPERGS (Research Support Foundation of Rio Grande do Sul), CNPq (Brazilian National Council for Scientific and Technological Development) and CAPES Brazilian Coordination for Improvement of Higher Education Personnel) for the financial support.

Nomenclature

D	Diamond perforation	E_t	steel tangent modulus of elasticity
E	Elliptical perforation	H	plate width
EP	Elasto-Plastic buckling	h, t	plate thickness
FEM	Finite Element Method	H/L	relation between the width and the length of the plate
LH	Longitudinal Hexagonal perforation	h_0	perforation width
LO	Longitudinal Oblong perforation	h_0/L_0	relation between perforation width and length
NLS	Normalized Limit Stress	k	function of the aspect ratio
R	Rectangular perforation	L	plate length
TH	Transversal Hexagonal perforation	l_0	perforation length
TO	Transversal Oblong perforation	m	number of half-waves of the deformation pattern in the x -axis direction
$\left(\frac{H_0}{L_0}\right)_o$	best geometry	NLS_{Max}	maximum normalized limit stresses
$\{F_{NL}\}_o$	vector of internal nonlinear nodal forces	NLS_{min}	minimum normalized limit stress
$[K_t]$	updated tangent stiffness matrix	P_{cr}	critical load per unit of length
$\{P\}_i$	external load applied	P_u	ultimate load per unit of lenght
$\{P\}_{i+1}$	external load applied	V	total volume of the plate without perforation
$\{U\}_i$	displacement	V_0	perforation volume
$\{U\}_{i+1}$	displacement	ν	poisson's ratio of the plate's material
$\{\Delta U\}$	vector of incremental displacements	π	mathematical constant
$\sqrt{\tau}$	plastic reduction factor of a plate subjected to uniform compression stress in one direction	σ_{cr}	critical stress
$\{\psi\}$	vector of unbalanced forces	σ_u	ultimate stress
D	plate bending stiffness	σ_y	material yielding strength
E	modulus of elasticity	ϕ	fraction for the perforation volume

References

- [1] Bellei IH. Edifícios Industriais em Aço: Projeto e Cálculo, Pini, São Paulo, SP, Brazil, 2006.
- [2] Silva VP. Design of Steel Structures, Course notes - USP, São Paulo, SP, Brazil, 2012.

- [3] Ventsel E, Krauthammer T. *Thin Plates and Shells*, Marcelo Dekker, New York, NY, USA, 2001.
- [4] Okumoto Y, Takeda Y, Mano M, Okada T. Design of Ship Hull Structures: A practical Guide for Engineers, Springer, Yokohama, Japan, 2009. <https://doi.org/10.1007/978-3-540-88445-3>
- [5] Cheng B, Zhao JS. Strengthening of perforated plates under uniaxial compression: Buckling analysis. *Thin-Walled Structures*, 2010; 48(12): 905-914. <https://doi.org/10.1016/j.tws.2010.06.001>
- [6] Chow F, Narayanan R. Buckling of Plates Containing Openings, Seventh International Specialty Conference on Cold-Formed Steel Structures, 1984
- [7] El-Sawy KM, Martini MI. Elastic stability of bi-axially loaded rectangular plates with a single circular hole, *Thin-Walled Structures*, 2007; 45(1): 122-133. <https://doi.org/10.1016/j.tws.2006.11.002>
- [8] Moen CD, Schafer BW. Elastic buckling of thin plates with holes in compression or bending, *Thin-Walled Structures*, 2009; 47(12): 1597-1607. <https://doi.org/10.1016/j.tws.2009.05.001>
- [9] Helbig D, Real MV, Correia ALG, Dos Santos ED, Rocha LAO., Isoldi LA. Constructal Design of perforated steel plates subject to linear elastic and nonlinear elasto-plastic buckling. XXXIV Iberian Latin American Congress on Computational Methods in Engineering, 2013.
- [10] Lorenzini G, Helbig D, Da Silva CCC, Real MV, Dos Santos ED, Isoldi LA. Constructal design method applied to the analysis of the cutout type and cutout shape influences in the mechanical behavior of thin steel plates subjected to buckling, Constructal Law & Second Law Conference, 2015
- [11] Falkowicz K, Ferdynus M, Debski H. Numerical analysis of compressed plates with a cut-out operating in the geometrically nonlinear range, *Science and Technology*, 2015; 17(2): 222-227. <https://doi.org/10.17531/ein.2015.2.8>
- [12] Åkesson B. *Plate Buckling in Bridges and other Structures*, Taylor & Francis Group, London, England, 2007.
- [13] Vinson JR. *Plate and Panel Structures of Isotropic, Composite and Piezoelectric Materials, Including Sandwich Construction*, Springer Science & Business Media, 2005. <https://doi.org/10.1007/1-4020-3111-4>
- [14] Chajes A. *Principles of Structural Theory*, Prentice-Hall, Englewood Cliffs, NJ, USA, 1974.
- [15] Bradford MA, Cuk PE. Elastic buckling of tapered monosymmetric I-beams, *Journal of Structural Engineering*, 1988; 114(5): 977-996. [https://doi.org/10.1061/\(ASCE\)0733-9445\(1988\)114:5\(977\)](https://doi.org/10.1061/(ASCE)0733-9445(1988)114:5(977))
- [16] Mulligan GP, Peköz T. The influence of local buckling on the structural behavior of single-symmetric cold-formed steel columns, Center for Cold-Formed Steel Structures Library, 1983.
- [17] Yu, Wei-Wen. *Cold-formed steel design*. John Wiley & Sons, 2000.
- [18] Bejan A, Lorente S. *Design with Constructal Theory*, John Wiley & Sons, Inc, Hoboken, NJ, USA, 2008. <https://doi.org/10.1002/9780470432709>
- [19] Bejan A, Lorente S. Constructal law of design and evolution: Physics, biology, technology, and society, *Journal of Applied Physics*, 2013; 113(15): 6. <https://doi.org/10.1063/1.4798429>
- [20] Bejan A, Evolution in thermodynamics, *Applied Physics Reviews*, 2017; 4(1): 011305. <https://doi.org/10.1063/1.4978611>
- [21] Miguel A F. Toward a quantitative unifying theory of natural design of flow systems: emergence and evolution. In: *Constructal Law and the Unifying Principle of Design*, Springer, New York, NY, USA, 2013: 21-39. https://doi.org/10.1007/978-1-4614-5049-8_2
- [22] Lorenzini G, Biserni C, Estrada E, Isoldi LA, Dos Santos ED, Rocha LAO. Constructal design of convective Y-shaped cavities by means of genetic algorithm, *Journal of Heat Transfer*, 2014; 136(7): 071702. <https://doi.org/10.1115/1.4027195>
- [23] Gonzales GV, Estrada ESD, Emmendorfer LR, Isoldi LA, Xie G, Rocha LAO, et al. A comparison of simulated annealing schedules for constructal design of complex cavities intruded into conductive walls with internal heat generation, *Energy*, 2015; 93: 372-382. <https://doi.org/10.1016/j.energy.2015.09.058>
- [24] Ansys, User's manual (version 10.0), 2005.

- [25] Madenci E, Guven I. The Finite Element Method and Applications in Engineering Using Ansys, Springer, New York, NY, USA, 2006.
- [26] El-Sawy KM, Nazmy AS, Martini MI. Elasto-plastic buckling of perforated plates under uniaxial compression, *Thin-Walled Structures*, 2004; 42(8): 1083-1101. <https://doi.org/10.1016/j.tws.2004.03.002>
- [27] Helbig D, Silva CCCD, Real MDV, Santos EDD, Isoldi LA, Rocha LAO. (2016). Study About Buckling Phenomenon in Perforated Thin Steel Plates Employing Computational Modeling and Constructal Design Method. *Latin American Journal of Solids and Structures*, 2016; 13(10); 1912-1936. <https://doi.org/10.1590/1679-78252893>
- [28] Bejan A, Zane J P. Design in nature. *Mechanical Engineering*, 2012; 134(6); 42.



Research Article

Darrieus vertical axis wind turbines: methodology to study the self-start capabilities considering symmetric and asymmetric airfoils

Nelson C. Batista^{1,2}, Rui Melicio^{*,1,2,3}, Victor M.F. Mendes^{1,4,5}

¹ Departmento de Física, Escola de Ciências e Tecnologia, Universidade de Évora, Portugal

² IDMEC, Instituto Superior Técnico, Universidade de Lisboa, Lisbon, Portugal

³ ICT, Universidade de Évora, Portugal

⁴ Department of Electrical Engineering and Automation, Instituto Superior de Engenharia de Lisboa, Portugal

⁵ CISE, Electromechatronic Systems Research Centre, Universidade da Beira Interior, Portugal

Article Info

Article history:

Received 01 Jan 2018

Revised 25 Feb 2018

Accepted 26 Mar 2018

Keywords:

*Self-starting,
Blade profile,
Symmetric airfoil,
Asymmetric airfoil,
Vertical axis wind
turbines*

Abstract

The rapid growth of wind power generation and the need for a smarter grid with decentralized energy generation has increased the interest in vertical axis wind turbines (VAWT), especially for the urban areas. For the urban areas the VAWT offer several advantages over the horizontal ones, so their acceptance is rising. The lift-type VAWT (Darrieus wind turbines) have a natural inability to self-start without the help of extra components. The existing methodologies are usually used to optimize the wind turbine performance, but not its ability to self-start. Indeed, studying the aerodynamic behavior of blade profiles is a very complex and time-consuming task, since blades move around the rotor axis in a three-dimensional aerodynamic environment. Hence, a new methodology is presented in this paper to study the self-start ability of VAWT, which offers a substantial time reduction in the first steps of new blade profiles development. Both symmetrical and asymmetrical airfoils are targeted in our study, presenting comprehensive results to validate our methodology.

© 2018 MIM Research Group. All rights reserved

Introduction

The renewable energies share in power production has increased significantly in many European countries [1-6]. The wind energy systems have been considered as one of the most cost effective of all the currently exploited renewable energy sources, so a growing investment in wind energy systems has occurred in the last decade.

The decentralized energy generation is an important solution in a smarter grid with a growing acceptance for the urban areas. Also, the increasing need for more environmentally sustainable housing and the new European norms regulating this issue, have contributed for the promotion of wind energy systems in buildings.

In urban areas the wind is very turbulent and unstable with fast changes in direction and velocity.

*Corresponding author: rui.melicio@gmail.com

DOI: <http://dx.doi.org/10.17515/jresm2017.39ds0108>

In these environments the vertical axis wind turbines (VAWT) have several advantages over horizontal axis wind turbines (HAWT) [7]: insensitivity to yaw wind direction changes (so the turbine does not need the extra components to turn the rotor against the wind); smaller number of components (the reduced number of components leads to a more reliable product and a reduced cost in production and maintenance); very low sound emissions (ideal for urban areas); ability to generate energy from wind in skewed flows (skewed flows are very usual in urban areas, especially in the rooftop of buildings); three dimensional structural design, easier to integrate in urban architecture; ability to operate closer to the ground level.

The modern VAWT can be divided in three basic types: Savonius [8-9], Darrieus [10-11] and H-rotor [12]. The Savonius VAWT is a drag-type wind turbine. This type of wind turbine has the ability to self-start and has high torque, but it operates at low tip speed ratio (TSR). The Darrieus VAWT is a lift-type wind turbine. Darrieus VAWT can be divided in two kinds: curved bladed turbine (or egg-shaped turbine) and straight bladed turbine. The H-rotor is the most common configuration of the straight bladed Darrieus VAWT. The "H" rotor received its name due to the arms and straight blade configuration resembling the "H" letter. Lift-type wind turbines can operate at high TSR, but they usually have an inherent problem: the inability to self-start [13]. On one hand, if VAWT need to be self-starting capable their performance is compromised, not being able to work at high TSR. On the other hand, if VAWT need to exhibit superior performance at high TSR they are not able to self-start without extra components or external power.

This paper is based on straight bladed Darrieus VAWT and the main goal is to present a new methodology to study their self-start behavior, capable of offering a fast tool for developing blade profiles. In this methodology, a relationship between the wind turbine (when it's in a stopped position), its blade profile design, and the aerodynamic behavior of the wind flow, is determined. Several symmetrical and asymmetrical airfoils are tested and their output data analyzed in order to demonstrate the proficiency of the new methodology.

This paper is organized as follows. Section 2 presents the performance prediction and modeling of the straight bladed Darrieus VAWT. Section 3 addresses the Darrieus VAWT ability to self-start. Section 4 provides the new methodology to study self-start capabilities. Section 5 presents the results considering several symmetrical and asymmetrical NACA airfoils. Finally, Section 6 outlines the conclusions.

2. Darrieus VAWT Performance Prediction and Modeling

The VAWT aerodynamic modeling is very complex since the turbine blades travel around the rotor in a 360° rotation. While some of the blades have lift forces acting on them, others suffer from drag forces in an opposing movement to the rotor rotation. Additionally, the blades that are traveling in the upstream side of the turbine induce some turbulence that will affect the blades performance travelling in the downstream side. These and other issues make VAWT performance prediction a very hard task, far more complex than for HAWT.

Several VAWT performance prediction models [13] have been developed, which will be briefly described in this section. The flow velocities diagram of a lift-type VAWT is shown in Fig. 1.

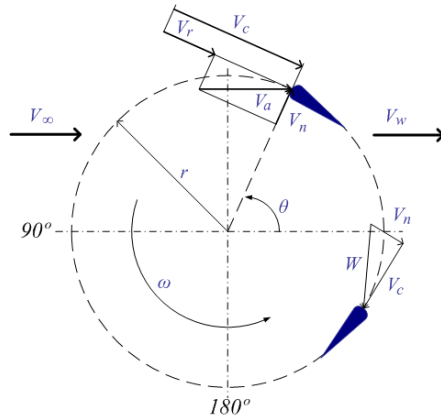


Fig. 1 Flow velocities diagram of a lift-type VAWT

In Fig. 1 shows the undisturbed wind velocity V_∞ that reaches the wind turbine, the induced velocity V_a at the blade profile level, and the induced velocity due to the rotor angular speed at the wind turbine V_r , i.e., due to the blade in its movement around the rotor, given by:

$$V_r = \omega r \quad (1)$$

The blade is influenced by the contribution of V_a and V_r to a resulting chordal velocity V_c , i.e., the velocity parallel to the chord line of the blade profile, given by:

$$V_c = V_r + V_a \cos\theta = r\omega + V_a \cos\theta = \lambda V_a + V_a \cos\theta \quad (2)$$

The induced velocity V_a has also a contribution to the normal velocity V_n , i.e., the velocity in a radial direction in relation to the center of the rotor, given by:

$$V_n = V_a \sin\theta \quad (3)$$

The relative flow velocity W is given by:

$$W = \sqrt{V_c^2 + V_n^2} = V_a \sqrt{1 + 2\lambda \cos\theta + \lambda^2} \quad (4)$$

The blade angle of attack α is given by:

$$\alpha = \tan^{-1} \left(\frac{V_n}{V_c} \right) = \tan^{-1} \left(\frac{V_a \sin\theta}{r\omega + V_a \cos\theta} \right) = \tan^{-1} \left(\frac{\sin\theta}{r\omega/V_a + \cos\theta} \right) \quad (5)$$

If the blade turbine is able to modify its pitch angle γ , the blade angle of attack α will be given by:

$$\alpha = \tan^{-1} \left(\frac{\sin \theta}{r\omega/V_a + \cos \theta} \right) - \gamma \quad (6)$$

The forces diagram acting on the blade airfoil is shown in Fig. 2.

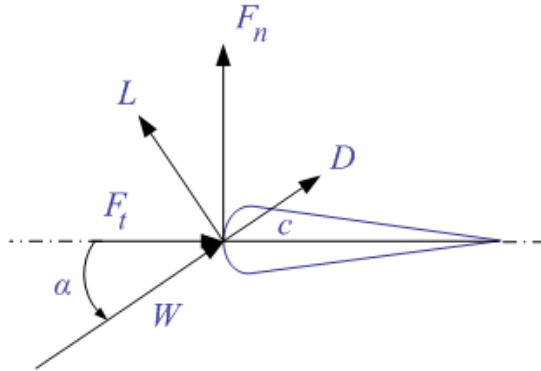


Fig. 2 Forces diagram acting on the blade airfoil

The tangential force coefficient C_t and the normal coefficient C_n are given by:

$$C_t = C_l \sin \alpha - C_d \cos \alpha \quad (7)$$

$$C_n = C_l \cos \alpha + C_d \sin \alpha \quad (8)$$

The tangential force F_t and normal force F_n are given by:

$$F_t = \frac{1}{2} C_t \rho c h W^2 \quad (9)$$

$$F_n = \frac{1}{2} C_n \rho c h W^2 \quad (10)$$

The average tangential force F_{ta} in function of the tangential force F_t around the rotor and the azimuth angle θ is given by:

$$F_{ta} = \frac{1}{2\pi} \int_0^{2\pi} F_t(\theta) d\theta \quad (11)$$

The turbine overall torque Q is given by:

$$Q = n F_{ta} r \quad (12)$$

The turbine overall power P is given by:

$$P = Q \omega \quad (13)$$

The power coefficient C_P is the relation between the wind turbine power output and the power available in the wind, given by:

$$C_P = \frac{P}{1/2 \rho V_\infty^3 A} = \frac{n F_{ta} r \omega}{1/2 \rho V_\infty^3 h r^2} = 2 \frac{n F_{ta} \omega}{\rho V_\infty^3 h r} \quad (14)$$

Several mathematical models have been developed by different researchers to achieve a more accurate prediction of lift-type VAWT performance. The most common used models can be divided in three categories: blade element momentum (BEM) model, vortex model and cascade model [13].

2.1. BEM Model

BEM theory is a combination of blade element theory with basic momentum theory, studying the flow and behavior of the air on the blades and the involved forces. The base models on the BEM theory experience some problems when trying to predict the performance for high TSR and high solidity σ turbines. Based on BEM theory, several models have been developed: single streamtube model, multiple streamtube model and double-multiple streamtube model.

2.1.1 Single Streamtube Model

This is the simplest model and is represented by a single streamtube where the turbine is placed and its blades in their revolution are translated in an actuator disc. All the blades are translated in only one blade where its chord is the sum of all turbine blades chords. The wind speed in the upstream and downstream sides of the rotor is assumed to be constant. The effects of the wind speed outside the streamtube are assumed negligible. The single streamtube model is illustrated in Fig. 3.

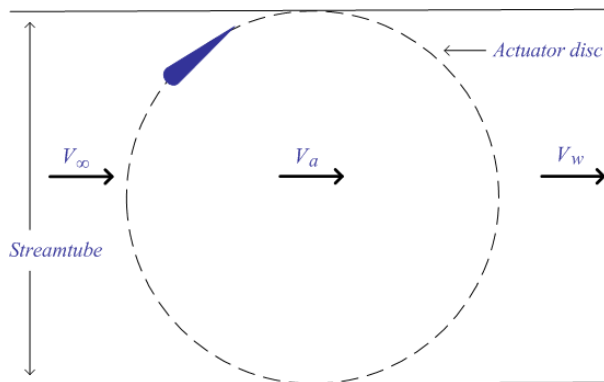


Fig. 3 Single streamtube model diagram

The uniform velocity through the rotor is given by:

$$V_a = \frac{V_\infty + V_w}{2} \quad (15)$$

The turbine drag force F_D considering the rate of change of momentum, is given by:

$$F_D = A\rho V_a (V_\infty - V_w) \quad (16)$$

The turbine drag coefficient C_D is given by:

$$C_D = \frac{F_D}{1/2 \rho A V_a^2} = \frac{A\rho V_a (V_\infty - V_w)}{1/2 \rho A V_a^2} = \frac{V_\infty - V_w}{1/2 V_a} \quad (17)$$

Considering (15), C_D is given by:

$$C_D = \frac{V_\infty - (2V_a - V_\infty)}{1/2 V_a} = \frac{4(V_\infty - V_a)}{V_a} \quad (18)$$

The induced velocity ratio is given by:

$$\frac{V_a}{V_\infty} = \frac{1}{1 + C_D/4} \quad (19)$$

By using (19), and with the general mathematical expressions that were presented before, it is now possible to predict the torque and power coefficient of the VAWT. However, the single streamtube model is not good in predicting the turbine performance, since it neglects the wind speed variations inside and outside the rotor, usually providing much higher values than those obtained from experimental data.

2.1.2 Multiple Streamtube Model

This model is a variation of the single streamtube model, where instead of having only one streamtube there are several parallel and adjacent streamtubes independent from each other, having their own undisturbed, induced and wake velocities. The multiple streamtube model is shown in Fig. 4.

The induced velocity ration equation for this model is given by:

$$\frac{V_a}{V_\infty} = 1 - \left(\frac{k}{2} \frac{nc}{r} \frac{r\omega}{V_\infty} \sin\theta \right) \quad (20)$$

Several multiple streamtube models have been presented over the years, with the addition of drag forces, blade profile geometry, turbine solidity, curvature flow, and so on. However, the performance prediction is still far from experimental values.

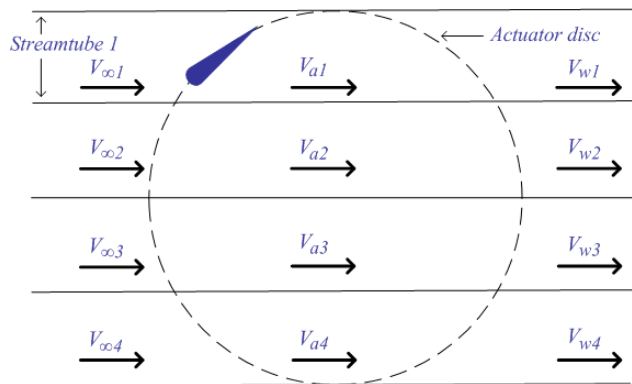


Fig. 4 Multiple streamtube model diagram

2.1.3 Double-Multiple Streamtube Model

The double-multiple streamtube model [14-16] is a variation of the multiple streamtube model, in which the actuator disc is divided into half cycles representing the upstream and the downstream of the rotor, as shown in Fig. 5.

The actuator disc is then divided in two actuator discs, each of them with their own induced velocity. The induced velocity in the upstream is represented by V_{au} and the induced velocity in the downstream is represented by V_{ad} .

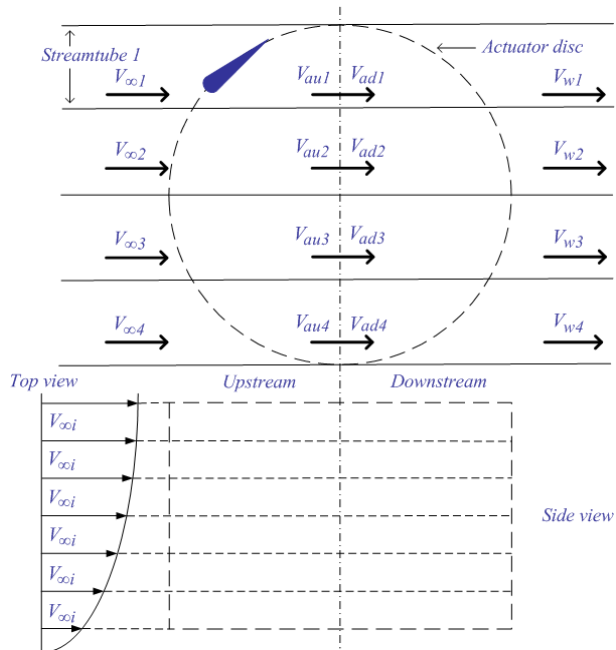


Fig. 5 Double-multiple streamtube model diagram

The induced velocity in the downstream is influenced by the wake velocity in the upstream V_e , which is given by:

$$V_e = V_{\infty i} \left(2 \frac{V_{au}}{V_{\infty i}} - 1 \right) = V_{\infty i} (2u_u - 1) \quad (21)$$

The induced velocity in the downstream V_{ad} is given by:

$$V_{ad} = u_d V_e = u_d (2u_u - 1) V_{\infty i} \quad (22)$$

The interference factor for the downstream, which is given by:

$$u_d = \frac{V_{ad}}{V_e} \quad (23)$$

This model has received some improvements over the years and provides a good performance for most predictions, but it may suffer convergence problems in some cases.

2.2. Vortex Model

The vortex model [17-18] predicts the performance of VAWT by calculating the vorticity in the wake of the blades. The blades are substituted by vortex filaments whose strengths will be determined by the blade profile coefficients, relative flow velocity and angle of attack. By Helmholtz theorems of vorticity, the strengths of the vortex filaments are equal to each trailing tip vortex.

Several modifications on this model have been presented, but the main disadvantage of the vortex model still persists, the high computation time.

2.3. Cascade Model

In the cascade model [19] the VAWT blades are arranged in vanes called cascade and positioned in equal interspaces of the turbine perimeter divided by the number of blades. The aerodynamic properties of the blades are calculated independently taking in consideration the upwind and downwind sides of the rotor, their local Reynolds number and the local angle of attack.

This model does not have convergence problems and provides good performance prediction in low and high TSR. However, like the vortex model, the cascade model requires a high computation time.

2.4. Aerodynamic Disturbances

Although there are several mathematical models for the VAWT performance prediction, still the aerodynamic behavior of the VAWT rotor is very difficult to predict. Several aerodynamic disturbances can be found in the VAWT operation, such as deep stall, dynamic stall and laminar separation bubbles.

References [20-22] model the dynamic stall on VAWT, validating the results with particle image velocimetry data. In the rooftops the wind flows in a skewed movement. Reference [23] addresses the feasibility analysis of a Darrieus VAWT installation in the rooftop of a building. Also, a computational study of a rooftop size VSWT with straight blades is presented in [24]. Some solutions have been presented for preventing vortex shedding and reducing drag in flows past bluff bodies. Large vortices forming in high-speed flows past bluff bodies tend to be shed downstream, with new vortices forming in their stead. These issues result in an increased drag, unsteady loads on the body, and produce an unsteady

wake. Reference [25] presents a trapped vortex cell solution that keeps the vortex near the body at all times, reducing those effects.

3. Solutions to Overcome the Natural Self-Start Inability of Darrieus VAWT

The Darrieus VAWT has a natural inability to self-start, since the blades suffer at the same time with the drag forces and the lift forces. These forces usually balance each other leading to a lack of starting torque. Nevertheless, there are few works that study the starting performance of Darrieus VAWT through the development and validation of computational simulation, as occurs in [26].

Several solutions have been presented to overcome the self-start inability of Darrieus wind turbines, such as external electricity feed-in, guide-vanes, hybrid configuration, blade pitch optimization, blade form optimization, and blade profile design.

3.1. External Electricity Feed-In

The use of a generator with external electricity feed-in helps the rotor to start rotating. This is commonly used in the egg shaped Darrieus VAWT. A problem arises here when the wind turbines are disconnected from the grid and do not have an external electricity source.

3.2. Guide-Vanes

The use of a guide-vane [27] may prevent the drag effect on the blades moving in the upwind zone of the wind turbine, optimizing the wind flow in the downwind zone to maximize the lift forces on the blades. The guide-vanes increase the turbine solidity, leading to higher forces to be exerted in the pole. However, the use of guide-vanes implies that more material and components are required, increasing the VAWT price and reducing its sustainability.

3.3. Hybrid Configuration

A Savonius VAWT has been used in a hybrid configuration with a Darrieus VAWT [28-29]. This hybrid configuration gives the wind turbine the self-start capabilities (offered by the Savonius VAWT) and the ability to operate at TSR higher than one (offered by the Darrieus VAWT). However, at high TSR the Savonius VAWT increases the drag leading to a lower performance, which would not occur if only a Darrieus VAWT was used.

3.4. Blade Pitch Optimization

Reference [30] addresses the VAWT blade pitch optimization. The mechanical systems used to optimize the blade pitch angle are usually complex and, since they need to operate at high speeds when the turbine reaches high TSR, the components experience fatigue. The increase of turbine complexity and components number leads to higher production and maintenance costs. Also, the components fatigue reduces the lifetime of the turbine. Some tools are presented in [15] to define the optimal variation of the blade pitch angle in straight bladed Darrieus VAWT.

3.5. Blade Form Optimization

The optimization of the blade form may increase the drag properties at low TSR and increase the lift properties at high TSR [31]. These systems have similar problems to the blade pitch systems presented earlier, leading to a complexity increase and higher production and maintenance costs.

3.6. Blade Profile Design

A blade profile capable of offering self-start capabilities to the wind turbine is desirable [26]. By studying and developing new profiles for the VAWT blades, a self-start improvement of the wind turbine may be achieved. However, this is a very time consuming task that usually requires a significant computation time to study profile variations. Some of the modifications that can be made to the blade profile to enhance the self-starting behavior of VAWT are: high turbine solidity; blades with inclined leading edge; cambered blades [32-33]; thick blades [34]. However, as the VAWT self-starting behavior is enhanced, a compromise to the wind turbine performance at high TSR should be made.

3.7. Motivation for a New Methodology

This paper envisages the development of new blade profiles to overcome the natural inability of the VAWT to self-start, without compromising much of the performance at high TSR. Several models have been developed to predict the Darrieus VAWT performance when its blades are moving, but no model addresses the study of the turbine ability to self-start relying only on the blades form. Hence, the new methodology presented in this paper offers a fast-computational tool for the development of new blade profiles for Darrieus VAWT, capable of being integrated with existing tools or capable of being used as a standalone tool. The new methodology is presented hereafter.

4. New Methodology to Study Self-Start Capabilities

4.1. The Problem to Solve

To study the self-start capabilities of a VAWT blade profile, there is the need to create a methodology that would give a closer relation between the wind forces acting on the blade, and the blade profile itself. Also, the methodology should be fast in computation time, useful in the first steps of the studies when developing different profile designs.

A wind turbine is able to self-start when without external help (extra components or external energy) it accelerates from a stopped position to a certain rotation movement able to produce energy. The new methodology presented studies the exact moment when the wind turbine starts to move by itself.

The VAWT must take advantage of the drag forces caused by the wind on the blades when the turbine is in a stopped position in order to self-start relying only on the blades profile, without compromising the wind turbine performance at high TSR. If possible, the lift forces should be used in cooperation with the drag forces to induce the self-start capability of the wind turbine, especially when the turbine is stopped and the wind flow starts to achieve higher velocities.

Since the blade may be at any given position around the rotor, there is the need to study the blade profile at any angular position from 0° to 360° . Accordingly, the dynamic stall behavior, air flow separation and any other aerodynamic disturbances must be taken in account [20-22]. To study these aerodynamic disturbances requires a significant computation time, which leads to considerable time consumption not advisable in the first steps of development studies. So, the new methodology that is present here is mainly suitable for a fast analysis, when there is the need to compare several blade profile solutions to start restricting and eliminating different designs. It is also important not to forget the analysis of different aspects of the wind flow disturbances acting on the wind turbine.

4.2. Description of the Methodology

To study the blade profile modifications and the implications that those modifications bring to the wind turbine performance, a close relation between the surface of the blade and the wind flow must be created. In this methodology the pressure coefficient C_{pr} is used, which is a dimensionless number that describes the relative pressure throughout a flow field. It is intimately correlated to the flow velocity, and can be calculated at any point of the flow field.

The C_{pr} is useful to study the forces acting on any given point on the blade profile surface and its relation with dimensional numbers [35] is given by:

$$C_{pr} = \frac{p - p_\infty}{1/2 \rho V_\infty^2} \quad (24)$$

In a normal operation of a VAWT, the variations of pressure and wind speed have little influence in the wind density, so the wind flow can be treated as being incompressible. Hence, it is assumed that: when C_{pr} is equal to one, that point is a stagnation point, meaning that the flow velocity at that point is null (relevant when optimizing the drag forces); when C_{pr} is negative in the point of study, the wind is moving at a higher speed than in the undisturbed wind flow (relevant when optimizing the lift forces).

To study the C_{pr} around the blade profile surface, firstly there is the need to divide it into segments. The blade profile NACA0020 with surface divisions is shown in Fig. 6. Smaller segments can provide a more accurate analysis.

The pressure coefficient acting on the blade profile divided surface is shown in Fig. 7. This figure illustrates the points i and $i + 1$ of the segment of length s in the blade profile surface, their corresponding Cartesian coordinates and the C_{pr} acting on the blade profile surface.

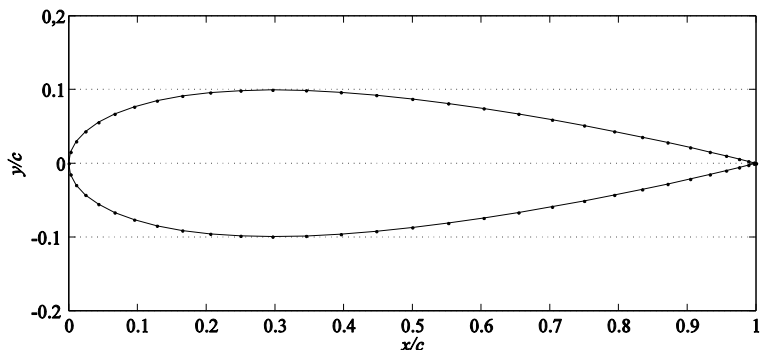


Fig. 6 Blade profile NACA0020 with surface divisions

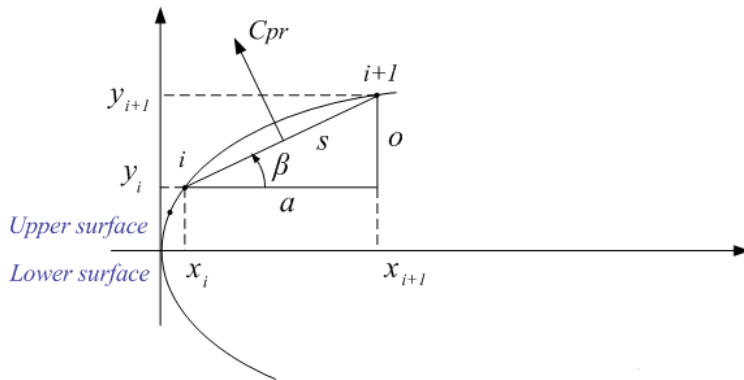


Fig. 7 Pressure coefficient acting on the blade profile divided surface

In order to calculate the length of each segment s there is the need to calculate the length o of the triangles opposite side and the length a of the triangle's adjacent side, which are respectively given by:

$$a = x_{i+1} - x_i \quad (25)$$

$$\begin{cases} o = y_{i+1} - y_i & \text{uppersurface} \\ o = y_i - y_{i+1} & \text{lower surface} \end{cases} \quad (26)$$

When $o > 0$ it means that the surface segment is oriented in the direction to the wind turbine rotation. When $o < 0$ the segment is oriented in the opposite direction. The segment length s , and the segment angle β , in relation to the chord axis, are given by:

$$s = \sqrt{a^2 + |o|^2} \quad (27)$$

$$\beta = \arctan\left(\frac{o}{a}\right) \quad (28)$$

The C_{pr} contribution to the forward movement of the wind turbine (the contribution to the tangential force T_{pr}), the C_{pr} contribution to the forces exerted in a radial axis (the contribution to the normal force N_{pr}) and the angle φ of the C_{pr} exerted on the blade surface in relation to the chord line are shown in Fig. 8.

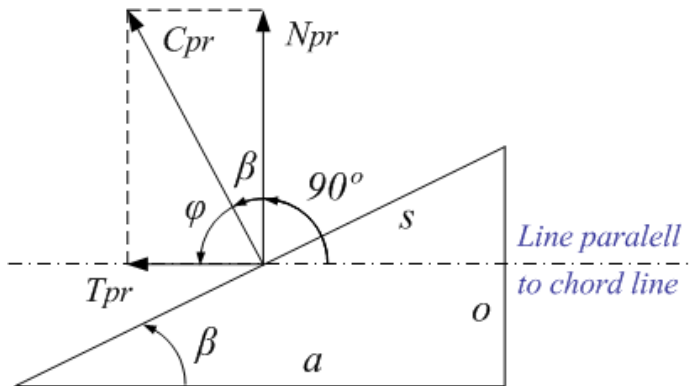


Fig. 8 Pressure coefficient, chordal and normal forces acting on the blade profile surface.

The angle φ of the C_{pr} exerted on the blade surface in relation to the chord line is given by:

$$\varphi = 180^\circ - 90^\circ - \beta \quad (29)$$

The relationships between C_{pr} , T_{pr} , N_{pr} and φ are given by:

$$\begin{cases} T_{pr} = C_{pr} \cos(\varphi)s & \text{when } o \geq 0 \\ T_{pr} = -C_{pr} \cos(\varphi)s & \text{when } o < 0 \end{cases} \quad (30)$$

$$\begin{cases} N_{pr} = C_{pr} \sin(\varphi)s & \text{uppersurface} \\ N_{pr} = -C_{pr} \sin(\varphi)s & \text{lower surface} \end{cases} \quad (31)$$

The analysis of the relation between the blade profile design changes and the wind turbine behavior when it's in a stopped position (at any given axial position) is now possible.

5. Case Studies

The new methodology to study the self-start capabilities of the blade profiles for Darrieus type VAWT has been applied on two case studies: one with several symmetrical NACA airfoils, and a second one with asymmetrical airfoils. But, before the analyses are presented, the computational tool used for the C_{pr} calculation will be presented in the next subsection.

5.1. Pressure Coefficient Analyses in Each Blade Airfoil Segment

The aerodynamic behavior and performance data for different blade profiles is not always available, and in the majority of the cases is incomplete. This data is very hard to obtain and it is a very time-consuming task. Several computational fluid dynamics tools are commonly used to generate the aerodynamic performance data needed. The JavaFoil [36] is a fast processing computational tool. The JavaFoil presents several problems at high

angles of attack, but is used in this paper for simplification of presentation and to facilitate the reader data reproducibility.

This computational tool is able to analyze different blade profiles of any configuration, offering all kind of different output data, for instance: velocity and pressure coefficient distribution along the blade chord; lift, drag and momentum coefficient; flow field with pressure vectors; flow stream lines and pressure distribution along the fluid flow; boundary layer evaluation cards; polar card evaluation with the relations between lift and drag coefficients and with the angle of attack variation; and other information. It is also able to evaluate multi-foil and ground effect configurations. One important feature of the JavaFoil is the ability to save all the analysis and output data to a file. Adding the last feature to its integrated scripting module, it is possible to automate the computational processes and to complement the information needs with other tools.

In the theoretical background of the tool, it uses several methods for airfoil analysis, mainly divided in two main areas:

- Potential Flow Analysis. This analysis is done by a panel method with a linear varying vorticity distribution based on XFOIL code. This method is used to calculate the velocity distribution along the surface of the airfoil;
- Boundary Flow Analysis. This analysis is done on the upper and lower surfaces of the airfoil with different equations, starting with the panel method and performing several calculations in a called integral boundary layer method.

Depending on the Reynolds number and other parameters, the tool gives us the ability to choose different analysis methods and configurations, offering more flexibility to the computational processing.

To apply the JavaFoil computational tool for the C_{pr} calculation, a division of the blade path around the rotor and the axial angles in relation to the flow movement is needed. Hence, the rotor division to study the self-start behavior of the VAWT is shown in Fig. 9.

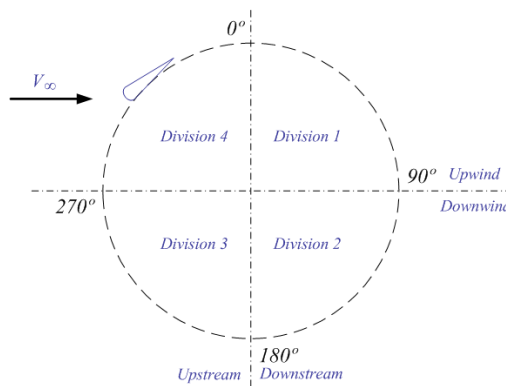


Fig. 9 Rotor division to study the self-start behavior

5.2. Symmetrical Airfoils Analysis

For the symmetrical airfoils data evaluation, the following NACA profiles were selected: NACA0012, NACA0018, NACA0020, NACA0025, and NACA0030.

The NACA0012 and NACA0018 are classical blade profiles used in the VAWT. These profiles are considered to have low self-start capabilities. The thicker NACA0020 blade

profile can be commonly found in the straight-bladed Darrieus wind turbine. The thicker blades show a better self-start performance. The NACA0030 is closer of having self-start capacity nature due to a thicker blade profile. However, a thicker blade leads to an increased drag at high TSR, leading to a performance decrease. The five blade profiles are shown in Fig. 10.

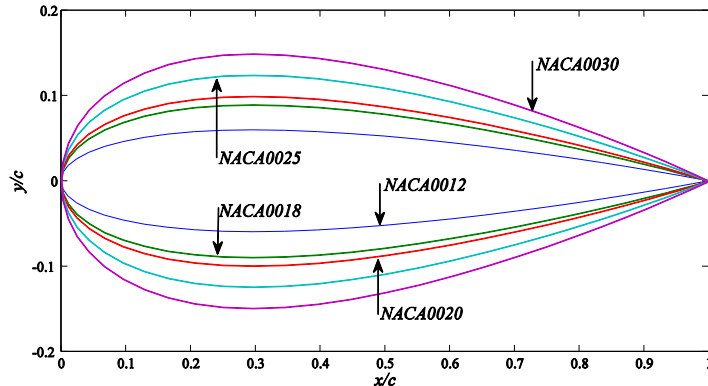


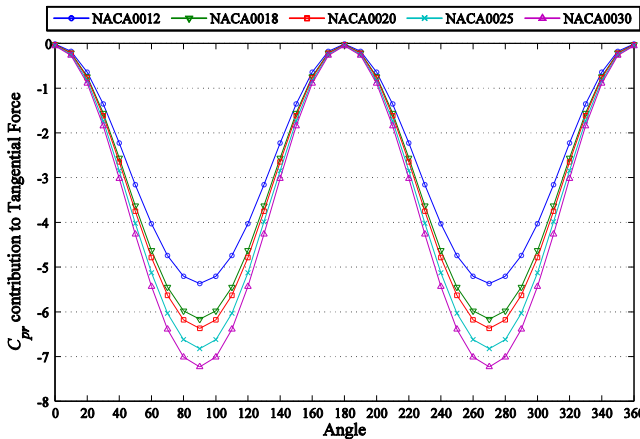
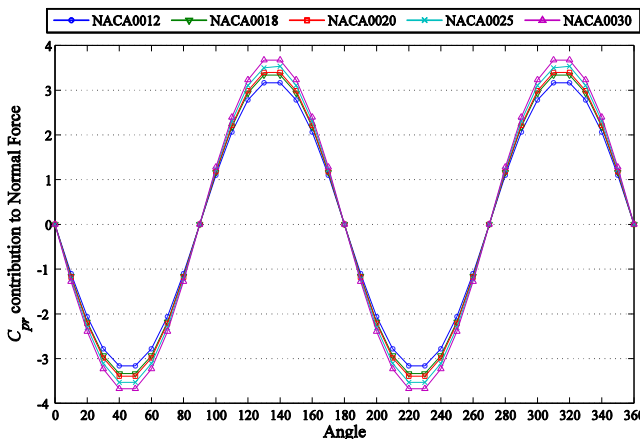
Fig. 10 NACA0012, NACA0018, NACA0020, NACA0025 and NACA0030 blade profiles

In order to apply the proposed methodology, the pressure coefficient needs to be calculated around the blade profile. For the data evaluation presented here, the C_{pr} is calculated for all segments around the blade profile for any given angle between 0° and 360° . The JavaFoil tool offers the pressure coefficient evaluation associated with the x and y coordinates. This evaluation can be automatically performed to the entire 360° at the same time in the velocity area.

By applying (25) and (26) to the given x and y coordinates, the opposite side and the adjacent side are obtained. By applying (27), the length of the airfoil surface exposed to the wind forces can be obtained. Also, using (28) and (29), the C_{pr} angle in relation to the blade chord line φ is determined.

Taking into account all the data previously calculated, it is now possible to determine the C_{pr} contribution to the tangential force T_{pr} and the C_{pr} contribution to the normal force N_{pr} . These forces are related to the actual tangential and normal forces responsible for the blades movement, by the pressure coefficient.

The C_{pr} contribution to the tangential force T_{pr} and the C_{pr} contribution to the normal force N_{pr} , for the chosen NACA airfoils, are shown in Fig. 11 and Fig. 12 respectively.

Fig. 11 C_{pr} contribution to the tangential force T_{pr} Fig. 12 C_{pr} contribution to the normal force N_{pr}

On one hand, it can be seen in Fig. 11 that a thicker blade implies a higher-pressure coefficient contribution to the forward movement of the wind turbine blades (contribution to the tangential force). Indeed, the NACA0030 presents 26% better performance than the NACA0012. On the other hand, it can be seen in Fig. 12 that the airfoil NACA0012 presents the most desirable behavior. Smaller axial forces imply lesser need of blade/arms connection reinforcements.

When the wind turbine is in a stopped position the drag forces have a considerable contribution to the self-start of the wind turbine. Taking in consideration the divisions shown in Fig. 9, there is the need to increase the drag exerted on the blades when they are positioned in divisions 2 and 3. The pressure coefficient is also used to study the drag contribution to the forward movement of the wind turbines blades. In an incompressible flow, when the pressure coefficient reaches values between one and null, that is a stagnation point. The study of the values that contribute to the forward movement of the wind turbine blades are shown in Fig. 13.

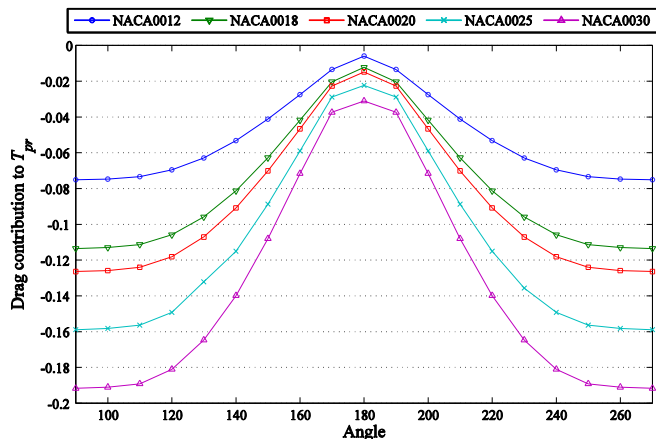


Fig. 13 Drag contribution to the forward movement of the wind turbine blades T_{pr}

In Fig. 13 it can be seen that thicker blades imply higher drag contribution to the forward movement of the wind turbine blades. The drag forces contributing to the tangential force are 150% higher in the NACA0030 than in the NACA0012.

Hence, it was clearly shown that thicker blades are able to provide the wind turbine with self-start capabilities, while the thinner blade wind turbines are most likely unable to self-start.

5.3. Asymmetrical Airfoils Analysis

In asymmetrical airfoils the profile curvature and form may have a direct influence in the wind turbine self-start performance.

To study the influence of the camber size, the NACA0012, NACA2412, NACA4412, NACA6412, NACA8412 and NACA10412 blade profiles were selected, are shown in Fig. 14.

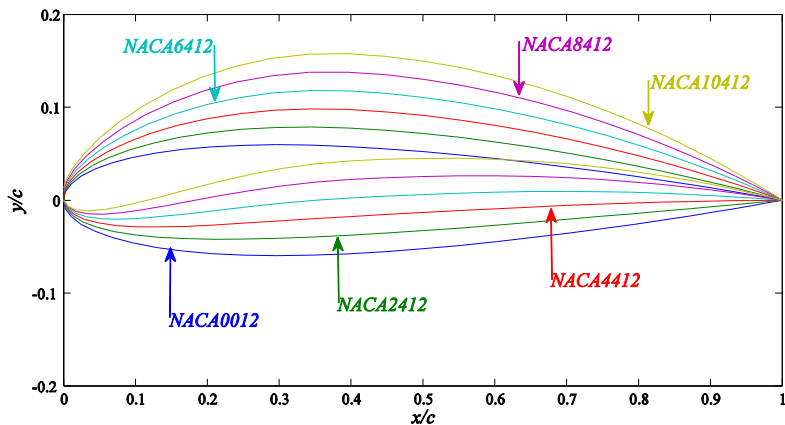


Fig. 14 NACA0012, NACA2412, NACA4412, NACA6412, NACA8412 and NACA10412 blade profiles

All these profiles have 12% of thickness in relation to the chord line size and a camber positioned at 40% of the chord line. The camber sizes in all profiles vary in 2% of the chord line size.

To study the influence of the camber position, the NACA4112, NACA4212, NACA4412, NACA4612, NACA4812 and NACA4912 blade profiles were selected, as shown in Fig. 15.

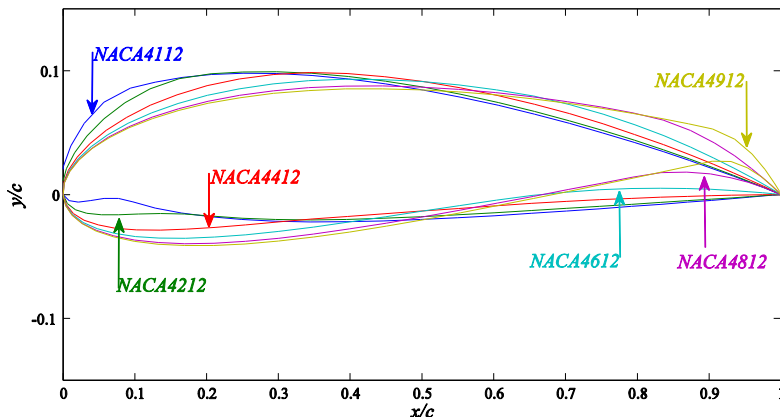


Fig. 15 NACA4112, NACA4212, NACA4412, NACA4612, NACA4812 and NACA4912 blade profiles

All these profiles have 12% of thickness in relation to the chord line size and a camber size of 4% of the chord line size. The profiles vary in the camber position in relation to the chord line at 10%, 20%, 40%, 60%, 80% and 90%, respectively.

The NACA0012 with 12% of thickness, in relation to the blade chord size, and the NACA0018 with 18% of thickness are the classical blade profiles used in the VAWT. These profiles have been studied several times and have a large amount of real measurement data available in the scientific community. These data availability simplifies the prediction simulation, leading to an increased acceptance of these airfoils in the VAWT developments, influencing the acceptance of these profiles in the final turbines. However, these profiles are considered to have low self-start capabilities, for which thicker blades show better performance.

The influence of the camber curvature size and the influence of the camber position are evaluated. The C_{pr} contribution to the tangential force T_{pr} and the C_{pr} contribution to the normal force N_{pr} were calculated, as occurred with the symmetrical airfoils.

The pressure coefficient C_{pr} contribution to the tangential force T_{pr} by varying the blade profile camber curvature size is shown in Fig. 16.

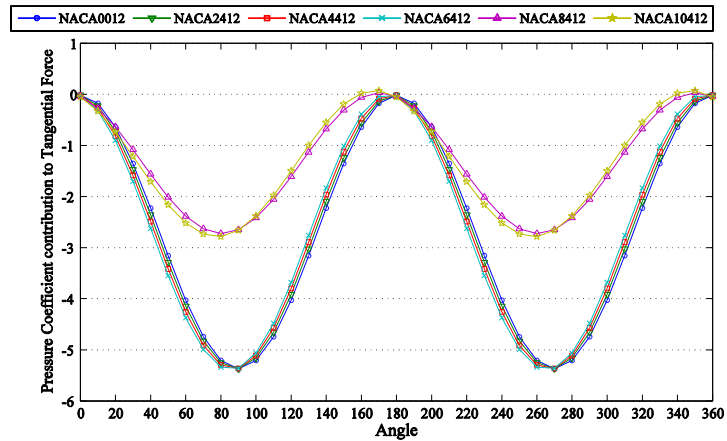


Fig. 16 Pressure coefficient C_{pr} contribution to the tangential force T_{pr} by varying the blade profile camber curvature size

The pressure coefficient C_{pr} contribution to the normal force N_{pr} by varying the blade profile camber curvature size is shown in Fig. 17.

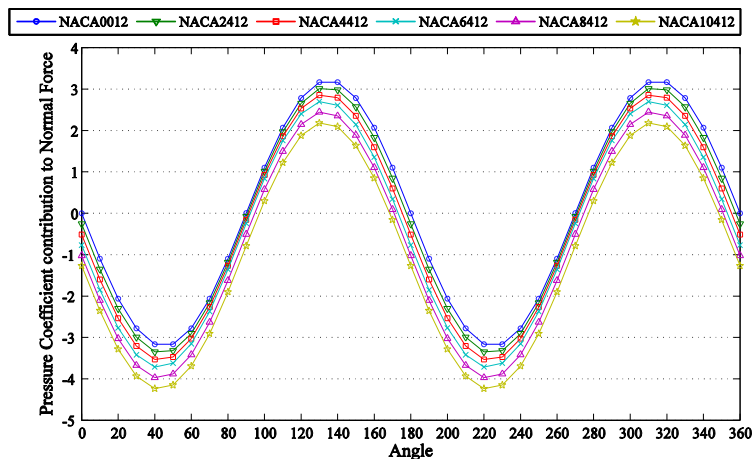


Fig. 17 Pressure coefficient C_{pr} contribution to the normal force N_{pr} by varying the blade profile camber curvature size

The drag contribution to the forward movement of the wind turbine blades by varying the blade profile camber curvature size is shown in Fig. 18.

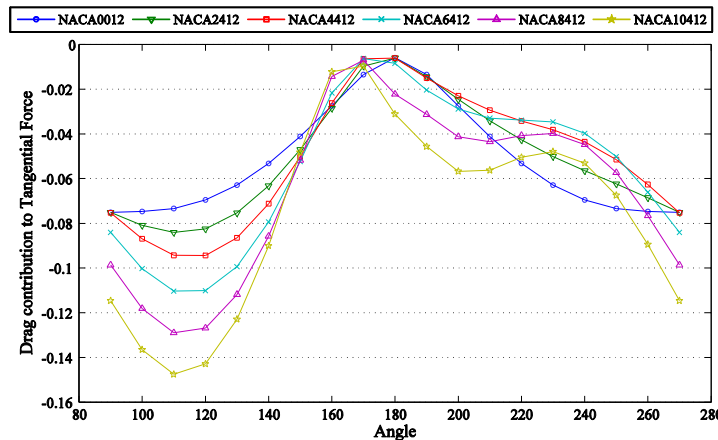


Fig. 18 Drag contribution to the forward movement of the wind turbine blades by varying the blade profile camber curvature size

Fig. 16, Fig. 17 and Fig. 18 presented the airfoil performance evaluation data by applying the new methodology to the variation of the camber curvature size.

The pressure coefficient C_{pr} contribution to the tangential force T_{pr} by varying the blade profile camber position is shown in Fig. 19.

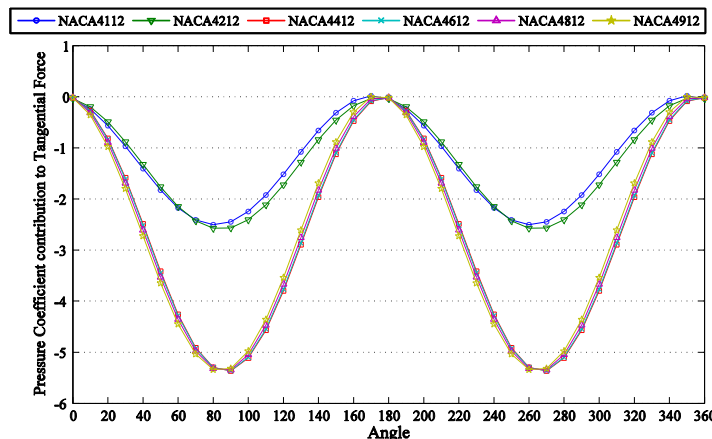


Fig. 19 Pressure coefficient C_{pr} contribution to the tangential force T_{pr} by varying the blade profile camber position

The pressure coefficient C_{pr} contribution to the normal force N_{pr} by varying the blade profile camber curvature size is shown in Fig. 20.

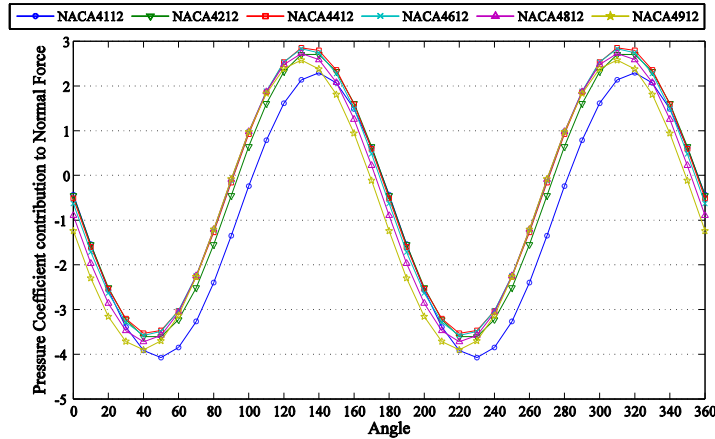


Fig. 20 Pressure coefficient C_{pr} contribution to the normal force N_{pr} by varying the blade profile camber position

The drag contribution to the forward movement of the wind turbine blades by varying the blade profile camber curvature size is shown in Fig. 21.

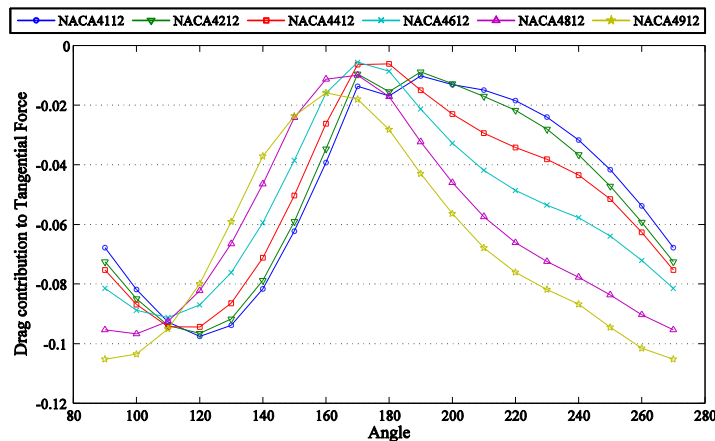


Fig. 21 Drag contribution to the forward movement of the wind turbine blades by varying the blade profile camber position

Fig. 19, Fig. 20 and Fig. 21 presented the airfoil performance evaluation data by applying the new methodology to the variation of the camber position in relation to the airfoil chord.

5.3.1 Camber Curvature Size Variation

In Fig. 16 it can be seen that curvature size doesn't influence the pressure coefficient contribution to the forward movement of the wind turbine blades until it reaches values higher than 6% of the blade chord size. The blade profiles with 8% and 10% sized cambers suffer a performance decrease of 40%.

In Fig. 17 it can be seen that the airfoil NACA0012 presents the most desirable behavior. Smaller axial forces imply lesser need of blade/arms connection reinforcements. Also,

higher camber curvature sizes imply higher displacement of the exerted forces to the outside of the wind turbine and lower to the inside of the rotor.

When the wind turbine is in a stopped position the drag forces have a considerable contribution to the self-start of the wind turbine, especially when the blades are positioned in the downwind side of the rotor.

The pressure coefficient is also used to study the drag contribution to the forward movement of the wind turbine blades. In an incompressible flow, when the pressure coefficient reaches values between one and null, that is a stagnation point. The study of the values that contribute to the forward movement of the wind turbine blades are shown in Fig. 18. It can be seen that higher blade profile camber curvature sizes imply higher drag forces contributing to the forward movement of the wind turbine blades. The airfoil NACA0012 has a symmetrical behavior between the 90° to 180° and 180° to 270° due to its symmetrical shape in the upper and lower airfoil surfaces.

5.3.2 Camber Position Variation

In Fig. 19 it can be seen that when the camber curve is positioned in the first 40% of the blade chord line, a 50% performance decrease occurs compared with the cambers positioned in the last 60% of the blade chord line.

It can be seen in Fig. 20 that the blade chord position does not have a significant influence to the axial exerted forces, except when it is positioned at 10% of the airfoil chord line.

It can be seen in Fig. 21 that the better behaviors are presented by the airfoils that have the cambers positioned in the middle of the chord line.

5.4. Self-start Simulation

In Fig. 22 it can be seen a simulation of a straight blade Darrieus VAWT with 1 m blade and 0.5 m radius. Two wind turbines are compared, one with the symmetrical blade profile NACA0012 and other with the asymmetrical blade profile NACA4412. The simulation is done by the qBlade software [37]. For the of the VAWT start simulation the wind velocity was set to 3 m/s and the wind turbines TSR set to 1.

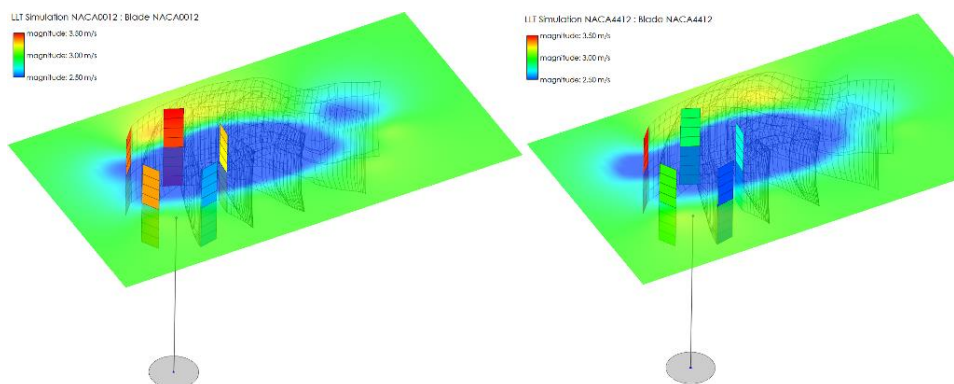


Fig. 22 Symmetrical blade profile NACA0012 and asymmetrical blade profile NACA4412
Darrieus VAWT start simulation

5.5. Blade Development by Applying the New Methodology

A new blade profile for Darrieus VAWT named EN0005 was created by applying the new methodology presented in this paper. The new profile offers self-start to a Darrieus VAWT and good performance at high TSR [32,38-40]. The blade profile EN0005 is presented in Fig. 23.

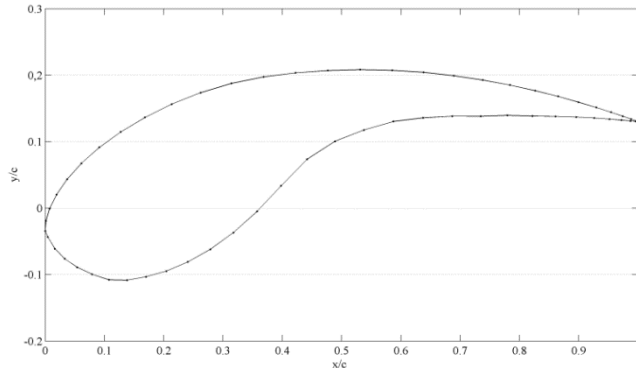


Fig. 23 Blade profile EN0005

The ANSYS FLUENT computational tool is used to generate the aerodynamic performance data presented in the following analysis and comparison instead of the JavaFoil, since it presents a more accurate and validated good accuracy although more difficult to use.

In Fig. 24 and Fig. 25 the blade profile EN0005 C_{pr} contribution to the T_{pr} and N_{pr} respectively is compared with the symmetrical profiles NACA0018 and NACA0020 and asymmetrical profiles NACA4418 and NACA4420 same data.

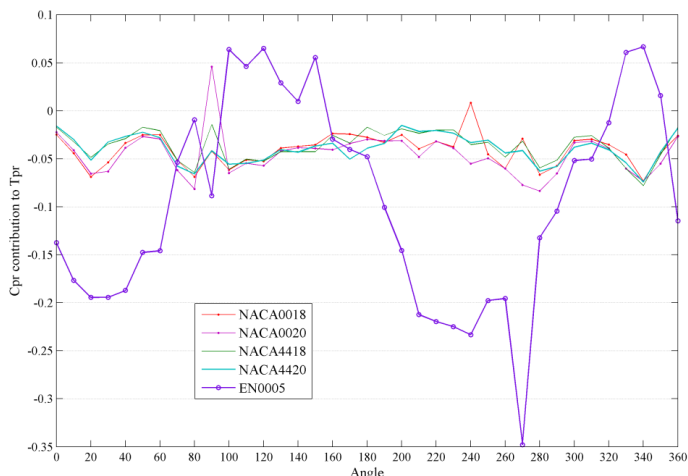


Fig. 24 C_{pr} contribution to the tangential force T_{pr}

Fig. 24 shows a better capability for the blade profile EN0005 to offer self-start capability to the Darrieus VAWT. From angle 0° to 80° and 180° to 310° The EN0005 blade profile

presents a better contribution to the lift force. Also, the EN0005 presents a drag force contributing for the forward movement of the Darrieus VAWT between the angles 100° and 150° and presents a lower variation in the normal force between the 70° and 180°. Although with inversed orientation for the remaining angles, the normal force is very similar to the other blade profiles. The self-start ability that blade profile EN0005 offers is validated in the independent work [32].

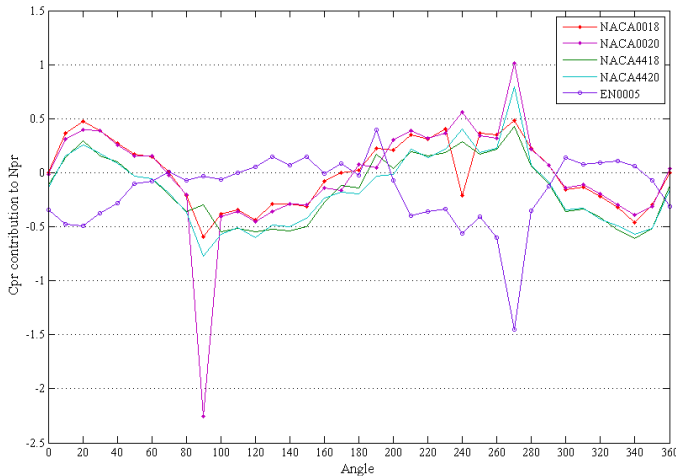


Fig. 25 C_{pr} contribution to the normal force N_{pr}

6. Conclusions

- This paper focused on the study and development of new blade profiles for Darrieus type VAWT capable to self-start without the use of extra components or external energy input. A new methodology for fast development and its associated equations have been presented, in order to study the influences of the wind on the turbine in its stopped position. This new methodology gives a close relation between the blade profile design and the wind forces acting on the blades.
- Two case studies were provided: one with symmetrical NACA airfoils and other with asymmetrical airfoils. In the asymmetrical airfoils, a closer study to the camber curvature size and position has also been presented. The comprehensive results obtained from the two case studies are in very good agreement with other works in the scientific community, validating the proficiency and usefulness of the proposed methodology.
- A real case of a new blade profile developed with the methodology presented in this paper is shown. The new blade profile called EN0005 presents the ability to offer self-start capabilities to a Darrieus VAWT.

Acknowledgment

This work is funded by: European Union through the European Regional Development Fund, included in the COMPETE 2020 (Operational Program Competitiveness and

Internationalization) through the ICT project (UID/GEO/04683/2013) with the reference POCI010145FEDER007690; Portuguese Funds through the Foundation for Science and Technology-FCT under the project LAETA 2015-2020, reference UID/EMS/50022/2013; Portuguese Foundation for Science and Technology (FCT) under Project UID/EEA/04131/2013.

Nomenclature

A	Area swept by the wind turbine	Q	Turbine overall torque
a	Blade profile surface segment adjacent	r	Turbine rotor radius
c	Blade profile chord	R_e	Reynolds number
C_d	Blade drag coefficient	s	Blade profile surface segment
C_D	Turbine drag coefficient	T_{pr}	Pressure coefficient contribution to the tangential force
C_l	Blade lift coefficient	V_∞	Undisturbed wind velocity
C_m	Blade momentum coefficient	V_a	Induced velocity
C_P	Power coefficient	V_r	Induced velocity due to the rotor angular speed at the wind turbine
C_{pr}	Pressure coefficient	V_c	Chordal velocity component
C_{prl}	Pressure coefficient in the lower surface	V_n	Normal velocity component
C_{pru}	Pressure coefficient in the upper surface	V_{au}	Induced velocity in the upstream
C_Q	Turbine overall torque coefficient	V_{ad}	Induced velocity in the downstream
C_t	Tangential force coefficient	V_e	Wake velocity in the upstream
C_n	Normal force coefficient	V_w	Wake velocity in the downstream
D	Blade drag force	u_d	Interference factor for the downstream
F_D	Turbine drag force	u_u	Interference factor for the upstream
F_t	Tangential force	W	Relative flow velocity
F_n	Normal force	α	Blade angle of attack
F_{ta}	Average tangential force	β	Blade profile surface segment angle in relation to the chord line
h	Turbine height	γ	Blade pitch angle
k	Factor found by iteration	θ	Blade azimuth angle around the rotor
L	Blade lift force	ρ	Fluid density
n	Number of blades	λ	Tip speed ratio
N_{pr}	Pressure coefficient contribution to the normal force	μ	Dynamic viscosity of the fluid
o	Blade profile surface segment opposite	σ	Turbine solidity
P	Turbine overall power	v	Kinematic viscosity of the fluid
p	Pressure of the point where the evaluation of the pressure coefficient is made	φ	Pressure coefficient angle in relation to the chord line
p_∞	Pressure of the undisturbed wind	ω	Rotor angular speed at the wind turbine

References

- [1] Francese D., Adamo E., Khanmohammadi S. Micro-aeolic in residential districts: a Case study in Sant'Arsenio (south-western Italy). Mediterranean Green Buildings and Renewable Energy 2017; 369-377.
- [2] Jäger-Waldau A. PV Status Report 2017. Publications Office of the European Union 2017.
- [3] Melicio R., Mendes V.M.F., Catalão J.P.S. Computer simulation of wind power systems: power electronics and transient stability analysis. Proceedings of the Int. Conference on Power Systems Transients (IPST 2009), 1-7, Kyoto, Japan, June 2009.
- [4] Batista N.C., Melicio R., Matias J.C.O, Catalão J.P.S. ZigBee standard in the creation of wireless networks for advanced metering infrastructures. Proceedings of the 16th IEEE Mediterranean Electrotechnical Conference, 220-223, Medina Yasmine Hammamet, Tunisia, March 2012. <https://doi.org/10.1109/MELCON.2012.6196418>
- [5] Melicio R., Mendes V.M.F., Catalão J.P.S. Modeling, control and simulation of full-power converter wind turbines equipped with permanent magnet synchronous generator. International Review of Electrical Engineering 2010; 5(2): 397-408.
- [6] Melicio R., Mendes V.M.F., Catalão J.P.S. Modeling and simulation of wind energy systems with matrix and multilevel power converters. IEEE Latin America Transactions 2009; 7(1): 78-84. <https://doi.org/10.1109/TLA.2009.5173468>
- [7] Arab A., Javadi M., Anbarsooz M., Moghimian M. A numerical study on the aerodynamic performance and the self-starting characteristics of a Darrieus wind turbine considering its moment of inertia. Renewable Energy 2017; 107: 298-311. <https://doi.org/10.1016/j.renene.2017.02.013>
- [8] D'Alessandro V., Montelpare S., Ricci R., Secchiaroli A. Unsteady aerodynamics of a Savonius wind rotor: a new computational approach for the simulation of energy performance. Energy, 2010; 35: 3349-3363. <https://doi.org/10.1016/j.energy.2010.04.021>
- [9] Shigetomi A., Murai Y., Tasaka Y., Takeda Y.. Interactive flow field around two Savonius turbines. Renewable and Sustainable Energy Reviews, 2011; 36: 536-545. <https://doi.org/10.1016/j.renene.2010.06.036>
- [10] Hill N., Dominy R., Ingram G., Dominy J. Darrieus turbines: the physics of self-starting. Proceedings of the Institution of Mechanical Engineers, Part A: Journal of Power and Energy, 2009; 223: 21 - 29. <https://doi.org/10.1243/09576509JPE615>
- [11] Castelli M.R., Englano A., Benini E. The Darrieus wind turbine: proposal for a new performance prediction model based on CFD. Energy, 2011; 36: 4919 - 4934. <https://doi.org/10.1016/j.energy.2011.05.036>
- [12] Kjellin J., Bulow F., Eriksson S., Deglaire P., Leijon M., Bernhoff H. Power coefficient measurement on a 12 kW straight bladed vertical axis wind turbine. Renewable Energy, 2011; 36: 3050 - 3053. <https://doi.org/10.1016/j.renene.2011.03.031>
- [13] Islam M., Ting D.S.K., Fartaj A. Aerodynamic models for Darrieus-type straight-bladed vertical axis wind turbines. Renewable and Sustainable Energy Reviews, 2008; 12: 1087 - 1109. <https://doi.org/10.1016/j.rser.2006.10.023>
- [14] Ponta F.L., Seminara J.J., Otero A.D. On the aerodynamics of variable-geometry oval-trajectory Darrieus wind turbines. Renewable Energy, 2007; 32: 35 - 56. <https://doi.org/10.1016/j.renene.2005.12.007>
- [15] Paraschivou I., Trifu O., Saeed F. H-Darrieus wind turbine with blade pitch control. Int J Rotating Machinery, 2009; 2009: 1 - 7. <https://doi.org/10.1155/2009/505343>
- [16] Batista N.C., Melicio R., Mendes V.M.F., Figueiredo J., Reis A.H. Darrieus wind turbine performance prediction: computational modeling. Technological Innovation for the Internet of Things, SPRINGER, Heidelberg, Germany, April 2013; 382-391.
- [17] Gazzano R., Marini M., Satta A. Performance calculation for a vertical axis wind turbine with variable blade pitch. Int J Heat and Technology, 2010; 28: 147 - 153.
- [18] Anderson F., Fletcher T.M., Brown R.E. Simulating the aerodynamic performance and wake dynamics of a vertical-axis wind turbine. Wind Energy, 2011; 14: 159 - 177. <https://doi.org/10.1002/we.409>

- [19] Islam M., Amin M.R., Ting D.S.K., Fartaj A. Aerodynamic factors affecting performance of straight-bladed vertical axis wind turbines. Proceedings of the ASME Int Mechanical Engineering Congress and Exposition, Washington, USA, November, 2007. <https://doi.org/10.1115/IMECE2007-41346>
- [20] Ferreira C.S., van Kuik G., van Bussel G., Scarano F. Visualization by PIV of dynamic stall on a vertical axis wind turbine. Experiments in Fluids, 2009; 46: 97 – 108. <https://doi.org/10.1007/s00348-008-0543-z>
- [21] Ferreira C.J.S., van Zuijlen A., Bijl H., van Bussel G., van Kuik G. Simulating dynamic stall in a two-dimensional vertical-axis wind turbine: verification and validation with particle image velocimetry data. Wind Energy, 2010; 13: 1 – 17. <https://doi.org/10.1002/we.330>
- [22] Greenblatt D., Schulman M., Ben-Harav A. Vertical axis wind turbine performance enhancement using plasma actuators. Renewable Energy, 2012; 37: 345 – 354. <https://doi.org/10.1016/j.renene.2011.06.040>
- [23] Balduzzi F., Bianchini A., Carnevale E.A., Ferrari L., Magnani S. Feasibility analysis of a Darrieus vertical-axis wind turbine installation in the rooftop of a building. Applied Energy, 2012; 97: 921 – 929. <https://doi.org/10.1016/j.apenergy.2011.12.008>
- [24] Qin N., Howell R., Durrani N., Hamada K., Smith T. Unsteady flow simulation and dynamic stall behaviour of vertical axis wind turbine blades. Wind Engineering, 2011; 35: 511-527. <https://doi.org/10.1260/0309-524X.35.4.511>
- [25] Zannetti L., Gallizio F., Ottino G. Vortex capturing vertical axis wind turbine. J of Physics Conf Series, 2007; 75: 1-10. <https://doi.org/10.1088/1742-6596/75/1/012029>
- [26] Dominy R., Lunt P., Bickerdyke A., Domniny I. Self-starting capability of a Darrieus turbine. Proc Inst Mech Eng Part A-J Power Energy, 2007; 211: 111-120. <https://doi.org/10.1243/09576509JPE340>
- [27] Shahizare B., Nik-Ghazali N., Chong W.T., Tabatabaeikia S., Nima I., Alireza E. Novel investigation of the different Omni-direction-guide-vane angles effects on the urban vertical axis wind turbine output power via three-dimensional numerical simulation. Energy Conversion and Management, 2016; 117: 206–217. <https://doi.org/10.1016/j.enconman.2016.03.034>
- [28] Xiaoting L., Sauchung F., Baoxing O., Chili W., Christopher C., Kaihong P. A computational study of the effects of the radius ratio and attachment angle on the performance of a Darrieus-Savonius combined wind turbine. Renewable Energy, 2017; 113: 329-334. <https://doi.org/10.1016/j.renene.2017.04.071>
- [29] Bhuyan S., Biswas A. Investigations on self-starting and performance characteristics of simple H and hybrid H-Savonius vertical axis wind rotors. Energy Conversion and Management, 2014; 87: 859-867. <https://doi.org/10.1016/j.enconman.2014.07.056>
- [30] Chen J.S.J., Chen Z., Biswas S., Miau J.J., Hsieh C.H. Torque and power coefficients of a vertical axis wind turbine with optimal pitch control. Proceedings of the ASME 2010 Power Conference, Illinois, USA, July, 2010. <https://doi.org/10.1115/POWER2010-27224>
- [31] Bhatta P., Paluszek M.A., Mueller J.B. Individual blade pitch and camber control for vertical axis wind turbines. Proceedings of the World Wind Energy Conf 2008, Kingston, Canada, June, 2008.
- [32] Sengupta A.R., Biswasa A., Guptab R. Studies of some high solidity symmetrical and unsymmetrical blade H-Darrieus rotors with respect to starting characteristics, dynamic performances and flow physics in low wind streams. Renewable Energy 2016; 93: 536-547. <https://doi.org/10.1016/j.renene.2016.03.029>
- [33] Sayyad B.Q., Isam J. Investigation of effect of cambered blades on Darrieus VAWTs. Energy Procedia 2017; 105: 537-543. <https://doi.org/10.1016/j.egypro.2017.03.353>
- [34] Chi-Cong N., Thi-Hong-Hieu L., Phat-Tai T. A numerical study of thickness effect of the symmetric NACA 4-digit airfoils on self starting capability of a 1 kW H-type vertical axis wind turbine. International Journal of Mechanical Engineering and Applications. Special Issue: Transportation Engineering Technology — part II. 2015; 3: 7-16.
- [35] Anderson J.D. Fundamentals of aerodynamics, McGraw-Hill Series in Aeronautical and Aerospace Engineering, New York, NY, USA, 2010.
- [36] Hepperle M. JavaFoil – Analysis of Airfoils. Available: <http://www.mh-aerotools.de/>.

- [37] Marten D., Wendler J., Pechlivanoglou G., Nayeri C.N., Paschereit C.O. Qblade: an open source tool for design and simulation of horizontal and vertical axis wind turbines. Emerging Technology and Advanced Engineering 2013; 3: 264-269.
- [38] Batista N.C., Melicio R., Mendes V.M.F., Calderón M., Ramiro A.. On a self-start Darrieus wind turbine: Blade design and field tests. Renewable and Sustainable Energy Reviews 2015; 52: 508-522. <https://doi.org/10.1016/j.rser.2015.07.147>
- [39] Batista N.C., Melicio R., Catalão J.P.S. Vertical axis turbine blades with adjustable form. Patent US 2012/0163976A1; 2012.
- [40] Batista N.C., Melicio R., Matias J.C.O., Catalão J.P.S. New blade profile for Darrieus wind turbines capable to self-start. Proceedings of the Renewable Power Generation Conference, 1–5, Edinburgh, UK, September 2011. <https://doi.org/10.1049/cp.2011.0219>



Research Article

Optimization applied to dynamic poroelasticity using boundary element method (BEM) and genetic algorithm (GA)

Anunciação Jr.N. C *¹, Anflor C.T.M¹, Goulart J.N.V¹

¹ Group of Experimental and Computational Mechanics (GMEC), University of Brasilia, Brazil

Article Info	Abstract
<i>Article history:</i>	
Received 08 Nov 2017	
Revised 19 Mar 2018	
Accepted 26 Mar 2018	
<i>Keywords:</i>	
Poroelasticity, Dynamic, Soil, BEM, GA	This paper focused on developing a methodology based on coupling the Genetic Algorithm (GA) and the Boundary Element Method (BEM) for predicting the mechanical properties of a soil if a previous displacement x frequency curve is known. The NSGA-II (Elitist Non-Dominated Sorting Genetic Algorithm) was chosen for optimizing a dynamic poroelastic problem. The revisited problem introduced by Cheng is the benchmark used to verify the numerical routine and to apply the proposed optimization procedure. The present methodology was shown to be able to predict the mechanical properties of the underground soil if a displacement x frequency curve is previously known.

© 2018 MIM Research Group. All rights reserved

1. Introduction

During the last decade, countless efforts have been made to increase the capacity to exploit underground resources. It is well known that in the deepest regions there is a large amount of water, oil and gas reservoirs. The characteristics of the soil will determine what kind of resources will be present within it. The great complexity of the problems and the increasing availability of computational resources open up opportunities for the use of more comprehensive analyses. This kind of analysis is related to the concepts of soil mechanics that was first introduced by Terzaghi [1] in the theory of elasticity and the theory of limit analysis (plasticity). Subsequently, Biot and Willis [2] presented the theory of consolidation, which is the basis for studies regarding to the poroelasticity of the soil.

The problems that arise in poroelasticity are related to the consolidation of layers of soil, excavations in saturated pores (such as tunnels), pumping (removal) of fluid (petroleum or water) by saturated porous medium, among others. The propagation of waves and consolidation of soil has long been a topic for study. Terzaghi [3] and Gassmann [4] provided wave propagation results in porous media at low frequency (0-100 Hz), considering the solid and fluid phases as unique. After some years analyzing the wave's propagation in poroelastic medium, Biot developed the theory of dynamic consolidation of soil. This study was divided in two parts, where the first one regards the elastic wave propagation in a saturated porous medium for low frequencies, and the second one for high frequencies. Through the previous studies introduced by Biot [5-6], two different types of wave propagation were observed, the primary and secondary. The primary is the compression or longitudinal waves and the secondary are the shear, distortion or

*Corresponding author: anflor@unb.br

DOI: <http://dx.doi.org/10.17515/jresm2017.34ds1108>

rotational waves. Plona [7] experimentally registered the existence of slow waves. In order to describe the porous medium two scales are needed. The first one is the macroscopic scale (related to the dimensions of a representative volume) and the second one is related to pore dimension which is microscopic in scale. These problems can be represented by using mathematical formulations, allowing the modelling through numerical methods. Introduced in this work is a numerical methodology for wave propagation based on Biot's theory of poroelasticity [8] coupled with Thierzagi's theory of consolidation [1]. This numerical methodology applies the boundary element method (BEM) for solving the consolidation phenomena of poroelastic media problems. All differential equations were transformed into integral equations by using the reciprocity theorem. The behavior of poroelastic medium is still an object of study, and all the basic concepts solved by Biot can be applied. Schanz and Paryl [9] applied the poroelastic formulations in a dynamic analysis of compressible and incompressible media, i.e. solid and fluid. They observed that the behaviors of derivations of fundamental solutions confirmed the fact that the solid displacement and the pore pressure (fluid) are sufficient to describe the behavior of a poroelastic medium, affirming the theory of Biot. A simplified model of dynamic analysis on viscoelastic and poroelastic soils is presented by Millán and Domínguez [10], where dynamic coefficients of behavior were found through numerical formulations using the finite element method (FEM) and the BEM. Gensterblum [11] performed measurements of permeability in gases in the process of extraction of high quality bituminous coal, considering the dynamic and poroelastic aspects. The gases interaction and coupling of the gases were analyzed by using the Darcy's Equation. Hydraulic parameters were analyzed by Berg [12]. In this study the effects of pumping in aquifers resulted in pore pressure changes which were predicted by the traditional groundwater theory. Apostolakis and Dargush [13] used the analogy between thermoelastic and poroelastic theories first identified by Biot, and then developed a corresponding mixed variational principle for fluid-infiltrated porous bodies. They developed a poroelastic formulation in close mathematical analogy with the thermoelastic system particularized to the solid skeleton displacement, impulse of the effective stress, impulse of pore pressure and total average fluid displacement. According to this work, the physical analogy is not complete, as the contributions from the extended Fourier and Darcy laws are shown to be of a different character. In this sense, some efforts still need to be devoted to the development of new computational approaches in both problem domains (thermoelasticity and poroelasticity).

Considering this, the main goal of this work relies on applying an optimization process in such a way to predict the mechanical properties of soil if a frequency-displacement curve is known. A numerical routine was written in order to couple the NSGA-II (elitist non-dominated sorting genetic algorithm) and the BEM for evaluating a poroelastic dynamic problem. In this work, the Matlab GA toolbox was used while the BEM was completely written in open source code. The remainder of the paper is organized as follows. The poroelasticity theory and the basic equations for dynamic poroelasticity are the focus of Section 2. The development of the BEM for dynamic poroelasticity is presented in Section 3. Section 4 presents the GA methodology using NSGA-II as well as the objective function and the design variables. The theories introduced in the previous sections are applied for solving a revisited problem proposed by Cheng [14]. Finally, conclusions about the optimization process are provided in Section 5.

2. The Poroelasticity Theory

The internal structures of a porous body can be compared to a homogeneous solid, despite the presence of some voids between the grains. The voids can be completely filled or not by a fluid like water, gas or oil. In the theory of poroelasticity, the porous medium is considered as linear elastic, and the pores are considered completely filled with fluid. A

porous medium has a defined volume, which can be divided into two: the volume of the matrix and the volume corresponding to the pores. Porosity is defined by the ratio of pore volume to total volume. The effective stress introduced by Terzaghi [1, 15] is defined as that part that governs the deformation of the soil or rock. The effective stress can be decomposed into the sum of the effective stresses and the pore pressure as

$$\sigma_{ij} = \sigma'_{ij} + \alpha p \delta_{ij} \quad (1)$$

where σ_{ij} is the total stress, σ'_{ij} is the effective stress, p is the pore pressure (fluid pressure in the pores), δ_{ij} is the Kronecker delta and α is the Biot coefficient. For an isotropic media the stress can be written according to Eq. (2).

$$\sigma = \sigma' + \alpha p \quad (2)$$

2.1. Basic Equations for Dynamic Poroelasticity

According to Biot's theory (5), the equilibrium equations for linear poroelasticity are expressed as Eq. (3) and Eq. (4).

$$\tau_{ij,j} + X_i = \frac{\partial^2}{\partial t^2} (\rho_{11} u_i + \rho_{12} U_i) + k \frac{\partial}{\partial t} (u_i - U_i) \quad (3)$$

$$\tau_{,j} + X'_i = \frac{\partial^2}{\partial t^2} (\rho_{12} u_i + \rho_{22} U_i) + k \frac{\partial}{\partial t} (u_i - U_i) \quad (4)$$

where τ_{ij} is the solid stress, τ is the fluid stress due to the fluid pressure p introduced by Eq. (5).

$$\tau = -\beta p \quad (5)$$

where β is the porosity, u_i and U_i are the solid and fluid displacements, respectively. The variables ρ_{11} , ρ_{12} and ρ_{22} are the mass densities and X_i and X'_i concern the body force acting on the solid and fluid, respectively. The relations between the linear equilibrium equations and the mechanical variables are introduced by Eq. (6) and represents the partial solid stress and Eq. (7) the partial fluid stress.

$$\tau_{ij} = \left(\lambda + \frac{\alpha^2}{R} \right) \delta_{ij} e + 2\mu e_{ij} + \alpha \delta_{ij} \varepsilon \quad (6)$$

$$\tau = \alpha e + R \varepsilon \quad (7)$$

where δ_{ij} is the Kronecker delta, $e_{ij} = 0.5 (u_{ij} + u_{ji})$ is the solid strain tensor, $\varepsilon = U_{,i}$ and $e = u_{,i}$ are the fluid and solid dilation, respectively. Finally, there are the elastic constants λ , μ , α and R .

3. The Boundary Element Method for Dynamic Poroelasticity

The boundary integral formulation arises from the reciprocal relation between the terms of the displacements of the solid, boundary conditions of traction, stress in the fluid, boundary conditions of normal displacements in the fluid and body force in both phases. The integral representation for these equations can be written for 2D domain in the absence of body force according to Eq. (8) and (9), where J is defined as Eq. (10) according to Cheng [14].

$$c_{\alpha\beta} u_{\alpha} + \int_{\Gamma} t_{\alpha\beta}^* u_{\alpha} d\Gamma + \int_{\Gamma} \tau_{\beta}^* U_n d\Gamma = \int_{\Gamma} u_{\alpha\beta}^* t_{\alpha} d\Gamma + \int_{\Gamma} \tau U_{n\beta}^* d\Gamma \quad (8)$$

$$\int_{\Gamma} t_{\alpha 3}^* u_{\alpha} d\Gamma + \int_{\Gamma} \tau_3^* U_n d\Gamma = \int_{\Gamma} u_{\alpha 3}^* t_{\alpha} d\Gamma + \int_{\Gamma} \tau (U_{n3}^* - J X_{\alpha}^{*\prime} n_{\alpha}) d\Gamma + J c_{33} \tau \quad (9)$$

$$J = \frac{1}{i\omega b - \omega^2 \rho_{12}} \quad (10)$$

The fundamental solutions for the solid and for the fluid are introduced by Eq. (11) and Eq. (12), respectively.

$$t_{\alpha j}^* = \left(\lambda e_j^* + \frac{\alpha}{R} \psi_{3j} \right) n_{\alpha} + 2\mu e_{\alpha j}^* \quad (11)$$

$$U_{nj}^* = J \left(\psi_{3j,\alpha} + \frac{1}{2\pi} \frac{r_{\alpha}}{r} \delta_{3j} \right) n_{\alpha} + Z \psi_{\alpha j} n_{\alpha} \quad (12)$$

Where $Z = J(i\omega b + \omega^2 \rho_{12})$. The integrals are written as,

$$c^i u^i + \int_{\Gamma} p^* u d\Gamma = \int_{\Gamma} u^* p d\Gamma \quad (13)$$

Where u and p are vector fields from variables in Eq. (14) for solid displacement and fluid stress, respectively. The variables p^* and u^* are the fundamental solutions, as presented in Eq. (15).

$$u = \begin{bmatrix} u_1 \\ u_2 \\ \tau \end{bmatrix} \text{ and } p = \begin{bmatrix} t_1 \\ t_2 \\ U_n \end{bmatrix} \quad (14)$$

$$p^* = \begin{bmatrix} t_{11}^* & t_{21}^* & -U_{n1}^* \\ t_{12}^* & t_{22}^* & -U_{n2}^* \\ t_{13}^* & t_{23}^* & -U_{n3}^* \end{bmatrix} \text{ and } u^* = \begin{bmatrix} u_{11}^* & u_{21}^* & -\tau_1^* \\ u_{12}^* & u_{22}^* & -\tau_2^* \\ u_{13}^* & u_{23}^* & -\tau_3^* \end{bmatrix} \quad (15)$$

Where $\hat{U}^* n3 = U^* n3 - J X^*_{\alpha} n_{\alpha} = (J \tau^*_{3,\alpha} + Z u^*_{\alpha 3}) n_{\alpha}$ and c^i is introduced by Eq. (16).

$$c^i = \frac{1}{2} \begin{bmatrix} 1 & 0 & 0 \\ 0 & 1 & 0 \\ 0 & 0 & -J \end{bmatrix} \quad (16)$$

Considering the domain discretized in constant boundary elements Eq. (13) can be rewritten as,

$$c^i u^i + \sum_{j=1}^N \left\{ \int_{\Gamma_j} p^* d\Gamma \right\} u^j = \sum_{j=1}^N \left\{ \int_{\Gamma_j} u^* d\Gamma \right\} p^j \quad (17)$$

Eq. (17) can be also replaced according to Eq. (18) or Eq. (19).

$$c^i u^i + \sum_{j=1}^N \hat{H}^{ij} u^j = \sum_{j=1}^N G^{ij} p^j \quad (18)$$

$$\sum_{j=1}^N H^{ij} u^j = \sum_{j=1}^N G^{ij} p^j \quad (19)$$

One can also introduce Eq. (20) in order to take into account the coincidence between the source point and field point.

$$\begin{aligned} H^{ij} &= \hat{H}^{ij} && \text{when } i \neq i \\ H^{ii} &= \hat{H}^{ii} + c^i && \text{when } i = i \end{aligned} \quad (20)$$

Equation (19) can be written as matrix,

$$H u = G p \quad (21)$$

where H and G are the influence coefficients matrices. For each node u_1 or t_1, u_2 or t_2 and τ or U_n are known variables and consequently $3N$ variables are unknown. Thus, the linear system as introduced in Eq. (20) can be rearranged, passing all unknown variables to the left side. This system can now be written as,

$$A X = F \quad (22)$$

where X is the unknown vector of displacement, traction, pore pressure and flux. F is a known vector and A is the coefficient matrix.

3. Genetic Algorithm

The genetic algorithm (GA) was originally proposed by John Holland [16] and it is based on the Darwinian principle of natural selection. The simplest genetic algorithm that still leads to good results in many practical problems is composed of four operators: selection, crossover, mutation and replacement. The selection operator is an artificial version of natural selection based on Darwinian survival of the fittest among string creatures. The crossover operator is performed after reproduction, creating two new populations from two existing ones by genetically recombining randomly chosen parts formed by a randomly chosen crossover point. The mutation is the operator that increases the possibility of finding the global optimum. This operator changes a percentage of individuals by altering the value of the existing string. The last operator is the replacement that is used to decide which individuals remain or are replaced in a population. There are many improvements on GA theory in order to make the optimization process more efficient and powerful. In this sense, many methodologies based on GA architecture have been developed. Based on some successful applications of optimization problems found in the literature, the NSGA-II was chosen as the GA algorithm. It is important to highlight that this algorithm uses a methodology where the concepts of dominance and diversity are applied simultaneously, which makes the NSGA-II an efficient tool in the search process and optimization of an objective function [15]. (Fig. 1) depicts a scheme of the NSGA-II structure used in this work.

The RMSE (root mean square error) was chosen as the objective function as introduced by Eq. (23). Minimizing the objective function, an approximation of the design variables results.

$$RMSE = \sqrt{\frac{(YY - Y)^2}{YY}} \quad (23)$$

where YY stands for the displacement obtained by numerical solution [12] and Y for the displacements obtained through an analytical solution.

The design variables that represent the poroelastic medium are stored in a vector $\{E, G, \nu, \nu_u, B, \alpha, R, k, \phi\} = \{\text{Young's modulus, shear modulus, Poisson's coefficient, undrained Poisson's ratio, Skempton's pore pressure, Biot's coefficient, poroelastic constitutive coefficient, intrinsic permeability, porosity}\}$, which will be maximized or minimized during the optimization process. Based on the specific sample of soils, the search space was defined according to Table 1.

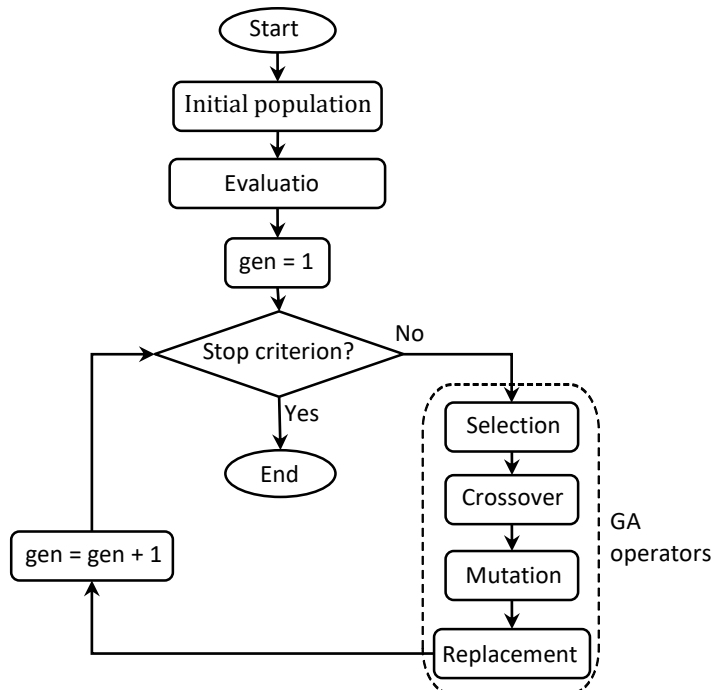


Fig. 1 GA scheme

Table 1 Search space

	Minimum	Maximum
G	1.5 x 1010	6 x 109
N	0.15	0.25
vu	0.31	0.34
B	0.50	0.85
K	4 x 10-4	8 x 102
Φ	0.01	0.26

4. The Revisited Problem: Stress Excitation on Top of Column

A problem investigated by Cheng [14] is revisited in order to test the proposed methodology in this work. (Fig. 2) introduces a one-dimensional saturated soil or rock column with three possible excitation modes: a stress and pressure excitation at the top, and a displacement excitation at the bottom. Cheng [14] separately examined these excitations. Despite its importance, only the displacement excitation will be taken into account.

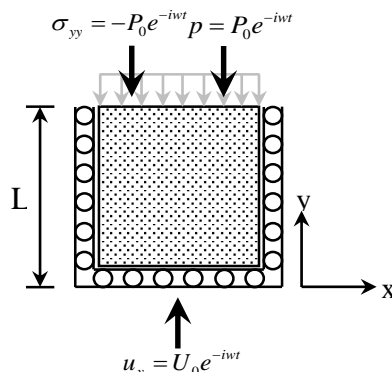


Fig. 2 One-Dimensional Saturated Soil Column under Dynamic Loading

It was considered that the top of the column was subject to a harmonic normal stress of $-P_0 e^{-iwt}$ with the surface drained. The bottom and sides are confined by rigid, frictionless and impermeable walls. The imposed boundary conditions for this problem are introduced as,

$$\begin{aligned}\tilde{u}_y &= 0 ; \quad \tilde{q}_y = 0 \quad \text{to} \quad y = 0 \\ \tilde{\sigma}_{yy} &= -P_0 ; \quad \tilde{p} = 0 \quad \text{to} \quad y = L\end{aligned}\tag{24}$$

Cheng [14] and Dominguez [19] present the exact solution for the unidimensional poroelastic in terms of displacement, which can be obtained by using a mathematical symbolic computation program. They are presented as,

$$\frac{E_s \tilde{u}_y}{P_0 L} = \frac{d_3 \left[e^{-\lambda_1(L-y)} - e^{-\lambda_1(L+y)} \right]}{L(\lambda_3 d_1 - \lambda_1 d_3)(1 + e^{-2\lambda_1 L})} - \frac{d_1 \left[e^{-\lambda_3(L-y)} - e^{-\lambda_3(L+y)} \right]}{L(\lambda_3 d_1 - \lambda_1 d_3)(1 + e^{-2\lambda_3 L})}\tag{25}$$

$$E_s = \frac{2G(1-\nu)}{(1-2\nu)} \quad (26)$$

$$d_i = \frac{E_s \lambda_i^2 + \omega^2 (\rho - \beta \rho_f)}{\lambda_i (\alpha - \beta)} \quad (27)$$

$$\lambda_1 = \sqrt{\frac{-B_0 + \sqrt{B_0^2 - 4A_0C_0}}{2A_0}} ; \lambda_1 = \sqrt{\frac{-B_0 - \sqrt{B_0^2 - 4A_0C_0}}{2A_0}} \quad (28)$$

$$A_0 = \frac{E_s \beta}{\omega \rho_f} ; B_0 = \frac{\omega \beta (\rho - \beta \rho_f)}{\rho_f} + \frac{E_s \omega \phi^2}{R} + \omega (\alpha - \beta)^2 \text{ and} \\ C_0 = \frac{\omega^3 \phi^2 (\rho - \beta \rho_f)}{R} \quad (29)$$

Where E_s is the drained elastic property, ω is the frequency of excitation, ρ is the density of the soil (ρ_s stands for the solid density, ρ_f for the fluid density and ρ_a is the additional density) and λ_1 is the wave number and characterizes a high-velocity dilatational wave and λ_3 a low-velocity dilatational and dissipative wave [6]. For the routine calculations A_0 , B_0 and C_0 , it is necessary to calculate Biot's effective coefficient α , the constitutive coefficient poroelastic R and the force field β obtained through frequency depending on whether or not the material exhibits viscoelastic behavior [5]. The equation of the force field can be seen in Eq. (30).

$$\beta = \frac{\omega \phi^2 \rho_f k}{i\phi^2 + \omega k (\rho_a + \phi \rho_f)} \quad (30)$$

For this analysis, six material constants were used corresponding to the mechanical properties of Berea sandstone: $G = 6.0 \times 10^9 \text{ N/m}^2$; $\nu = 0.2$; $\nu_u = 0.33$; $k = 1.9 \times 10^{-10} \text{ m}^4/\text{N.s}$; $B = 0.62$; $\phi = 0.19$; $\rho_s = 2800 \text{ kg/m}^3$; $\rho_f = 1000 \text{ kg/m}^3$; $\rho_a = 150 \text{ kg/m}^3$ and a column length of $L = 1$ [16]. Dominguez [19] introduced a BEM formulation for dynamic poroelastic problems. The efforts were initially devoted to the analysis of the Biot coefficients and the development of the boundary integral equations in terms of solid displacement and fluid stress. Selvadurai [20] also introduced an analysis about waves for poroelastic media, applying the statements proposed by Cheng [14] and Dominguez [19]. In order to validate the methodology introduced by Domingues [19] and apply the proposed formulation by Biot [8], the vertical displacements obtained by the excitation at the top of a column were calculated. The numerical solutions were analyzed and compared with the analytical solution introduced by Cheng [14], using the same constant materials previously defined by Rice and Cleary [18]. This same analysis was performed using the principles of the Biot theory by Selvadurai [20] using the BEM for studying wave propagation in a saturated poroelastic media. In this study, peaks of resonance for low frequencies $\omega_n = (2n-1)\omega_1$, were found, with $n = 1, 2, 3, \dots$. (Fig. 2) depicting the numerical solution versus the analytical solution. The results were plotted in absolute values of normalized displacement at the top of the column $\tilde{u}_y(L)E_u/P_0L$ versus the dimensionless frequency $\omega^* = \omega/\omega_1$. The first frequency of resonance ω_1 can also be determined by Eq. (40) and E_u is the undrained elastic module as introduced by Eq. (41). According to Selvadurai [20], for frequencies below the first natural frequency, the dimensionless displacement approximates the values of the poroelastic displacements for the elastic behavior.

$$\omega_1 = \frac{\pi}{2L} \sqrt{\frac{E_u}{\rho}} \quad (40)$$

$$E_u = \frac{2G(1-\nu_u)}{(1-2\nu_u)} \quad (41)$$

The problem initially introduced by Selvadurai [20] followed by Dominguez [19] was discretized into 24 constant elements, numerically integrated with four Gauss points and considers a discrete set of 44 frequencies. (Fig. 3) depicts the perfect overlapping until $\omega = 2.5 \omega_1$ where after this point, it is possible to see a small offset between both curves.

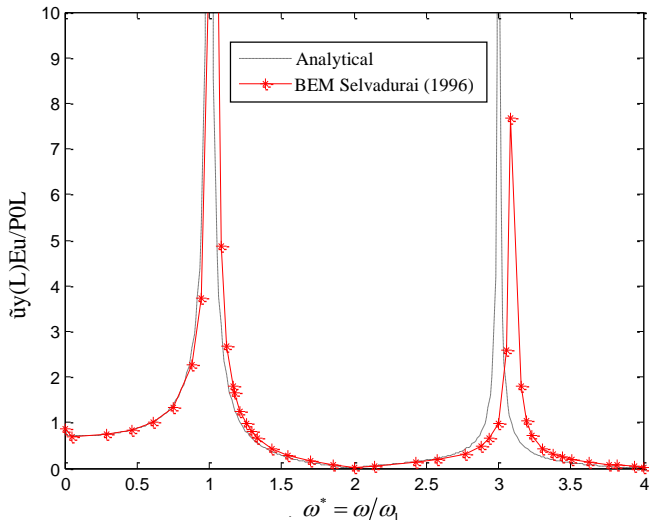


Fig. 3 Displacement at the top of the column (stress excitation)

5. The Numerical Results Using GA And BEM

In order to define the mechanical properties of the soil, a numerical routine was written to couple both, the GA and the BEM. The domain was discretized into 32 constant boundary elements and integrated numerically with six Gauss points. A set of 327 frequencies was defined in order to ensure a good definition of the curves and the resonance peaks. The objective function as aforementioned, was the RMSE and the design variables to be optimized were: G , v , ν_u , B , k , and ϕ . Table 2 summarizes the maximum and minimum values for the search space, the values of the material constant imposed for the analytical solution and those obtained after the optimization process. According to the resulting mechanical properties after the optimization process, it is suggested that the soil is Berea sandstone.

The numerical results are related to the permeability of the soil in consequence of the fluid trapped in the pores and the volumetric reaction of the process with fluid and solid. The deformations present elastic behavior and are linked as variables of the optimization process. The numerical results are related to the frequencies (ω) of the loads.

After searching fields in approximately 10 thousand iterations in the GA, the three variables that most influenced the process were: permeability (k) because it is related to a

quantity of pores (ϕ) and the interconnection between them affecting soil poropressure behavior; the shear coefficient (G) that can approach a maximum stress, allowing a quantity of material (ideal); and the Poisson coefficient drained (v_u) being the most differentiated coefficient. Since there is load dynamics in the structure, it was made with this parameter to undergo great influence without calculation.

Table 2 Design variables, search range, analytical and optimized variables.

Design variables	Search space max	Search space min	Analytical	Optimized
G	6 x 109	6 x 1019	6 x 109	5.95 x 109
N	0.20	0.18	0.20	0.20
v_u	0.33	0.28	0.33	0.31
B	0.62	0.50	0.62	0.61428
K	1.9 x 102	5.6 x 100	1.9 x 102	9.54 x 10-1
ϕ	0.19	0.19	0.19	0.195

The stop criterion was set to approximate the values of the variables through the optimization process with a minimum possible value; therefore, it was used as the reference in Eq. (23) in $RMSE \leq 0.025$ and was achieved for a value of 0.02509069.

A comparison between the analytical curve and the optimized one, can be seen as (Fig. 3) (load transmitted by dynamic pressure) with the effects of the distribution of the AG coupled to the BEM overlapping the analytic curve adopted by Cheng [14].

It is possible to observe a proximity between the solutions, and as in Selvadurai [20] there was no total overlap of the curves. Full overlap requires a thorough investigation of the problem.

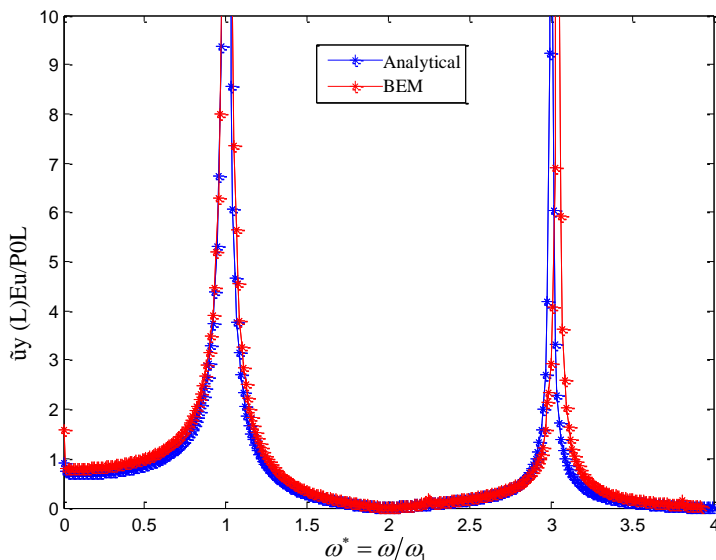


Fig. 3 Displacement at the top of the column (stress excitation)

5. Conclusion

The main goal of this work was to develop a numerical procedure using BEM and GA-NSGA-II in order to determine the design variables G , B , k , v , v_u , and ϕ as mechanical properties of soil. The presented methodology was shown to be efficient for predicting the kind of underground soil if a displacement x frequency curve is previously known. Despite using an analytical curve for the displacement x frequency behavior, the present methodology can also be used with a curve obtained experimentally. Regarding the design variables, it is important to highlight that the permeability (k) was the variable that was most influenced during the optimization process. The main reason is due to the fact that this variable takes into account the amount of pores, the connection between them and finally the strong influence in the fluid percolation. All advantages from the BEM features provided a low computational cost and resulted in a good prediction for the characterization of the soil.

References

- [1] Terzaghi, K. (1925). "Principles of soil mechanics, IV—Settlement and consolidation of clay". *Engineering News-Record*, 95(3), 874-878.
- [2] Biot, M. A. and Willis, D. G. (1956). "The elastic coefficients of the theory of consolidation". *J. Appl. Mech.*, 24, 594-601.
- [3] Terzaghi, K. (1936). "The shearing resistance of saturated soils and the angle between the planes of shear". *Proceedings of the International Conference on Soil Mechanics and Foundation Engineering*, pp. 54-56.
- [4] Gassmann, F. (1951). "Elasticity of porous media". *Vierteljahrsschrder Naturforschenden Gessellschaft*, 96, 1-23.
- [5] Biot, M. A. (1956a). "Theory of propagation of elastic waves in a fluid-saturated porous solid. I. Low- frequency range". *Journal of Applied Physics*. Nr 28. pp. 168-178. <https://doi.org/10.1121/1.1908239>
- [6] Biot, M. A. (1956b). "Theory of propagation of elastic waves in a fluid-saturated porous solid. I. High- frequency range". *Journal of Applied Physics*. Nr 28. pp. 179-191.
- [7] Plona, T. J. (1980). "Observation of a second bulk compressional wave in a porous medium at ultrasonic frequencies". *Appl. Phys. Lett.*, 36:259-261. <https://doi.org/10.1063/1.91445>
- [8] Biot, M. A. (1956). "Theory of Deformation of a Porous Viscoelastic Anisotropic Solid", *Journal of Applied Physics*, vol. 27, pp 459 - 467. <https://doi.org/10.1063/1.1722402>
- [9] Schanz, M., Pryl, D. (2004). "Dynamic fundamental solutions for compressible and incompressible modeled poroelastic continua". *International Journal of Solids and Structures*, 41(15), 4047-4073. <https://doi.org/10.1016/j.ijsolstr.2004.02.059>
- [10] Millán, M. A., & Domínguez, J. (2009). "Simplified BEM/FEM model for dynamic analysis of structures on piles and pile groups in viscoelastic and poroelastic soils". *Engineering Analysis with Boundary Elements*, 33(1), 25-34. <https://doi.org/10.1016/j.enganabound.2008.04.003>
- [11] Gensterblum, Y., Ghazizadeh, A., and Krooss, B. M. (2014). "Gas permeability measurements on Australian subbituminous coals: fluid dynamic and poroelastic aspects". *Journal of Natural Gas Science and Engineering*, 19, 202-214. <https://doi.org/10.1016/j.jngse.2014.04.016>
- [12] Berg, S. J., Hsieh, P. A., and Illman, W. A. (2011). "Estimating hydraulic parameters when poroelastic effects are significant". *Groundwater*, 49(6), 815-829. <https://doi.org/10.1111/j.1745-6584.2010.00781.x>
- [13] Apostolakis, G., & Dargush, G. F. (2013). "Mixed variational principles for dynamic response of thermoelastic and poroelastic continua". *International Journal of Solids and Structures*, 50(5), 642-650. <https://doi.org/10.1016/j.ijsolstr.2012.10.021>

- [14] Cheng, A. H. D., Badmus, T., Beskos, D. E. (1991). "Integral equation for dynamic poroelasticity in frequency domain with BEM solution". Journal of Engineering Mechanics, 117(5), 1136-1157. [https://doi.org/10.1061/\(ASCE\)0733-9399\(1991\)117:5\(1136\)](https://doi.org/10.1061/(ASCE)0733-9399(1991)117:5(1136))
- [15] Terzaghi, K. (1923). "Die Berechnung der Durchlässigkeitssziffer des Tones aus dem Verlauf der hydrodynamische Spannungerscheinungen". Sitzber. Akad. Wiss. Wien, Abt. IIa, 132, 125-138.
- [16] Holland, J. H. (1975). "Adaptation in Natural and Artificial Systems. University of Michigan Press". Ann Arbor.
- [17] Deb, K.; Agrawal, S.; Pratab, A.; Meyarivan, T. (2000). "A fast elitist non-dominated sorting genetic algorithm for multi-objective optimization: NSGA-II". Kangal Report 200001, Indian Institute of Technology, Kanpur, India. https://doi.org/10.1007/3-540-45356-3_83
- [18] Rice, J. R., Cleary, M. P. (1976). "Some basic stress diffusion solutions for fluid-saturated elastic porous media with compressible constituents." Reviews of Geophysics and Space Physics, V.14, N.2, P.227-41. <https://doi.org/10.1029/RG014i002p00227>
- [19] Dominguez, J. (1993). "Boundary elements in dynamics". Wit Press.
- [20] Selvadurai, A. P. S. (1996). Mechanics of poroelastic media. In Antes, H., & Wiebe, T. "Analyses of waves in 3-d poroelastic media". (Pp. 371-387). Springer Netherlands. <https://doi.org/10.1007/978-94-015-8698-6>

CONTENT

Editorial Note

- 137 **Andreas Öchsner, Luiz A. O. Rocha, Antonio F. Miguel**
Preface

Research Article

- 139 **Marcelo Langhinrichs Cunha, Grégori da Silva Troina, Elizaldo Domingues dos Santos, Luiz Alberto Oliveira Rocha, Liércio André Isoldi**
Computational modeling and Constructal Design method applied to the geometric optimization of stiffened steel plates subjected to uniform transverse load

Research Article

- 151 **Liang Ji, Xinzhi Liu, Houlei Zhang**
Properties of furfural residue and its drying characteristics in single-shaft paddle heat exchangers

Research Article

- 161 **Onur Yenigün, Turgay Coşkun, Erdal Çetkin**
The effect of time delay of fluid flow in a vascularized plate

Research Article

- 169 **Daniel Helbig, Marcelo Langhinrichs Cunha, Caio Cesar Cardoso da Silva, Elizaldo Domingues dos Santos, Ignácio Iturrio, Mauro de Vasconcellos Real, Liércio André Isoldi, Luiz Alberto Oliveira Rocha**
Numerical study of the elasto-plastic buckling in perforated thin steel plates using the constructal design method

Research Article

- 189 **Nelson C. Batista, Rui Melicio, Victor M.F. Mendes**
Darrieus vertical axis wind turbines: methodology to study the self-start capabilities considering symmetric and asymmetric airfoils

Research Article

- 219 **Anunciação Jr.N. C, Anflor C.T.M, Goulart J.N.V**
Optimization applied to dynamic poroelasticity using boundary element method (BEM) and genetic algorithm (GA)



www.jresm.org



**Research on
Engineering
Structures & Materials**

Published by

**MIM RESEARCH
GROUP**